



Università Politecnica delle Marche
Scuola di Dottorato di Ricerca in Scienze dell'Ingegneria
Corso di Dottorato in Ingegneria Civile, Ambientale, Edile e Architettura

The application of video-monitoring data to understand coastal and estuarine processes

Ph.D. Dissertation of:
Eleonora Perugini

Advisor:

Prof. Maurizio Brocchini

Coadvisors:

Dr. Luciano Soldini

Dr. Margaret L. Palmsten

Curriculum supervisor:

Prof. Stefano Lenci

XVII edition - new series

Università Politecnica delle Marche
Dipartimento di Ingegneria Civile, Ambientale, Edile e Architettura (DICEA)
Via Brezze Bianche — 60131 - Ancona, Italy

Acknowledgements

I would like to acknowledge my advisor Prof. M. Brocchini for coordinating my PhD study and for his availability and knowledge. I am especially grateful to my coadvisors Dr. L. Soldini and Dr. M. L. Palmsten for their patience, motivation and daily helps. Without their guidance and knowledge this work would not have been achieved.

I sincerely thank also A. Coluccelli for sharing the data of the COAWST Model, A. Sheremet for sharing measured spectra, P. Penna for sharing wave data of the Meda Station, C. Chickadel for sharing Matlab© codes, Carlo Lorenzoni for helping with the wave spectra analyses, B.G. Ruessink and T.D. Price for the information on the BLIM toolbox and R. Holman for his valuable suggestions on the cBathy. Special thanks go to J. Calantoni of the Naval Research Laboratory for his work of supervision of the EsCoSed project. The EsCoSed project was supported under base funding to the Naval Research Laboratory from the Office of Naval Research. Financial support from the ONR Global (UK), through the NICOP EsCoSed Research Grant (N62909-13-1-N020) is gratefully acknowledged.

Finally, I would like to thank my family: my grandparents, my parents, my brothers and all my dear relatives for believing in me and for supporting me in this important experience

Abstract

The present thesis details the first applications of a new video monitoring station, called SGS station, installed along the Adriatic coast, at the Senigallia harbour, Italy. SGS is not part of the Argus network but it was designed on the basis of typical Argus system. SGS is equipped with four cameras located on the top of a 25m high tower. Unlike Argus stations, which store only elaborated images, ten minutes of full-frame video data are collected at 2Hz every hour, during daylight hours. The observed area is the norther part of a 12 km long stretch of natural coast along the Adriatic Sea. It is a mildly sloping sandy beach, representative of those Adriatic beaches placed near river mouths. This area has already been studied in the past by means of traditional in-situ survey. The goal of this work is to better understand coastal and estuarine processes of the analysed area, and thus on the Adriatic Coast, using the data collected by the SGS station.

First, the video data recorded from the four cameras of the station (from 2015 to 2017) was post-processed by using Matlab© routines coded with the same approach used for the Argus Database and the CIL toolbox. From the data elaboration several products are obtained: time-exposure images, darkest images, brightest images and time series for a selected grid of pixels. Then the first three types of images are ortho rectified to obtain plane view images. The time series and the ortho-rectified time exposure images have been used for the follow applications.

The first application regards the indirect estimation of the bathymetry. To this scope a well-known algorithm for depth inversion in coastal region (cBathy) was applied to the SGS data. The results varied in quality as a function of the location and wave conditions, the bathymetry reconstruction being of insufficient quality for the area farthest from the videocameras. A detailed debugging analysis was performed to understand the causes of the problem. It was found that the code well estimates the wave period, while it underestimates the wavelength and, as a consequence, the water depth. Another crucial problem highlighted during the debugging analysis is related with the wave direction. Different from typical cBathy applications that use data from shore-based stations, the SGS station persistently looks the waves quite along the crests. Since in this condition the waves cannot be correctly

seen in the optical images, this affects the cBathy results. Synthetic tests have been performed to investigate this aspect and clarify what are the worst working conditions.

The second application regards the analysis of a multiple sandbar system present in the SGS observed area. The submerged sandbars have been identified using averaged ortho-rectified images and the BLIM toolbox. Three orders of alongshore uniform bars have been recognized from the images, in agreement with previous studies based on data collected by in-situ surveys. An on-offshore bar motion was observed on seasonal scale and bar switching and bifurcation has been also identified. The SGS station is able to monitor these seabed features and the results can be used to study the physical behaviour of the bar system. A preliminary analysis of the evolution of such bar system was performed by trying to correlate the movement of the bars with the local wave climate. The results showed different bar behaviours in response to waves of similar intensity but coming from different directions (NNE and ESE) and, therefore, with different incident wave angles (shore-normal waves and oblique waves, respectively). The different behaviour has been related to the reflection of the ESE waves off the wall of the nearby river pier.

Contents

| | |
|---|-------------|
| Contents | xi |
| List of Figures | xiii |
| List of Tables | xvii |
| List of Symbols | xix |
| Chapter 1 Introduction | 1 |
| 1.1 Objectives and thesis outline | 1 |
| 1.2 Remote Sensing to study the nearshore zone | 2 |
| 1.2.1 Remote sensing for bathymetry reconstruction | 5 |
| 1.2.2 Remote sensing for bar evolution | 7 |
| Chapter 2 The Study Area | 11 |
| 2.1 The Senigallia Beach | 11 |
| 2.1.1 Wave climate | 12 |
| 2.1.2 Bathymetric features | 16 |
| Chapter 3 The SGS Station | 21 |
| 3.1 Features and installation | 21 |
| 3.2 Data post processing | 24 |
| Chapter 4 Bathymetric Analysis | 31 |
| 4.1 cBathy Algorithm | 31 |
| 4.2 Application of cBathy to the SGS Data | 36 |
| 4.3 Debugging analysis | 40 |
| 4.3.1 cBathy debug mode | 40 |
| 4.3.2 Further Analyses | 52 |
| 4.4 Synthetic Tests | 56 |
| 4.4.1 Method | 57 |
| 4.4.1.1 Input spectra | 58 |
| 4.4.1.2 Sea surface simulation | 60 |
| 4.4.1.3 Optical model | 61 |
| 4.4.1.4 cBathy | 62 |
| 4.4.2 Effects of wave direction on water depth estimation | 64 |

| | | |
|-------------------|-------------------------------------|------------|
| 4.4.2.1 | Seed sensitivity | 68 |
| 4.4.2.2 | Frequency and wavenumber estimation | 69 |
| Chapter 5 | Sandbar analysis | 73 |
| 5.1 | Sandbar identification | 73 |
| 5.2 | Morphological features | 76 |
| 5.3 | Morphodynamic evolution | 80 |
| Chapter 6 | Conclusions | 97 |
| References | | 101 |

List of Figures

- Figure 2-1. Satellite view of the unprotected coast near Senigallia. The up-right box shows the location of Senigallia Beach. The black box highlights the study area. 11
- Figure 2-2. Location of the Senigallia beach (yellow circle), location of the Ancona RON buoy (red circles) and location of the points of the COAWST model (green circles). 14
- Figure 2-3. Frequency distribution of significant wave height (red line) and wave energy flux (blue line): (a) RON buoy 1999-2006 & 2009-2013. (b) COAWST model 2015-2017, P3. 15
- Figure 2-4. Time series of wave characteristics collected by the Meda Station from June 2018 to October 2018. The upper panel shows the significant wave height, the middle panel shows the wave peak period and the lower panel shows the wave peak direction. 16
- Figure 2-5 - (a) Bathymetric survey of the study area, May 2013. (b) Changes of the cross-shore profile highlighted from the available surveys. 19
- Figure 3-1 - a) General view of the Senigallia harbour showing the SGS Station position and the cameras field of view. b) The four cameras installed on the top of the tower. 22
- Figure 3-2 – Particulars of the camera installation. 23
- Figure 3-3 – a) Communication box. b) Camera trigger. c) Computer station. 23
- Figure 3-4. Plan view location of the GCPs surveyed by means of the GPS technology. 26
- Figure 3-5 – Merged and orthorectified images: a) Timex, b) Bright, c) Dark. 28
- Figure 3-6 Example of stabilization effects. a) Target image (red) superposed to moving image (cyan). b) Target image (red) superposed to stabilized moving image (cyan). 29
- Figure 3-7 – Example of a Timestack where the wave propagation and the swash motion ($50\text{m} < x < 100\text{m}$) are well visible. 30
- Figure 4-1 The left panel shows an example pixel array used for cBathy analyses: sampling pixels (blue dots, half shown), an example of analysis point (red asterisk) and pixels in the nearby region (green dots). The right panels show an example of offshore wave height (top) and of Process error, Q (bottom), found from bathymetric variability during the Sandy Duck field experiment, 1997. Adapted from Holman et al. (2013). 35
- Figure 4-2 Measure of the tide elevation from the SGS Timex images. 37
- Figure 4-3 – a) cBathy Phase II estimated bathymetry. The blue lines are the sections of survey profiles (2013), the red lines are the sections of the cBathy grid, and the black lines are the camera boundaries. b) Error Map (95% confidence intervals) from cBathy Phase II. Depth colormaps have blue for shallow and red for deep. The harbour is located in the

| | |
|--|----|
| upper part of the domain ($y \sim -700\text{m}$), while the Rotonda is located in the lower part ($y=0\text{m}$). | 39 |
| Figure 4-4 – Comparison of estimated and measured bathymetry. The blue lines are the survey bed (2013) and the red lines are the cBathy estimated bed. The profiles are related to the transects shown in Figure 4-3. | 40 |
| Figure 4-5 - Time series and profile at $y=316\text{m}$. The upper panel gives the Timestack, where the red dotted lines are the x -positions of the debug points. In the lower panel the blue line is the survey seabed (2013), the red line is the cBathy estimated bed and the grey lines are the x -positions of the debug points. | 41 |
| Figure 4-6 - Phase maps for the range of frequencies selected in the setting file. | 43 |
| Figure 4-7 - a) Zoom of the ortho-rectified snapshot. The red dots are the points of the sampling grid (spaced 3m), the blue dots are the points of the sections, the green dots are the debug points and the black circles identify the wave crests. b) Zoom of the phase map for the frequency 0.18Hz. | 44 |
| Figure 4-8 Comparison between observed and predicted phase and magnitude maps for the tile relative to the analysis point D ($x=275\text{m}$, $y=-316\text{m}$). The maps are ordered from the most coherent frequency (fB1) to the less coherent frequency (fB4). maxNpix=80 points. | 47 |
| Figure 4-9 Comparison between observed and predicted phase and magnitude maps for the tile related to the analysis point ($x=275\text{m}$, $y=-316\text{m}$). The maps are ordered from the most coherent frequency (fB1) to the less coherent frequency (fB4). maxNpix=500 points. | 48 |
| Figure 4-10 Profile at $y=316\text{m}$. The blue line is the survey bed (2013), the red line is the cBathy estimated bed with maxNpix=80, the green line is the cBathy estimated bed with maxNpix=500, the cyan line is the estimated bed using cBathy v1.2 and the grey lines are the x -positions of the points used for the debugging. | 49 |
| Figure 4-11 Plots of: first dominant frequency of each point (top left panel), relative wavenumber (top right panel) and gamma (bottom panel). | 51 |
| Figure 4-12 - In red the calculated values of wavelength for a period of 5.5s and the corresponding depth. The dotted black lines show the approximated position of these depths along the survey profile. The blue letters show the approximated position of some points of the debug analysis. The blue line is the survey profile (2013) while the brown line is the cBathy estimated profile. The green lines are the contours of the camera resolution. | 52 |
| Figure 4-13 Resolution along the cross-axis of the cameras (normal to main axis of the camera). The black asterisk is the camera location. The black line is the 3 m contour. The y -axis is inverted. | 53 |
| Figure 4-14 Resolution along the main axis of the cameras. The black asterisk is the camera location. The black line is the 3 m contour. The y -axis is inverted. | 53 |
| Figure 4-15 Resolution in cross-shore direction. The black asterisk is the camera location. The black line is the 3 m contour. The y -axis is inverted. | 54 |
| Figure 4-16 Resolution in alongshore direction. The black asterisk is the camera location. The black line is the 3 m contour. The y -axis is inverted. | 54 |

| | |
|--|----|
| Figure 4-17 - Scheme of the way of the cameras look at the waves in relation to their location. | 57 |
| Figure 4-18 – a) Example of peak shifting for case E01 with peak directions of 0° (red), 45° (blue), and 90° (green). b) Example of frequency directional spectrum (A20) designed using equations (4.11) to (4.15). | 60 |
| Figure 4-19 - Optical images (upper panels) and estimated bathymetry (lower panels), for case E01, for wave angles equal to 0° (a,d), 45° (b,e), and 90° (c,f). The angles are positive in the counter-clockwise direction from the x-axis. The red arrows indicate the wave direction. The seed angle has been set coherent to wave propagation. | 65 |
| Figure 4-20 – Results of bathymetric error as function of difference between wave angle and camera viewing direction. a) analytical spectra A10, A20,A21, A22; b) analytical cases A10, A11, A12 and A13 with different directional spreading; c) observed spectra E01, E02, E03, E07 and E08; d) same as c) but includes case E05. | 67 |
| Figure 4-21 – Seed angle sensitivity for analytical (a-c) and experimental (d-f) cases with wave angles of 0° (a,c), 45° (b,e), and 90° (c,f). | 69 |
| Figure 4-22 – For case E01, the residual calculated using (4.29) for wavenumbers (a,d), frequencies (b,e) and depths (c,f) are plotted. Only the first coherent frequency and one realization for waves coming from 0° (a-c) and 92° (d-f) is illustrated. Mean (*) and standard deviation (bars) of relative error (4.30) are shown for wavenumber (g) and frequency (h) as a function of wave viewing direction. | 71 |
| Figure 4-23 – For case E01, the residual calculated using (4.29) for the seed analysis of wavenumbers (a,d), frequencies (b,e) and depths (c,f) are plotted. Only the first coherent frequency for seed equal to 0° (a-c) and 90° (d-f) is illustrated. Relative wavenumber (g) error is affected by seed angle, while frequency (h) is determined before the non-linear fit in step 1 of the cBathy algorithm and is therefore not sensitive to seed angle | 72 |
| Figure 5-1 – Extrapolation of intensity from imagery. Three Blimelines are identified in the images (green, violet and orange lines). The vertical continuous black lines indicate the location of three cross-shore sections (-500m, -400m, -300m) for which the sampling intensity profile is shown (blue lines). | 74 |
| Figure 5-2. Example of bar crest identification from stabilized ortho-rectified Timex images and comparison with the bathymetric survey of 2013. Blue lines give the breaking lines from BLIM; red, yellow and green dots are, respectively, the location of the outer, intermediate and inner bar crests from the bathymetric survey. | 76 |
| Figure 5-3 Sandbars configurations occurring during the SGS station functioning. | 79 |
| Figure 5-4 Wave climate from the COAWST model. The three upper panels show the frequency distribution of significant wave height (red line) and wave energy flux (blue line), in the years 2015, 2016 and 2017 (respectively from left to right). The lower panel shows the time series of the significant wave height for the first six months of 2016. The variation of the colour indicates the wave direction. The numbers indicate the progressive storms | 81 |
| Figure 5-5 - Sandbar position in relation to the wave climate. (a) Significant wave height from the COAWST model. The variation of the colour indicates the wave periods (light blue <5s, blue=5s, green=6, magenta=7s, red>7s). The numbers indicate the progressive storms. The vertical black lines indicate the days shown in the bottom panels. (b)-(f) | |

| | |
|---|----|
| breaker lines extracted from Timex images: blue, green and red lines are for inner, intermediate and outer bars respectively. | 82 |
| Figure 5-6 Correlation between the mean sand bar location (upper panel) and the wave climate (lower panel), for the full analysed period. The numbers indicate the progressive storms. The yellow bands indicate the period in which the station did not work. | 83 |
| Figure 5-7 – Correlation of the cross-shore mean intermediate bar position (central panel), the alongshore variability (right panel) and the wave climate for year 2016 (left panel). The numbers indicate the progressive storms. | 84 |
| Figure 5-8 From the upper to the lower panel: significant wave height time series from P3 of the COAWST model, the numbers indicate the progressive storms; total energy flux for each storm; cross-shore component of the energy flux; alongshore component of the energy flux; duration of the storms in hours. | 87 |
| Figure 5-9 – Test1 (ESE) – Upper panel: seabed profile. Middle panel: wave height. Lower panel: mean undertow current. The vertical solid line is the breaking point, the vertical dash-dot line is the end of the transition zone. | 91 |
| Figure 5-10 – Test2 (NNE) – Upper panel: seabed profile. Middle panel: wave height. Lower panel: mean undertow current. The vertical solid line is the breaking point, the vertical dash-dot line is the end of the transition zone. | 92 |
| Figure 5-11 –Bathymetry and geometry used in the Boussinesq simulation. Points G1 and G2 are two probes. | 93 |
| Figure 5-12 – Acceleration skewness recorded from gauge 1 (upper panel) and from gauge 2 (lower panel). The red lines represent the ESE storm while the blue lines represent the NNE storm. | 94 |

List of Tables

| | |
|---|----|
| Table 3-1 Examples of post-processed images (13 March 2017 h 13.00) | 24 |
| Table 4-1 – Example of setting parameters used to apply the cBathy algorithm to the Senigallia site. | 38 |
| Table 4-2. Numerical results for the debug point D ($x=275\text{m}$, $y=-316\text{m}$). The depths are not tide corrected yet. $\text{maxNpix}=80$ points. | 47 |
| Table 4-3 Numerical results for the debug point D ($x=275\text{m}$, $y=-316\text{m}$). The depths are not tide corrected. $\text{maxNpix}=500$ points. | 48 |
| Table 4-4 - Celerity analysis, point D. | 50 |
| Table 4-5 - Summary of analysed sea states and parameters, from analytical source. For each case the table displays the index, the peak period, the significant wave height, the spreading parameter, the camera height, the camera tilt angle (fixed in the patches) and the water depth. | 58 |
| Table 4-6 - Summary of analysed sea states and parameters, from EsCoSed experiment source. For each case the table displays the index, the peak period, the significant wave height, the wave energy, the camera height, the camera tilt angle (fixed in the patches), the water depth, and the time of measurement. | 58 |
| Table 4-7 - Summary of cBathy parameters. The x-axis is the cross-shore direction, and the y-axis is the alongshore direction. | 63 |
| Table 5-1 Wave characteristics of two representative storms from the COAWST model. H_s is the significant wave height, T_p is the peak wave period, θ is the wave direction with respect to the cross-shore direction, positive clockwise, looking towards offshore. Test 1 is the ESE storm n.6 of Figure 5-8, while Test 2 is the NNE storm n. 8 of Figure 5-8 | 88 |
| Table 5-2 Results of the first net offshore transport analysis. Analytical model of equations (5.9)-(5.18). | 92 |
| Table 5-3 Results of the net offshore transport analysis. Analytical model of equations (5.9)-(5.18) with increased longshore velocities by reflection off the river pier (equation 5.19). | 95 |

List of Symbols

| | |
|--------------|---|
| (Fx, Fy) | cross-shore and the alongshore component of the energy flux |
| (U, V) | 2D image coordinates |
| (X, Y, Z) | 3D world coordinates |
| (x, y) | cross-shore and alongshore coordinate |
| (U_0, V_0) | image centre coordinates |
| (f_U, f_V) | focal lengths |
| (x_0, y_0) | global coordinates of the origin of the local coordinate system |
| $[x_p, y_p]$ | pixel sampling array (cBathy) |
| $[x_m, y_m]$ | user-defined analysis point (cBathy) |
| D_{50} | median-diameter of sediment |
| h_{hour} | current hourly estimates (Kalman filter) |
| h_b | water depth at the breaking point |
| h_{prior} | previous running averaged bathymetry (Kalman filter) |
| h_{update} | updated average depth (Kalman filter) |
| U_b | depth-averaged time-mean undertow velocity |
| U_r | mean velocity due to the surface roller |
| U_w | mean velocity due to the Stokes drift |
| Ω^* | dimensionless fall velocity |
| A_n | amplitude of the noise signal in the frequency domain |
| A_w | amplitude of the wave signal in the frequency domain |

| | |
|------------|---|
| B^* | bar parameter |
| B_0 | wave shape parameter for the undertow |
| C_f | friction coefficient due to the waves and currents |
| D_0 | normalization factor |
| F_i | energy fluxes of each hour |
| H_b | breaking wave height |
| H_t | wave height at the end of the transition zone |
| K_1 | constant (Taylor approximation) |
| K_v | von Karman's constant |
| N_h | number of hours |
| N_s | elements of the transformed series |
| T_z | mean zero-upcrossing period |
| U'_b | maximum value of the undertow current |
| U_b^* | friction velocity |
| V_b | longshore velocity at the breaker line by considering the presence of horizontal mixing |
| V'_b | maximum value of the longshore current |
| V_o | maximum longshore velocity at the breaker line with no horizontal mixing |
| c_g | group speed |
| f_c | friction coefficient due to current |
| k_{deep} | deep water wavenumber |
| k_s | roughness height of the stationary bed |
| n_E | estimated value |
| n_T | true value |
| r_c | camera viewing direction |

| | |
|---------------|---|
| r_i | radiance incident ray |
| r_n | vector normal to the wave sea surface |
| s_k | image skewness |
| v_1 | dominant eigenvector of the cross-spectral matrix |
| v_1' | phase of the dominant eigenvector |
| w_s | sediment settling velocity |
| x_s | offshore distance where the beach slope becomes very small |
| α_c | camera azimuth or camera view direction |
| α_n | wave propagation direction |
| α_n | wave direction |
| γ_n | wave slope |
| θ_0 | offshore wave direction with respect to the cross-shore direction |
| θ_p | spectral peak direction |
| θ_b | wave angle at the breaking line |
| ρ_a | water density |
| ρ_s | particles density |
| τ_b | bed shear stress |
| φ_n | phases of the harmonic variability of the noise |
| ω' | angle of refraction |
| f | frequency |
| fB1 | most coherent frequency |
| h | still-water depth |
| hc | camera height |
| \mathcal{I} | identity matrix |
| \mathcal{L} | sky radiance distribution |

| | |
|------------------|--|
| lam1 | normalized eigenvalues |
| maxNpix | maximum number of points per tile |
| \mathcal{R} | Fresnel reflection coefficient |
| t | time |
| TR | tide range |
| α | wave direction |
| γ | Gamma coefficient |
| Γ | Gamma Function |
| ϕ | iphase shift |
| A | dimensional shape parameter (equilibrium profile) |
| C | vector of camera centre in world coordinates |
| $D(f, \theta)$ | directional distribution |
| E | wave energy |
| $E(f)$ | one dimensional, frequency dependent wave spectrum |
| F | energy flux |
| G | intensity signal from the frequency domain |
| $G(f)$ | coefficient (spectrum) |
| H | local wave height |
| H_s | significant wave height |
| I | intensity signal from the time domain |
| K | intrinsic matrix |
| K_r | refraction coefficient |
| K_s | shoaling coefficient |
| L | wave length |
| N | number of comparison values |
| P | projection matrix |

| | |
|----------------|--|
| Q | process error |
| R | camera rotation matrix |
| RTR | relative tide range |
| $S(f, \theta)$ | analytic frequency-directional spectra |
| S_{max} | spectrum wave energy |
| T | wave period |
| T_p | spectral peak period |
| V | longshore current |
| W | Fourier series of the surface elevation |
| c | wave celerity |
| g | gravitational acceleration |
| k | radial wavenumber |
| m | bottom slope |
| n | constant (equilibrium profile) |
| rM | roto-translation matrix |
| s | spreading parameter |
| \mathcal{C} | cross-spectral matrix () |
| \mathcal{K} | is the Kalman gain |
| Ω | radial wave frequency |
| β | Coefficient for considering the horizontal mixing |
| δ | height-to-depth ratio of breaking waves in shallow water |
| η | sea surface elevation time series |
| θ | wave direction |
| ν | kinematic viscosity of water |
| σ | coefficient (spectrum) |

| | |
|-------------|---|
| τ | camera tilt from horizontal |
| φ | phases of the harmonic variability of waves |
| ω | angle of incidence of the sky radiance with respect to the sea surface normal |
| ϑ | rotation angle between the global and local coordinates |

Chapter 1 Introduction

1.1 Objectives and thesis outline

This thesis concerns the first application of the data coming from a new video-monitoring station (SGS station) installed in July 2015 at the Senigallia Harbor, Italy. The overall goal of this work is to improve the knowledge of the hydro-morphodynamics of a micro-tidal, estuarine sandy beach environment (Senigallia beach) that is typical of the beach near an estuary along the Adriatic coast (Italy). Notwithstanding the capability of SGS station to explore the physical processes that evolve both in the beach on the south side of the Senigallia harbour and in the mouth of the Misa River, the present thesis mainly focuses on improving the knowledge of the morphological features of the sandy beach by adding to traditional survey techniques new prospective of study deriving from the video-monitoring data.

Two main aspects have been investigated:

- I) the study of the capability of the SGS data to estimate the water depth using cBathy (a widely used algorithm for depth-inversion) (see Chapter 4)
- II) the study of the dynamics of a multiple sandbars system by using the bar line information coming from post-processed images of the SGS station (see Chapter 5)

In detail the thesis is organised in six chapters.

Chapter 1 (*Introduction*) introduces the main aspects and gives an historical overview of the remote sensing techniques used to study the nearshore zone, with a focus on the use of this technology to perform bathymetry reconstruction and bar evolution analyses.

Chapter 2 (*The study area*) describes, on the basis of previous studies and traditional survey techniques, the main hydrodynamic features and the morphological characteristics of the observed area

Chapter 3 (*The SGS station*) introduces the SGS station and describes the installation, the data acquisition and the data post-processing analyses. All the post-processing products that are being elaborated are illustrated, with particular attention to those that are used in the analyses of this thesis.

Chapter 4 (*Bathymetric Analysis*) describes the first application of the SGS data to indirectly estimate the nearshore bathymetry. More in detail, Section 4.1 describes the widely used cBathy algorithm, while Section 4.2 shows the results of the application of cBathy to the SGS optical data. The implementation produced results that vary in quality as a function of the location and wave conditions and highlights an underestimation of the water depth over much of the domain. A debugging analysis performed to find the source of the underestimation is illustrated in Section 4.3. The depth underestimation has been mainly related to the difference between the wave direction and camera pointing direction. The relevance of this aspect has been analysed in depth using synthetic tests in Section 4.4.

Chapter 5 (*Sandbar analysis*) describes the application of the SGS data to analyse the submerged nearshore sandbars behaviour. The capability of the station to support analyses of the evolution of a multiple bar system is investigated. The methodology used to extract information on the bar crest positions from the images collected by the cameras is first described in Section 5.1. Then, the observed bar morphology (Section 5.2) and the cross-shore mobility of the bars (Section 5.3) are discussed.

Chapter 6 (*Conclusion*) provides some final considerations, general conclusion and suggests some possible future development.

1.2 Remote Sensing to study the nearshore zone

The nearshore zone is the area of the sea that extends from the breaking line to the shoreline. It can be further divided into two different areas: the surf zone, where the waves break and the swash zone, where the waves reach the beach and move the instantaneous shoreline back and forth.

The hydro-morphodynamics of this area, where the most dissipation of energy occurs, is complex with physical phenomena evolving over a wide range of temporal and spatial scales. By entering in the shallow waters, the incident waves begin to fill the presence of the

seabed and become skewed and asymmetric, due to nonlinear effects. Then, the waves break, undergoing a high energy dissipation before they reach the beach. From the morphological point of view, waves can force both a net onshore sediment transport, in wave-averaged models related to the acceleration skewness (Hoefel and Elgar, 2003; Silva et al., 2011) and a net offshore sediment transport, largely induced by the wave undertow due to braking waves (Roelvink and Stive, 1989; Abreu et al., 2012). The interaction between waves, currents, and sediment transport leads to complex variability in the nearshore bathymetry, which is required to understand and predict all nearshore physical processes.

Since the coast area is highly anthropized and strategic for human activities, the knowledge of the dynamics of the nearshore environment is of great importance from the social, economic, and environmental points of view. For example, bathymetric change prediction is crucial to investigate coastal erosion, flood risk exposure and evaluate hazards associated to safety and infrastructure design and stability. To understand the behaviour of the coastal environmental, accurate physical measurement are necessary.

Traditionally, nearshore physical characteristics have been sampled by means of in-situ instruments, this involving the use of ships, jet skis or amphibious vehicles such as the Lighter Amphibious Resupply Cargo (LARC) and the Coastal Research Amphibious Buggy (CRAB). Shipboard single and multibeam echo sounding or sonar-equipped jet-skis are widely used, as well as monitoring buoys and poles. They can provide highly accurate measurements and are essential to know the hydro-morphological features of the nearshore region. However, traditional methods are expensive, time-consuming, sometimes limited to calm sea conditions and inapplicable to the very shallow waters. This results in spatial and temporal resolution lower than necessary for the observational and modelling needs.

Monitoring the beach behaviour under both seasonal and extreme events is important to facilitate coastal management decisions (Davidson et al., 2007) and also to implement beach nourishment projects (Hamm et al., 2002; Ojeda and Guillén, 2006).

Over the last decades, remote sensing techniques, such as LIDAR, Radar and optical sensors, have been developed as alternative tools to monitor the coastal evolution (Hamm et al., 2002). Remote sensing methods offer the capability to collect a high volume of data at high temporal and spatial resolution with relatively low cost and over a long period. For example, remote sensing techniques can indirectly estimate the water depth and fill spatial and temporal gaps in surveyed bathymetry (Holman et al., 2017). Additionally, remote sensing

methods are not limited by high-energy storms and, therefore, may be employed when more traditional sampling methods must be abandoned.

In general, there are two types of remote sensing technologies: active sensors, such as Radar and Lidar, which emit a signal and evaluate the time delay between emission and return, and passive sensors, which gather the radiation emitted or reflected by an object, such as the sunlight reflected by the sea surface and measured through a camera.

Nowadays, use of imaging methods is very common and in particular optical data are widely employed all over the world. The use of images to study the nearshore zone dates back to the thirties, when aerial photography was first used to map the coastline. Then, coastal remote sensing was developed to quantify hydro-morphodynamic characteristics from shore-based video observations using photogrammetric and computer vision techniques. Since the eighties these new methods developed at the Coastal Imaging Lab (CIL) of the Oregon State University led to the network of the Argus coastal monitoring stations (e.g. Holman and Stanley, 2013) and to the Coastal Imaging Research Network (<https://coastal-imaging-research-network.github.io>). An Argus station is a land-based automated and unmanned station programmed to acquire and return optical remote sensing data in sites of research interest (Holman and Stanley, 2007). It is typically composed of a number of video cameras mounted on an elevated position and connected to a host computer that controls the acquisition and storage of data. The hourly data collection mainly consists of a snapshot image, which shows the general condition, a ten minutes time exposure image, which averages the light intensity signal on each pixel, and the variance image, which shows the variance of the intensity signal during the recorded time. These oblique images can be geo-referenced and rectified using standard photogrammetric techniques to obtain plan view images that allow to quantify the image features. Furthermore, time series of pixel intensity can be collected through specifically-designed sampling schemes.

The first Argus station was installed at Agate Beach on the Oregon Coast in 1992 and presently, shore-based video systems are widely used in coastal research in many locations all over the world. In Italy, the first Argus station was installed in the North Adriatic coast at Lido di Dante beach in 2003 (Archetti, 2009, Armaroli and Ciavola, 2011). Subsequently, other video-monitoring stations, based on EVS (Erdman Video System) were installed in many sites along the peninsula, among others, at Igea Marina (RN), Sabaudia (LT), Terracina (LT), Pineto (TE), Senigallia (AN). These installations have been used to study

the coastline evolution and monitor the effects of nourishment and coastal defence works (Parlagreco et al., 2011). A new video monitoring station, called the “Sena Gallica Speculator” (SGS), was installed in July 2015 at the Senigallia harbour, central Adriatic, as part of the Estuarine Cohesive Sediments (EsCoSed) project (Brocchini et al., 2015). SGS is not part of the Argus network but it was designed on the bases of typical Argus systems. SGS is equipped with four cameras located on the top of a 25m high tower. Unlike Argus stations, which store only single images products and isolated pixel time series, ten minutes of full frame images data are being collected at 2Hz every hour, during daylight hours, and then post-processed. Like other video monitoring stations, SGS aims to support coastal, estuarine, and riverine studies in site of scientific interest.

The concept at the basis of the use of video monitoring imagery to study nearshore processes is that a physical phenomenon can be investigated through images, if it can be discerned visually (Holman et al., 1993; Holland et al., 1997). Fortunately, many nearshore processes have a visual manifestation, therefore the video-monitoring technique provides indirect measurement of the nearshore characteristics. For example, incoming waves are visible on the optical imagery, thus their period, wavelength and direction can be evaluated (Holman and Stanley, 2007). In the same way, preferential breaking areas appear on the time exposure images as bright bands indicating position of submerged sandbar (Lippmann and Holman, 1990). In general, the challenge is to extract accurate quantitative information of hydrodynamic and morphological features from optical signatures visible on the images. In the last decades, many algorithms for the estimation of different nearshore measurements have been developed and currently optical remote sensing is a powerful tool for sampling the nearshore environment (Holman and Stanley, 2007).

1.2.1 Remote sensing for bathymetry reconstruction

Quantifying bathymetric changes is crucial to support navigation and engineering projects, as well as to understand erosion and accretion processes of the beach. Prediction skill of forecasting models increases with more accurate bathymetric boundary conditions (e.g. van Rijn et al., 2003; Holman et al., 2014; Holman et al., 2016). High-resolution coastal elevation data are also necessary to achieve an accurate assessment of coastal flood risk (Beck et al., 2018).

In the last decades, thanks to remote sensing techniques, significant advances have been made in achieving nearshore bathymetry information. Each remote sensing tool has its own accuracy and limitations, and many alternatives are available (Gao, 2009). For clear water columns, where the bottom is visible, Light Detection and Ranging (LIDAR) is an accurate and popular tool to sample the bathymetry (Irish and Lillycrop, 1999). But for turbid water columns, where the bottom is not visible, the LIDAR cannot be used and other methods must be adopted. Another powerful tool to indirectly estimate the bathymetry is the X-band marine radar because wave parameters can be mapped from radar images and used in inversion algorithms based on linear wave theory (Bell, 1999). While the X-band radar can cover areas of a few kilometres giving appropriate results in to the very shallow-water zone, optical videos are typically used to collect data in shallow water because, in view of the high temporal and spatial resolution, they allow to properly extract information also over complex morphologies.

Since in turbid waters the surface signatures dominate, many authors studied the morphology evolution analysing the breaking wave patterns, visible on optical time-averaged images as high-intensity bands (Lippmann and Holman, 1990; van Enkevort and Ruessink, 2001, Aarninkhof et al., 2005). Another particular technique related sub-areal topography to shadows falling across a beach (Holman et al., 1991), while Holland and Holman (1997) have shown how stereo imagery of the moving swash could yield information on foreshore topography. Intertidal bathymetry could be measurement also by mapping shoreline contours over one tidal cycle (Plant and Holman, 1997; Aarninkhof et al., 2003).

Alternatively, nearshore bathymetry can be estimated using depth-inversion algorithms, based on the inversion of the dispersion relationship, which exploits the wave celerity observed by optical imagery. Depth-inversion method is currently one of the most frequently used video-based remote sensing methods to estimate nearshore bathymetry in the presence of surface gravity waves. This approach is based on the linear (e.g. Stockdon and Holman, 2000), nonlinear (e.g. Catálan and Haller, 2008), or extended Boussinesq dispersion equations (e.g. Misra et al., 2003). Two different approaches can be used to estimate the wave celerity, namely the time domain inversion (Almar et al., 2009) and the frequency domain inversion (Stockdon and Holman, 2000). The temporal method computes a time-domain cross-correlation between neighboring positions to estimate the wave celerity

(Almar et al., 2009), while the spectral method uses a cross-spectral correlation to estimate the wave celerity (Plant et al., 2008). Both approaches result in depth estimates with similar accuracy given synthetic optical video data (Bergsma and Almar, 2018). Among the linear depth inversion algorithms that use the spectral method to estimate the wave celerity, the open source depth-inversion algorithm known as cBathy (Holman et al., 2013) (<https://github.com/Coastal-Imaging-Research-Network/cBathy-toolbox>) has become one of the most widely used depth inversion algorithms (e.g. Holman and Stanley, 2013; Radermacher et al., 2014; Sembiring et al., 2014; Méndez et al., 2015; Bergsma et al., 2016; Holman et al., 2017; Rutten et al., 2017; Bergsma and Almar, 2018; Brodie et al., 2018; Zuckerman et al., 2018).

1.2.2 Remote sensing for bar evolution

A very important feature of natural beaches is the presence of particular seabed perturbations called sandbars. A submerged sandbar is a persistent accumulation of sand on the seabed below sea level (Holman and Sallenger, 1993). The nearshore zone of sandy unprotected beaches is often characterized by the presence of these morphological patterns. Some empirical parameters, such as the dimensionless fall velocity Ω (Wright and Short, 1984) and the bar parameter B^* (Short and Aagaard, 1993), can be used to classify beaches where single ($2 < \Omega < 6$) and multiple ($B^* > 50$) sandbars can evolve.

Accurate knowledge of submerged bar behavior is crucial first because sandbars are natural barriers to protect the coast from strong storm actions, which may cause significant beach erosion. Since submerged sandbars evolve in shallow waters, the incoming waves break preferentially near the ridge of the bars, inducing an important dissipation of the wave energy before the waves impact the shore. Such wave energy dissipation is also an important natural protection mechanism that improves the beach resilience. Moreover, for a proper management of sediment budgets, the presence of sandbars must be taken into account, since they involve significant volumes of mobile sand and have an important role on the sediment transport.

Nearshore submerged sandbars can exhibit very complex morphological states. They can occur as a single feature or as a multiple bar system and they can be alongshore uniform (2D bars) or present an intricate alongshore variability (variety of 3D bars). The mutual

interaction between sand transport, waves and currents generate a perpetual variability of sandbar systems, which are characterized by both cross-shore and alongshore motions.

These changes may be affected by single storm events or dominated by seasonal cyclicality. Therefore, the study of sandbar behavior must be carried out analyzing phenomena with time scale varying from hours to months or years. In this respect it is difficult to understand the sandbar dynamics only on the basis of in situ traditional measurement. For these reasons the remote sensing technique may help gather useful information to study sandbar evolution and the related beach morphology. A video monitoring station, in fact, can observe a bar system for a very long period and, at the same time, with an hourly sampling resolution.

Given the scientific and social importance of understanding the behaviour of sandbars and given the potentiality of video monitoring systems, many studies were developed in the past decades to properly identify sandbar features from optical images.

Remote monitoring of sandbar morphology is based on the observation that more waves break over the shallows of the bar than over the surrounding areas (Lippmann and Holman, 1990). Time exposure images, which are a classical product of video-monitoring stations, are a useful tool to highlight wave breaking patterns, because the areas of preferential breaking are displayed on these images as white bands. Lippmann and Holman (1990), first developed a technique that allows to estimate the sandbar position on the basis of the patterns of incident breaking waves. Their assumption is that light intensity recorded on the camera varies with the dissipation of the incident wave energy and they regarded the energy dissipation as a proxy to measure of bottom topography (Lippmann and Holman, 1990). Many approaches to sample bar crest location from images have been developed since then. A widely used algorithm, implemented also in the Argus toolbox Barline Intensity Mapper (BLIM), is the algorithm developed by Van Enkevort and Ruessink (2001).

This technique provides quantitative information on both cross-shore and longshore bar crest location and is commonly used to monitor submerged bar systems and nourishments in countless sites all over the world. The accuracy of video-based estimation of the bar location depends on the relationship between the maximum video image intensity and the seabed morphology and should be evaluated for each particular site. Focusing on the Mediterranean area, Ribas et al. (2010) confirmed the suitability of the video-monitoring technique to study bars and terraces on the micro-tidal beach of Barcelona. In the present thesis the barred

beach of Senigallia (Italy) is studied using the optical data coming from the new video-monitoring station, SGS.

Chapter 2 The Study Area

2.1 The Senigallia Beach

The Italian coast of the central Adriatic Sea is predominantly characterized by sandy and low-sloped beaches periodically separated along the coast by the mouths of rivers that flow from the mountains to the sea, in west-to-east direction. The coastline is highly anthropized and the beach is commonly used for commercial and touristic activities. To preserve the littoral area from both inundation and erosion risks, a number of hard defence structures were placed along the coast over the years. This thesis focuses on a stretch of coastline representative of those Adriatic beaches that are near to river mouths.

The study area is located in Senigallia (AN, Italy) about 30 km north of the Conero promontory. The coast is characterized by a very mildly sloping sandy beach and extends on southern side of the Senigallia Harbour, from the jetty to the Rotonda pier (Figure 2-1).

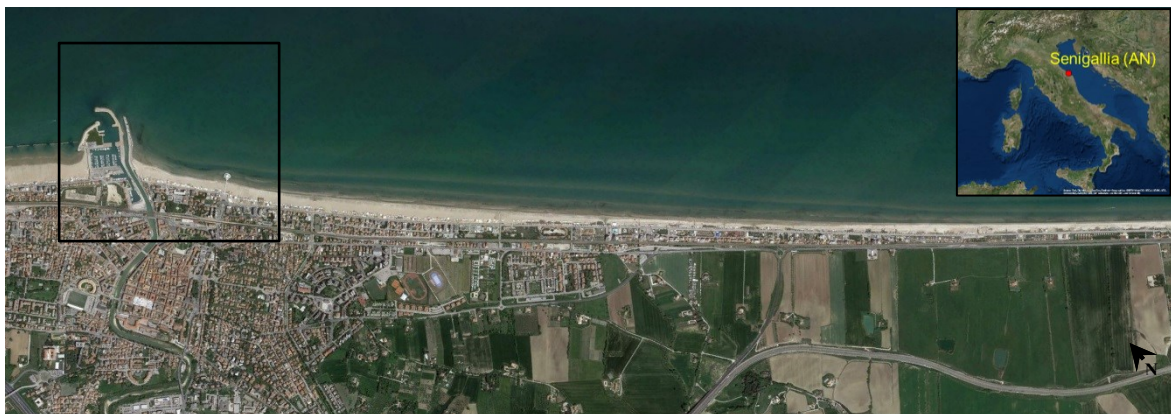


Figure 2-1. Satellite view of the unprotected coast near Senigallia. The up-right box shows the location of Senigallia Beach. The black box highlights the study area.

This area is the northern portion of a 12 km long stretch of natural coast, one of the few stretches of the Region coastline not protected by hard defence structures. Hence, the area represents a good site to study coastal processes typical of the Central Adriatic coast.

Moreover, the port of Senigallia is a typical Canal Harbour due to the presence of the mouth of the Misa River, and this allows to study also riverine and estuarine processes.

The coastline of the analysed area extends in the north-south direction with a rotation of about 47° from the north (Figure 2-2). The observed beach is characterized by medium ($D_{50} = 0.25\text{-}0.5\text{mm}$) to fine ($D_{50} = 0.125\text{-}0.25\text{mm}$) sand in its emerged profile and by fine sand in its subaqueous part. The sediment size of the submerged beach decreases moving southward. The swash zone is characterized by slopes ranging from 1:30 to 1:40 with an array of submerged bars in water depths 0 to 3 m. Depths deeper than 3 m are characterized by slopes of 1:200 (Postacchini et al., 2017).

The beach of Senigallia is a wave-dominated and micro-tidal environment (tide range $< 2\text{m}$) with sea level ranging between -0.6 m and $+0.6\text{ m}$ and a maximum tidal excursion that does not exceed 60 cm. Information of tide levels is obtained from a tide gauge located inside the Ancona Harbour and part of the Italian National Tide Gauge Network (RMN).

The study area is constrained by two rigid structures: the Senigallia Harbour in the northern part and the Rotonda pier in the southern part. The presence of the Rotonda pier does not significantly affect the evolution of the beach while the larger jetty of the Harbour induces a curvature of the shoreline in the northern part of the domain. The presence of the Harbour complicates also the hydrodynamics of the area because the waves coming from the ESE direction impact onto the walls and there get reflected.

The sediment transport of this area is influenced by both the wave motion and the Western Adriatic Coastal Current (WACC) that drives the sediment southward (Harris et al., 2008; Sherwood et al., 2004). Moreover, the freshwater discharge of the Misa River estuary transports sediments down to the river mouth and to the nearshore region, especially during the wintertime (Brocchini et al., 2015; Brocchini et al., 2017).

2.1.1 Wave climate

Knowledge about the wave climate of the analysed area derives from historical time series collected by the Ancona buoy of the Italian Data Buoy Network (RON). The Ancona buoy (red circles in Figure 2-2) was installed in March 1999, at around 30 km far from the shore, its location been slightly modified during 2000. The available data consists of two time series: from 1999 to 2006 and from 2009 to 2013. The buoy is currently out of service.

Previous studies (Postacchini et al., 2017) evaluated the overall wave climate on the bases of the significant wave height, peak period and direction provided by the Ancona Buoy every half hour. They highlighted that the wave climate in Senigallia is characterized by storm waves coming from two main directions: ESE (forced by Scirocco winds) and NNE (forced by Bora winds). The Bora is a cold wind very frequent and intense during winter. Given the narrow and elongated shape of the Adriatic Sea this wind has a relatively short fetch and generates short, steep and high waves that propagate almost perpendicular to the coast. The Scirocco is a warm wind coming from south-east and approaching the coast with wide angles. It has a longer fetch that allows long and less steep waves. It is common during summer and it is characterized by a surge larger than that typical of the Bora storms. Moreover, the storms coming from ESE are more suited to produce infragravity waves (Brocchini et al., 2017). These two types of storms are not a seasonal characteristic (summer condition -winter conditions). On the opposite, storms with different directions, due to an alternation of Bora and Scirocco winds, can occur during the same season. In general, wintertime is characterized by severe storm events while the summertime generally has milder wave conditions.

Since the Ancona Buoy stopped working in 2013 the data coming from the new video monitoring station (installed in 2015) must to be correlated with other available data sets of wave characteristics.

The closest location where wave time series are collected is at Cesenatico (Cesenatico Buoy in the Emilia Romagna Region). It is located 80 km north of Senigallia, at a distance of 8 km from the beach and placed in 10 meters deep waters. Unfortunately, results of wave frequencies and the inspection of the simultaneous wave time series collected in Ancona and Cesenatico reveal significant differences in the wave climate. Specifically, the waves at Cesenatico come mainly from the northeast sector, while the Ancona climate is characterized by the mentioned two main wave directions. Furthermore, the Cesenatico Buoy is located in shallower waters than the Ancona Buoy; therefore, the waves incoming from different sectors are rotated by refraction and focused in the cross-shore direction.

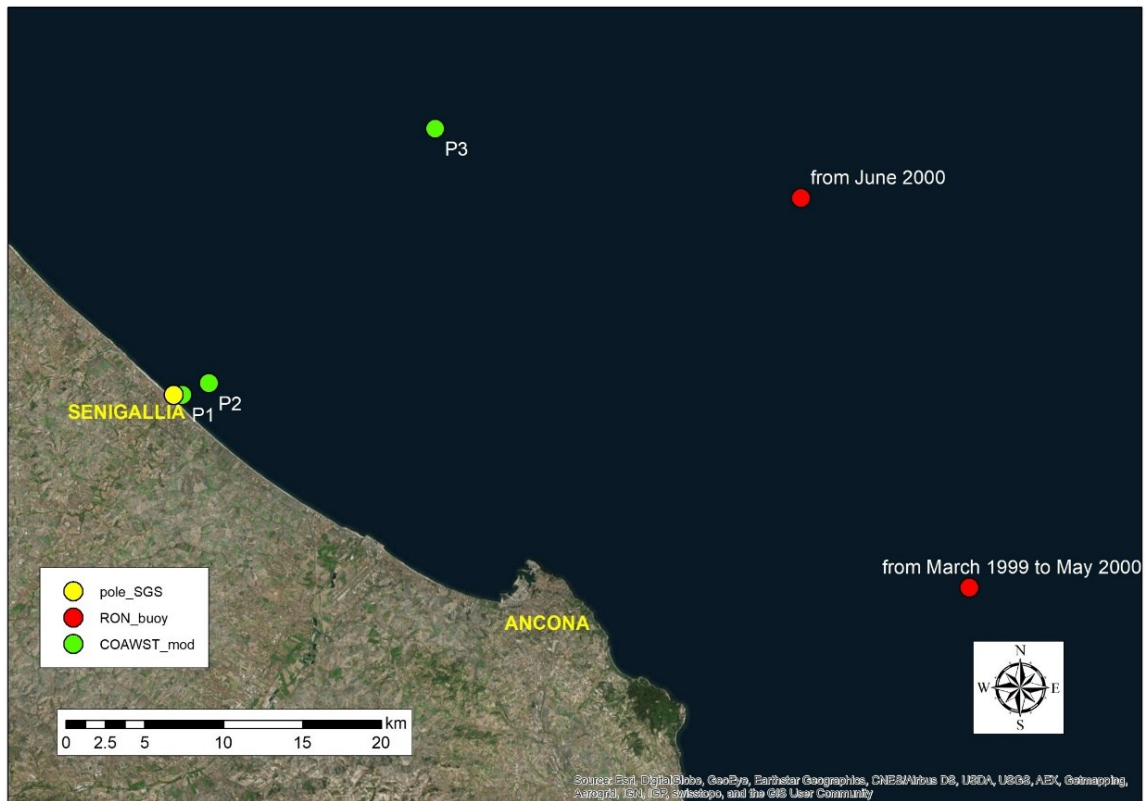


Figure 2-2. Location of the Senigallia beach (yellow circle), location of the Ancona RON buoy (red circles) and location of the points of the COAWST model (green circles).

Another opportunity is to use data extracted from the COAWST Model, a global circulation model available for the Adriatic Sea. COAWST is a Coupled Ocean–Atmosphere–Wave–Sediment Transport modelling system based on the Regional Ocean Modelling System (ROMS) and Simulating Waves Nearshore (SWAN) system. The model covers the northern Adriatic Sea and it has a grid resolution of 1 km. Three points of the model grid are analyzed in the present thesis: P3, P2 and P1 placed on waters of 50 m, 10 m and 5 m depth, respectively (Figure 2-2). Time series of the root-mean-square wave height, peak wave period and angle of wave incident with respect to north are available from 2015 to 2017. A comparison of the wave frequency distribution with reference to the direction of propagation available from the Ancona Buoy and COAWST (plotted with red lines in Figure 2-3), reveals that the model correctly reproduces the typical distribution of waves for this site. However, the distribution of the wave energy flux (represented with blue lines in Figure 2-3) predicted by the model is mainly concentrated from NNE and ENE, while no storms were generated by the Scirocco wind, which are typically the most energetic storms for that area. This may be related to the reduced length of the modelled time series. In fact, the wave

climate of this area has not a seasonal behaviour and some differences in frequency distribution of the wave energy flux can occur from year to year. Analysing in more detail the single years, we find that only in 2016 a 5% portion of the wave energy came from the ESE direction. In view of the above, the data extracted from the COAWST model have been mainly used for the analyses that follow.

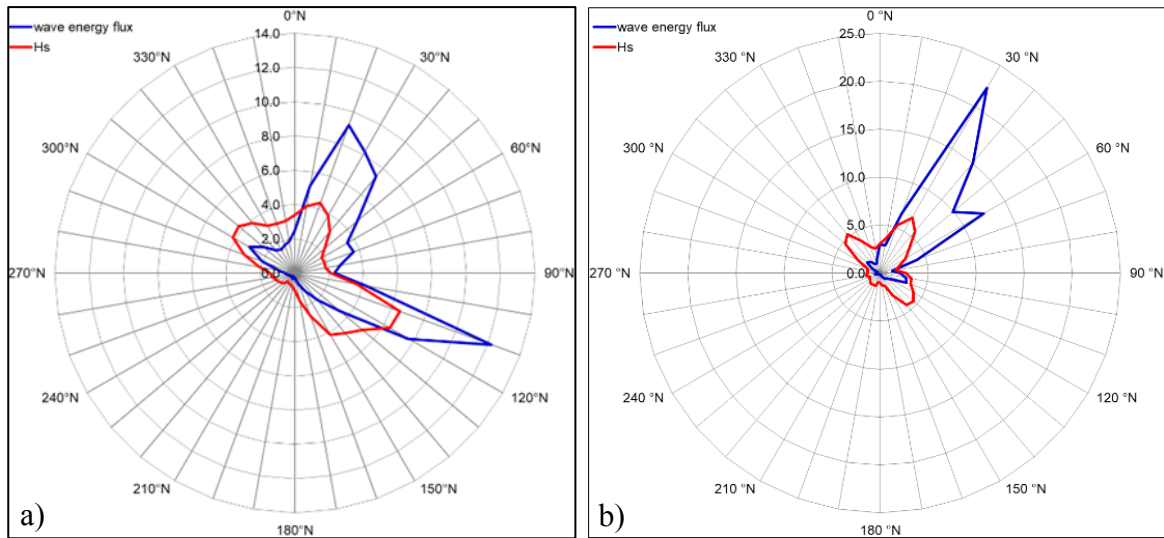


Figure 2-3. Frequency distribution of significant wave height (red line) and wave energy flux (blue line): (a) RON buoy 1999-2006 & 2009-2013. (b) COAWST model 2015-2017, P3.

From June 2018 a new data set of wave characteristics has become available from the Meda Station. The Meda Station is part of the weather monitoring network of the ISMAR, the Italian Institute of marine science. It was installed in July 1988 and it is located at around 1.2 nautical miles from the Senigallia coast, at around 12 m water depth (43 45.350N - 013 12.540E WGS84). The station traditionally collects weather and oceanographic data such as the velocity and the direction of the wind, atmospheric pressure, temperature and salinity of the sea water. At the end of May 2018, thanks to a collaboration between ISMAR and the Department of Civil and Building Engineering and Architecture of the Università Politecnica delle Marche, funded within the ONRG-MORSE project, a new ADCP was installed to measure wave characteristics. Therefore, beyond other collected data, the significant wave height, wave peak period and wave peak direction are now available. Figure 2-4 shows the time series of the main characteristics of the waves currently collected by the Meda Station. These measurements are available from June 2018 to October 2018.

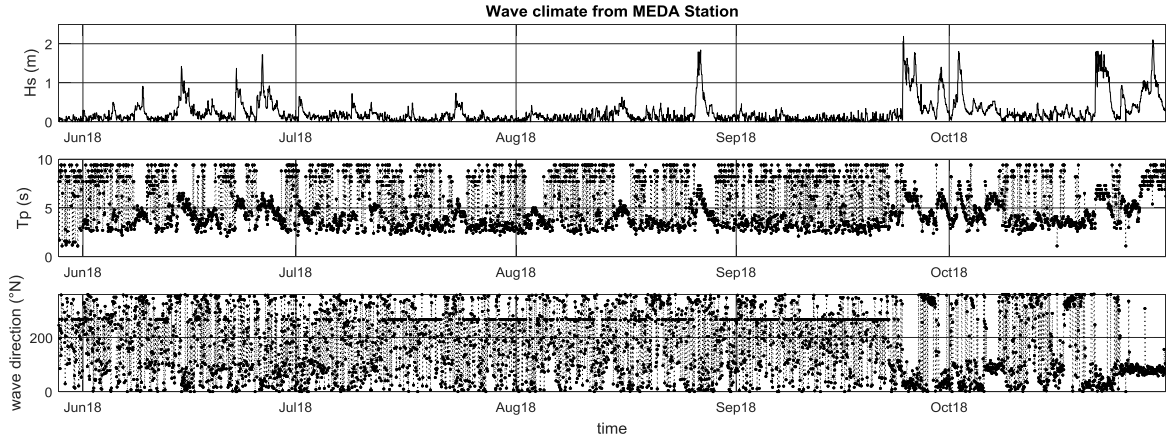


Figure 2-4. Time series of wave characteristics collected by the Meda Station from June 2018 to October 2018. The upper panel shows the significant wave height, the middle panel shows the wave peak period and the lower panel shows the wave peak direction.

2.1.2 Bathymetric features

A general description of the morphology of the beach can be carried out by means of synthetic parameters, such as the dimensionless fall velocity Ω^* (Wright and Short, 1984), the bar parameter B^* (Short and Aagaard, 1993) and the relative tide range RTR (Masselink and Short, 1993), which allow to classify the state of the beach:

$$\Omega^* = \frac{H_b}{w_s T}, \quad (2.1)$$

$$B^* = \frac{x_s}{g m T^2}, \quad (2.2)$$

$$RTR = \frac{TR}{H_b}, \quad (2.3)$$

where H_b is the breaking wave height, T is the wave period, x_s is an offshore distance corresponding to a specific depth at which the beach slope becomes very small, g is the gravitational acceleration, m is the bottom slope and TR is the tide range. The settling sediment velocity, w_s , was evaluated with the Zanke (1977) formulation, valid for sediment diameters in the range $0.1 \text{ mm} - 1 \text{ mm}$:

$$w_s = 10 \frac{v}{D_{50}} \left(\sqrt{1 + \frac{0.01 g D_{50}^3 (\rho_s - \rho_a)}{v^2 \rho_a}} - 1 \right) \quad (2.4)$$

where ν is the kinematic viscosity of water, D_{50} is the sediment median-diameter, ρ_s is the particle density, ρ_a is the water density. Using $\nu = 10^{-6} \text{ m}^2/\text{s}$, $D_{50} = 0.2\text{mm}$, $\rho_s = 2650 \text{ kg/m}^3$ and $\rho_a = 1000 \text{ kg/m}^3$, the settling velocity is $w_s = 0.0257 \text{ m/s}$.

For a general classification, frequent values of the above-mentioned quantities are used. In particular, for a typical storm condition it is $H_b = 3 \text{ m}$, $T = 7.5 \text{ s}$, $x_s = 600 \text{ m}$, $m = 0.0062$. Therefore, the mentioned synthetic parameters are: $\Omega = 15.5$, $B^* = 175$ and $RTR = 0.2$. Using mean wave condition ($H_b = 1\text{m}$ and $T = 7 \text{ s}$), the mentioned synthetic parameters are: $\Omega^* = 5.5$, $B^* = 200$ and $RTR = 0.6$.

The dimensionless fall velocity, Ω^* , takes into account both wave characteristics and sediment characteristics (Wright and Short, 1984). Values that exceed 6 are traditionally correlated with dissipative conditions and a stable morphodynamic state. In this kind of environment submerged bars may be present and rips are usually absent (Masselink and Short, 1993). Following the conceptual beach model of Masselink and Short (1993), who analysed also the role of the tide, the above calculated values of dimensionless fall velocity, Ω^* , and relative tide range, RTR , allow to classify the beach of Senigallia as a barred dissipative beach. The possible number of sandbars may be predicted using the dimensionless bar parameter, B^* , which takes into account both the nearshore geometry and wave period (Short and Aagaard, 1993). The value of B^* estimated for the Senigallia beach, indicates the likely presence of three bars.

The results of this simple empirical analysis are confirmed by the morphological features observed by in-situ surveys. The beach of Senigallia was frequently sampled with traditional bathymetric surveys over the last two decades, also thanks to the monitoring program established to control the effects of the port expansion works.

In June 2006, the Marche region promoted a topographic and bathymetric monitoring plan for an area spanning 4.3km in the longshore and reaching a depth of 6m. The topographic survey was performed over the emerged part of the beach, the swash zone and for the first meter depth of the submerged beach. The sampling of the shoreline was made during calm sea conditions and the survey was executed along sections perpendicular to the coast, spaced of about 50m. At the same time, a bathymetric survey was performed for the submerged part of the analysed area by means of a Multibeam system with high accuracy (5cm RMS). The data acquisition system produced a three-dimensional digital terrain model (DTM).

Between 2010 and 2013, after the modification of the harbour entrance, four annual bathymetric surveys were performed: in February 2010, in February 2011, in April 2012 and in May 2013. These surveys were promoted by the Municipality of Senigallia and were carried out for a longshore length of 2.5km, up to the bathymetric of -6m. Also in these cases, digital terrain models were obtained. Then, using ESRI ArcGIS 9.3, 18 cross-sectional profiles were extracted. The first 8 transects have been used in the present thesis as bathymetric benchmarks for the performed analyses.

The bathymetries surveyed in 2006, 2010, 2011, 2012 and 2013 have shown a general invariance of the seabed profile and the presence of a system of three submerged sandbars in a water depth of around 0-3m (Soldini et al., 2014; Postacchini et al., 2017). The short-to medium-term variability observed in the surveys is related to the evolution of submerged bars but the previous analyses did not resolve the storm-time variability of the bar system, which needs to be further investigated. Instead, the long-term stability of the seabed has been confirmed by a good adaptation of the beach to the Dean-type equilibrium profile (Soldini et al., 2014). The equilibrium beach profile (Dean, 1991) describes the balance of a shore-normal transect of a natural beach between erosive and accretive forcing:

$$h = A x^n \quad (2.5)$$

where h is the still-water depth and x the cross-shore coordinate. The constant n is equal to $2/3$ (Dean, 1991), while the dimensional shape parameter A can be directly related to the median grain diameter (Hanson and Kraus, 1989). The A parameter can also be calculated from experimental data, by means of techniques of best fitting.

Figure 2-5 shows an example of the DTM obtained from an in-situ bathymetric survey (May 2013) and the variability of the beach cross-shore profiles, which also display the long-term stability of the beach and the short-term variability of the bar system.

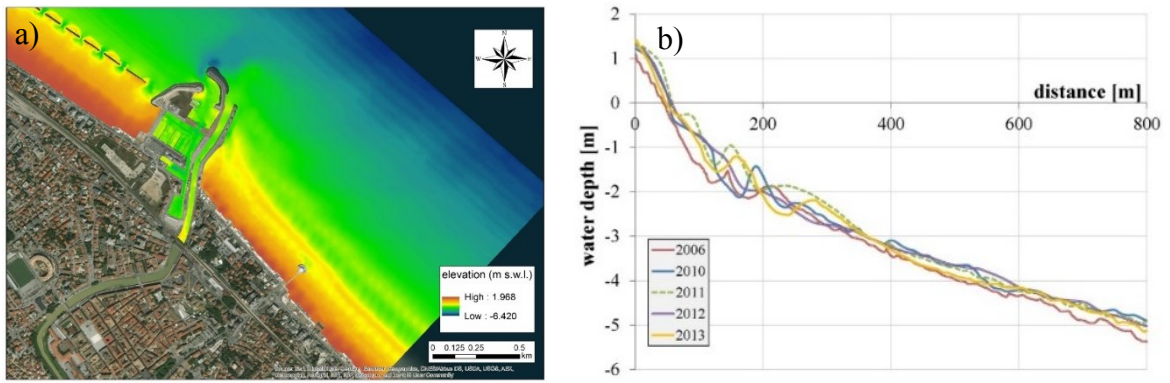


Figure 2-5 - (a) Bathymetric survey of the study area, May 2013. (b) Changes of the cross-shore profile highlighted from the available surveys.

Chapter 3 The SGS Station

3.1 Features and installation

A new shore-based video monitoring station was designed to monitor the nearshore area of a typical beach along the Middle Adriatic Sea. It was installed at the Senigallia town with the aim to observe both an unprotected stretch of a low-sloped sandy coast and the downstream part of an estuary. The station is named Sena Gallica Speculator (SGS) from the Latin name of this site.

The SGS station was installed in July 2015 as part of the Estuarine Cohesive Sediments (EsCoSed) project (Brocchini et al., 2015). The installation has been made possible thanks to the collaboration between the Department of Civil and Building Engineering and Architecture of the Università Politecnica delle Marche and the U.S. Naval Research Laboratory. The objective of the EsCoSed project was to better understand coastal, estuarine, and riverine processes at the Misa River mouth. For this purpose, also two field experiments were performed to investigate summertime (September 2013) and wintertime (January 2014) conditions (Brocchini et al., 2015; Brocchini et al., 2017).

The SGS station is part of the Coastal Imaging Research Network (CIRN), which grew out of the Argus camera system from Coastal Imaging Lab at Oregon State University. It has drawn inspiration from the classical Argus station structure but it is not part of the Argus Network. The main differences with traditional Argus stations regard the type of data storage and the logistics of the archive. In contrast to traditional Argus imaging stations, which collect only subsampled pixel time series, full frame video data are collected from this facility. The raw video data are then elaborated in post-processing. This allows gathering more general information that can be differently processed on the basis of the specific study at hand, but, obviously, this generates also the logistics issue of storing such large data volumes.

The SGS station is designed to be a long-term facility. It is located at the North pier of the port channel of Senigallia (Figure 3-1). The importance of the location is related to the possibility to observe both the nearshore and the estuary of the Misa River. The station is mainly composed by four cameras located on the top of a tower, at 25m above mean sea level (Figure 3-1). Three cameras face South toward the 500 m long unprotected beach between the harbour jetty and the Rotonda pier, this allowing to study the hydro-morphodynamics of the nearshore zone. The fourth camera faces northward toward the estuary of the Misa River; therefore the data recorded by the cameras represent a major source of information to improve also knowledge on estuarine dynamics.

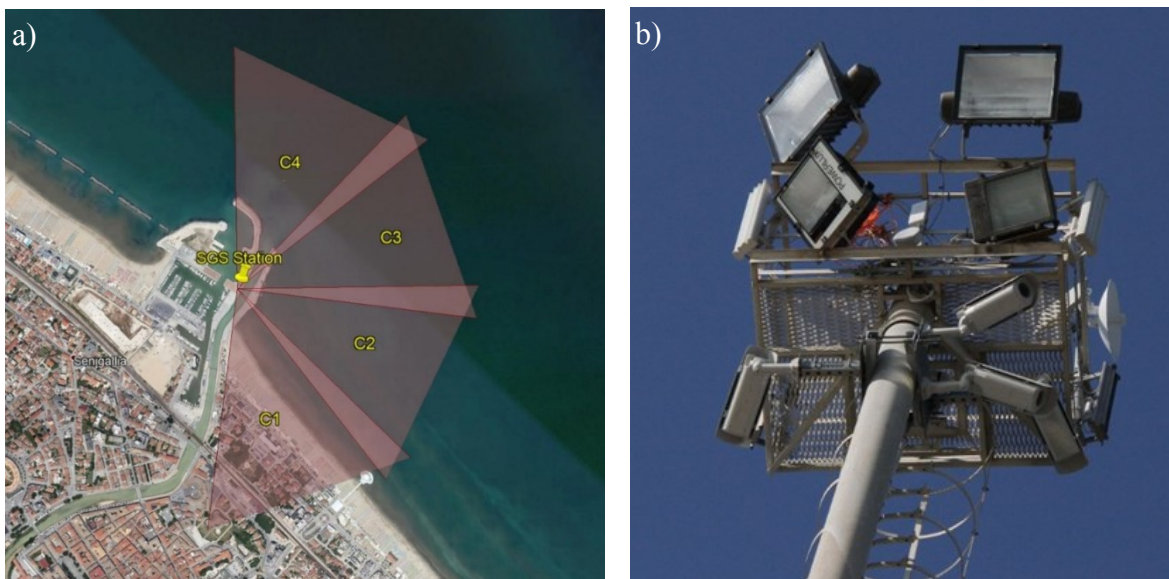


Figure 3-1 - a) General view of the Senigallia harbour showing the SGS Station position and the cameras field of view. b) The four cameras installed on the top of the tower.

The four cameras installed on the top of the tower are FLIR/Point Grey Grassopher3 with 9 MP resolution (3376×2704). The lenses are CF12.5HA-1 with 12.5 mm focal length and 49 mm linear polarizing filter. The cameras are placed inside CRONO CPK405PoE housings (Figure 3-2). The camera field-of-view is 53° for an overall angle of 200° . The resolution is between 0.05 m and 0.50 m and the useable distance is 700 m. Particular attention was made to obtain a suitable overlap of the field of view of each single camera. In November 2016, the cameras have been rotated to better superpose the fields of view and not lose information.



Figure 3-2 – Particulars of the camera installation.

Through a pair of cables, the camera system is connected to a communication box located 60 m far from the tower, where an external trigger (custom built by Naval Research Lab, US) synchronizes the camera acquisition (Figure 3-3). Then the system is linked to a computer where a software (Streams 7) controls the data collection and archive (Figure 3-3).



Figure 3-3 – a) Communication box. b) Camera trigger. c) Computer station.

For each recording hour, the data collected from each camera consists in a video and a snapshot. The acquisition occurs during daylight hours, from 5:00 AM to 5:00 PM UTC, for a total of thirteen videos and thirteen snapshots a day, for each camera. A video consists of the first ten minutes of an hour and it is collected at 2Hz. The Snapshot image is the first frame of a video and it is saved to get a rapid overall visual assessment of the dataset. Videos and snapshots are temporarily stored on a 8TB external drive and periodically uploaded on a repository server located at the Università Politecnica delle Marche. The data recorded from the cameras are archived based on typical storage and file naming Argus convention. A large amount of data is already available and it grows every day as the station is currently working. From 2015 to 2017 the gaps of the data collected from the SGS station were around 20% of the total number of days.

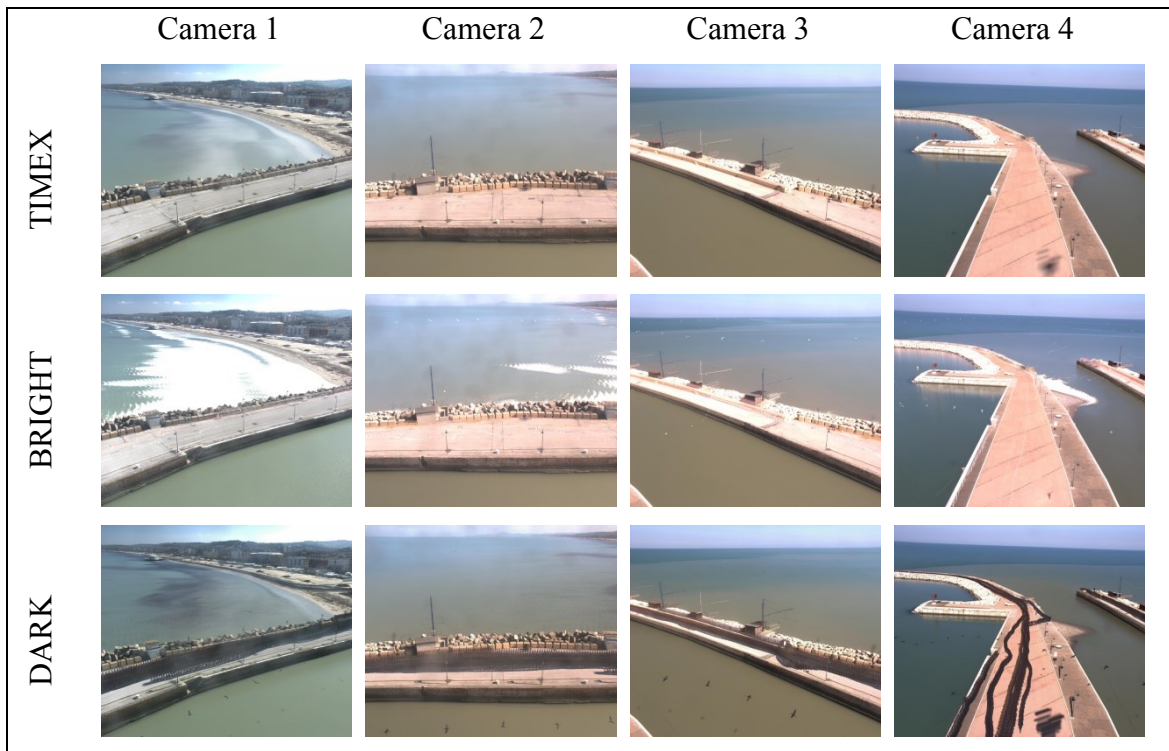
3.2 Data post processing

The hourly videos and snapshots recorded from the SGS station are post-processed using the Argus Database, the CIL toolbox and some custom Matlab© Codes. The post-processing of the SGS raw data includes the production of classical Argus images.

First, the videos of each hour and each camera, are elaborated to obtain a 10-minute time-exposure image, a darkest image, a brightest image and a full time series from the recorded period for a selected grid of pixels. In a second step, the processed images, together with the snapshots, are merged and ortho-rectified to obtain other five products per hour: a panoramic image and four (snapshot, time-exposure, darkest and brightest) plan view images. All these productions generated a continuously updated database (Table 3-1, Figure 3-5, Figure 3-7). These post-processing analyses are currently performed from July 2015, when the camera started to work, to November 2017.

More in detail, the time exposure (or Timex) images are created by averaging the intensity values of each pixel over the 10-minute sampling period (Table 3-1).

Table 3-1 Examples of post-processed images (13 March 2017 h 13.00)



In this way moving features, such as individual waves, are not visible but more stable characteristics are highlighted, like regions of wave breaking, which are visible on this image as bands of high intensity values. Some previous studies suggested to average day's Timex images to avoid a shift of the cross-shore position due to the tide (Holman and Stanley, 2007). Since the Senigallia coastal area is microtidal ($RTR < 2$, see Chapter 2), day-Timex are not created. Darkest (Dark) and brightest (Bright) images are created by saving the lowest and highest intensity value in each pixel over the sampling time. An example of these kinds of images is reported in Table 3-1.

Knowledge of real-world coordinates of physical features sampled on the images is crucial to extract quantitative information from optical data. Therefore, the photogrammetric transformation between 3D world coordinates (X, Y, Z) and 2D image coordinates (U, V) must be well defined. This aspect was well studied for Argus applications (Holland et al., 1997) and is currently evaluated in depth for new applications with quadcopters (Holman et al., 2017).

The used photogrammetric relationship is based on Hartley and Zisserman (2003) formulation and uses the concept of homogeneous coordinates that allows doing rotation and translation by matrix multiplication. The transformation between real and image coordinates can be, therefore, expressed with Equation (3.1), considering a single camera.

$$\begin{bmatrix} U \\ V \\ 1 \end{bmatrix} = P \begin{bmatrix} X \\ Y \\ Z \\ 1 \end{bmatrix} \quad (3.1)$$

P is the projection matrix and it can be explicated through three matrices:

$$P = KR[J] - C \quad (3.2)$$

where K is the intrinsic matrix describing the camera system, R is the rotation matrix between a real coordinate system relative to the camera system and a global coordinate system (the WGS84-UTM in this thesis) and the bracketed terms is the identity matrix (J) added to the vector of camera centre in world coordinates (C).

The total projection matrix is defined by means of 11 unknown parameters.

The intrinsic matrix (Equation 3.3) is a function of the physical characteristics of the camera, which are the geometric image centre coordinates (U_0, V_0) , the focal lengths (f_U, f_V) and the image skewness (s_k) . The latter parameter is usually ignored and set equal to zero.

$$K = \begin{bmatrix} f_U & s_k & U_0 \\ 0 & f_V & V_0 \\ 0 & 0 & 1 \end{bmatrix} \quad (3.3)$$

These 5 parameters are function of camera lens and hardware and are not a function of the camera installation. Therefore, these unknowns can be found by an intrinsic calibration in the laboratory, before in-situ camera installation.

The rotation matrix can be described by the camera rotation angles (azimuth, tilt and roll), while the camera centre is identified by three global coordinates. All of these 6 unknowns are extrinsic parameters, function of the camera installation, and can be obtained using the Ground Control Points (GCPs). GCPs are visible points whose world locations are known by dedicated surveys and whose image locations can be found from the images. Some GCPs sampling used to post-calibrate the four cameras of the SGS station are shown in Figure 3-4.



Figure 3-4. Plan view location of the GCPs surveyed by means of the GPS technology.

Using GCPs, the 6 unknowns can be found by a nonlinear solver, comparing measured and predicted image coordinates for a guess at the extrinsic parameter.

Each GCP gives two coordinates, so three or more non collinear GCPs are necessary to define the projection matrix. More GCPs lead to an overdetermined system that allows to solve the problem in the least-squares sense. Sometimes, it is not easy to find or place enough GCPs, especially using drones or unmanned aerial vehicles. It is possible to reduce the number of necessary GCPs by assuming that some parameters are known. For example, the camera location may be determined by GPS surveying (more information in Holman et al., 2017). For the SGS station, the transformation between Ground Control Points (GCPs) in world coordinates (WGS84-UTM) and the corresponding image coordinates was determined through standard photogrammetric and computer vision techniques.

Holland et al (1997) reformulated the camera model in an alternative, but equivalent, methodology based on 11 parameters (so called m-vector). During the post-processing analysis of the SGS data the m-vector approach was used.

It is important to observe that the photogrammetric relationship allows for the transformation between world (3D) to image (2D) coordinates, but the opposite conversion gives an under-determined system. This problem is usually overcome by fixing a real coordinate. Commonly the z-coordinate is assumed to be equal to the measured tidal level. Since the Senigallia beach is a microtidal environment, the z-coordinate was assumed to be equal to zero.

Together with the snapshot, the three oblique images elaborated in the first step of the post-processing (Timex, Dark, Bright) were geo-rectified using the photogrammetric method. For each hour and each type of image, the four ortho-rectified images of the four cameras are merged obtaining the plan view images, the so called ortho-rectified images (Figure 3-5).

The geometry solution calculated for each camera usually remains unchanged if the camera orientation is not modified (in November 2016 the geometry of the SGS cameras was changed) and the same transformation is used for the whole dataset. Even if the cameras move slightly, for example because of temperature differences or wind, commonly this does not affect the accuracy of the results. But, for the specific case of the SGS station sometimes the above-mentioned effects might be important. Therefore, different stabilization methodologies were explored and the following procedure was adopted for some specific analyses.

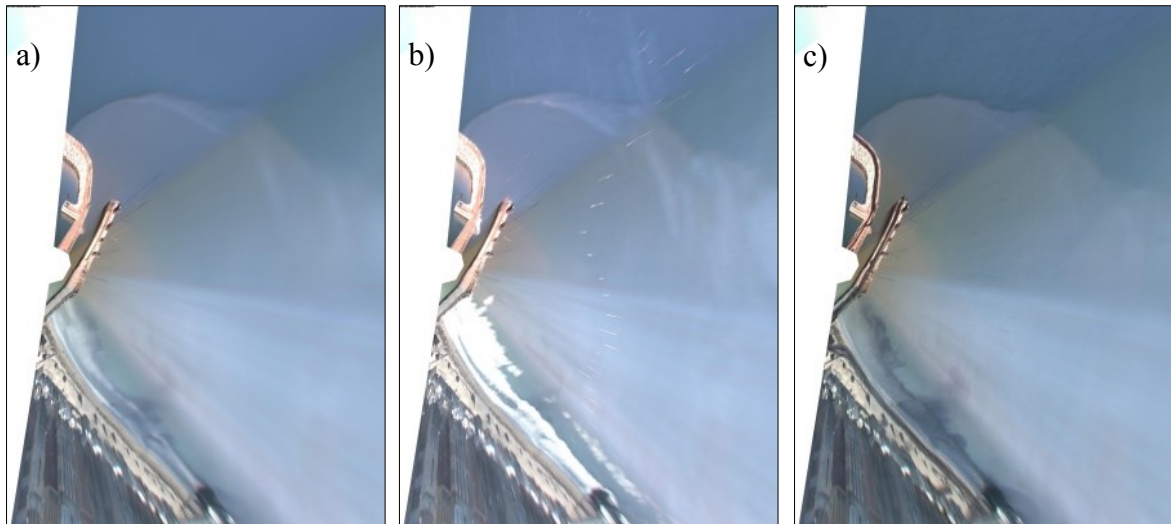


Figure 3-5 – Merged and orthorectified images: a) Timex, b) Bright, c) Dark.

To avoid errors on the time series, a video stabilization was implemented on the code that reads the video and builds the time series. For each analysed video, the geometric transformation that aligns the first frame of the video with a target image was estimated and applied to all the frames of the video. The image target was the snapshot of the day when the geometry was calculated. The movement of the cameras over the ten recorded minutes was neglected. This methodology was carried out to evaluate errors in the bathymetry estimation (Section 4.3.1).

To avoid errors in the location of the sampling of morphological characteristics in the time exposure images, image stabilization was implemented on the code that merges Timex images. For each hour and each camera, the geometric transformation between the analysed Timex and the Timex image of the day when the geometry was calculated (target Timex) was estimated and applied to the analysed image (Figure 3-6). Then the Timex of the four cameras were merged to obtain a stabilized ortho-rectified Timex image. These kinds of images were used for the analysis of underwater bar evolution (see Chapter 5).

The beach of Senigallia is not perfectly aligned with the North-South direction, therefore to easily study nearshore phenomena a rotated coordinate system was used. In general, for the SGS data two different real-world systems have been adopted. The first one is the global world coordinate system (WGS84-UTM), the second one is a local coordinate system with the y axis aligned with the shoreline and positive towards the Rotonda pier, and the x axis aligned with the cross-shore direction and positive in the offshore direction. The origin of the local system is a GCP near the Rotonda.

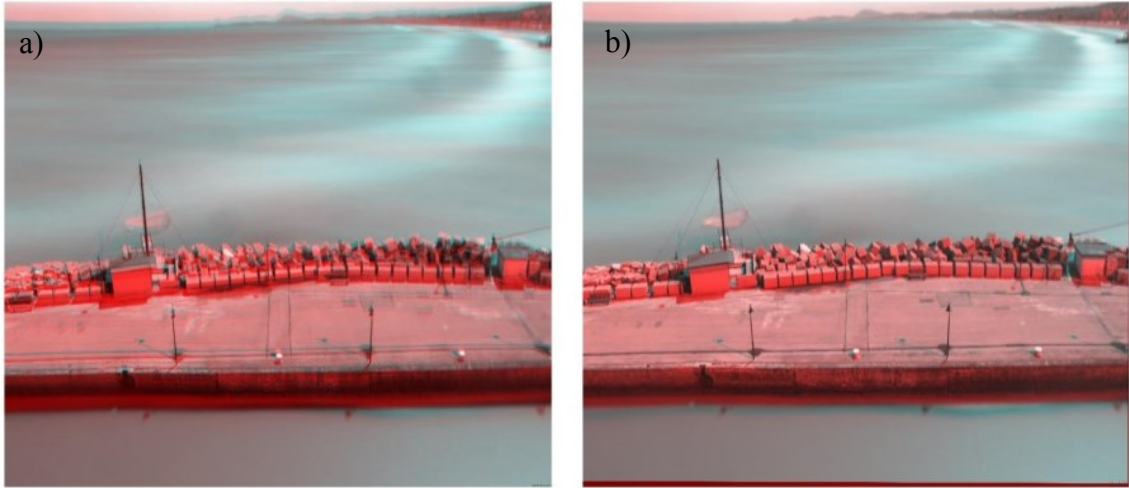


Figure 3-6 Example of stabilization effects. a) Target image (red) superposed to moving image (cyan). b) Target image (red) superposed to stabilized moving image (cyan).

The transformation between global coordinates and local coordinates was determined by means of a roto-translation matrix defined as

$$rM = \begin{bmatrix} \cos(\vartheta) & -\sin(\vartheta) & x_0 \\ \sin(\vartheta) & \cos(\vartheta) & y_0 \\ 0 & 0 & 1 \end{bmatrix} \quad (3.4)$$

where $\vartheta = -47.5637^\circ$ is the rotation angle between the global and local coordinates, $x_0 = 357026.367$ m and $y_0 = 4841854.962$ m are the global coordinates of the origin of the local coordinate system.

In the local system, a subsampling grid was designed, with a 3m resolution. Then, the coordinates of this grid were transformed into global and image coordinates and the corresponding intensity pixels were extracted from the videos. The time series of the image intensity values sampled for the point of the grid is called a Timestack, according to the typical Argus nomenclature. Figure 3-7 shows an example of intensity time series for a shore-normal cross-section in which the main characteristics of wave breaking, wave phase speed, and wave run-up can be quantified.

In the present thesis, the Timestack has been used to indirectly estimate the bathymetry (see Chapter 4) and the stabilized time-exposure plan view images have been used to estimate the sandbar locations (see Chapter 5). At this time, the other post-processing products are used only for a qualitative assessment of the evolving dynamics.

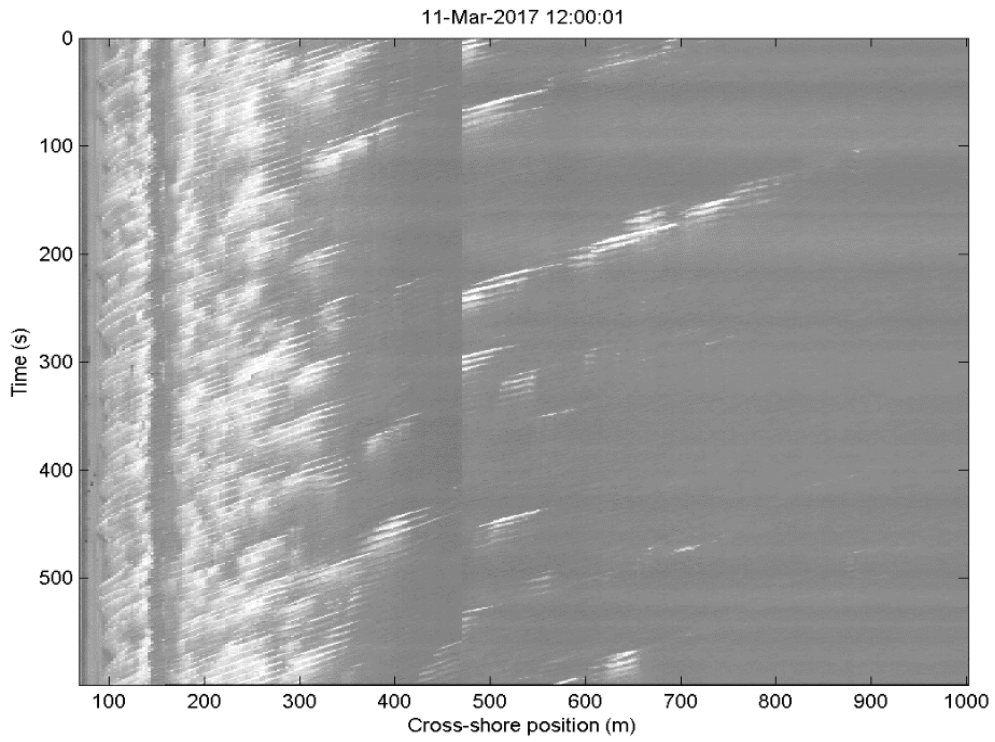


Figure 3-7 – Example of a Timestack where the wave propagation and the swash motion ($50\text{m} < x < 100\text{m}$) are well visible.

Chapter 4 Bathymetric Analysis

4.1 cBathy Algorithm

cBathy is a data-assimilation algorithm, developed by Holman et al. (2013), to estimate the nearshore bathymetry. It is based on the inversion of the linear depth relationship, it uses a spectral method to estimate the wave celerity and a Kalman filter to assimilate new bathymetry estimates. cBathy can be used with all types of optical imagery, such as pixel data coming from fixed cameras, radar images or data collected by any other sensors. It is an accurate and robust algorithm and provides frequent bathymetry estimations and confidence intervals that can be used also in nearshore prediction models.

Among the depth-inversion algorithms, cBathy has become one of the most widely used (e.g. Holman and Stanley, 2013; Radermacher et al., 2014; Sembiring et al., 2014; Méndez et al., 2015; Bergsma et al., 2016; Holman et al., 2017; Rutten et al., 2017; Bergsma and Almar, 2018; Brodie et al., 2018; Zuckerman et al., 2018). The original code of cBathy (cBathy v1.1) and an updated version (cBathy v1.2) are currently available on the CIRN GitHub repository (<https://github.com/Coastal-Imaging-Research-Network/cBathy-toolbox>). The Coastal Imaging Research Network (CIRN) is an international group of researchers working with remotely-sensing data techniques for the study of coastal, estuarine and riverine phenomena.

cBathy is based on the relationship between wave celerity and depth, expressed by the linear dispersion relation with no currents present,

$$c^2 = \frac{g}{k} \tanh(kh); \quad (4.1)$$

where $c = \Omega/k$ is the wave celerity, Ω is the radial wave frequency ($2\pi/T$), k is the radial wavenumber ($2\pi/\lambda$), h the water depth and g the acceleration due to gravity. From inversion of Equation (4.1), the local water depth can be estimated from a suite of observed wave frequency and wavenumber pairs,

$$h = \frac{1}{k} \tanh^{-1} \left(\frac{\Omega^2}{gk} \right). \quad (4.2)$$

The correct estimation of the $\Omega - k$ pairs is crucial. In real-sea conditions a wave is composed by a superposition of different wave components with many wave frequency and wavenumber pairs. Moreover, the optical contrast is dominated by short and steep waves that do not “feel” the seabed. Additionally, the optical signal can be affected by sun glare, rain drops on the lens, passing clouds and fog. Therefore, a correct inverse estimation of the bathymetry requires a good signal processing. In the cBathy algorithm this is done by frequency-domain empirical orthogonal functions (EOF). The adopted procedure improves previous works, like that of Stockdon and Holman, (2000), which used EOF analysis but for a 1-D cross-shore array, and Dugan et al. (2001) and Piotrowski and Dugan (2002), which considered both horizontal dimensions, but obtaining a limited spatial resolution. In particular the cBathy algorithm is based on Plant et al. (2008), which found the wavenumbers by using the spatial gradients of the Fourier phase in 1-D. cBathy extended the latter procedure for a 2-D cross-shore array.

The cBathy algorithm involves many codes developed in many years and its execution consists of three steps. In the following paragraphs the main aspects of the procedure implemented in cBathy v1.1 are illustrated.

The required input data are: an array of pixel intensity time series (Timestack), an array with the 3D coordinates of the sampling pixels $[x,y,z]$, a vector with the recorded time (epoch), and a setting file containing the input parameters. The variations of intensity inside the optical time series are related to changes in slope of the sea surface and, therefore, they have a strong correlation with the wave signal. Naturally, both the spatial and temporal resolution must be adequately chosen to solve the wave characteristics. The pixel sampling array $[x_p, y_p]$ is a subset of image pixels, defined in real coordinates, where the intensity was extracted. Not all image pixels are used to estimate the bathymetry. Moreover, the bathymetry is resolved only in a user-defined analysis point $[x_m, y_m]$, but using information of the surrounding sampling pixels. The number of sampling pixels, to consider for each analysis point, is defined by specifying the size of the surrounding area (Tile). The tile size is smoothed in the cross-shore direction, by a user-selected factor, to take into account the decrease of the length scales close to the shore. Figure 4-1 shows a classical example of the pixel array.

In the first step of cBathy v1.1 a frequency-dependent analysis is carried out. For each sampling point, a Fourier transform is done to convert the intensity signal from the time domain (I) to the frequency domain (G) (Equation 4.3). The Fourier coefficients are normalized, also to correct the differences in intensity between one camera and another. Then, only the most common wave frequencies are considered. These are user-defined by setting the range of wave periods in the setting file.

$$G(x_p, y_p, \Omega) = FFT \left(I(x_p, y_p, t) \right) \quad (4.3)$$

Then, for each tile, a cross-spectral matrix (\mathcal{C}) is computed to determine the correlations between all possible pixel pairs, averaging over the desired frequency bands:

$$\mathcal{C}_{i,j}(\Omega) = \langle G(x_{pi}, y_{pi}, \Omega)^* G(x_{pj}, y_{pj}, \Omega) \rangle \quad (4.4)$$

where $*$ indicates the complex conjugate and the angled brackets indicate the averaging across each frequency band.

For each frequency band, the total spatial coherence squared is computed and only the frequencies with the highest total coherence are used. The number of examined frequencies (usually 4) is user-selected in the setting file. This allows one to consider only the most important wave components.

For each selected frequency, the cross-spectral matrix contains information of multiple wave trains coming from different directions. Therefore, it is filtered by a spatial EOF analysis and the dominant eigenvector of the cross-spectral matrix is calculated ($v_1(x_p, y_p, \Omega)$). It is the complex eigenvector (first EOF-mode) corresponding to the largest eigenvalue. The phase of the dominant eigenvector (v_1') is the observed spatial wave phase. This observed phase can be described by a model (right-hand side of Equation 4.5) that is function of the wavenumber, wave angle and a phase shift.

$$\underbrace{v_1'(x, y) = \tan^{-1} \left(\frac{\text{imag}(v)}{\text{real}(v)} \right)}_{\text{observed spatial wave phase}} = \underbrace{\exp(i[k\cos(\alpha)x_p + k\sin(\alpha)y_p + \phi])}_{\text{Theoretical spatial wave phase}} \quad (4.5)$$

where k is the wavenumber, α is the wave direction, ϕ is the phase shift (with no geophysical value) and (x_p, y_p) is the sampling point. The dominant wave number and direction are those values that yield the best match between observed and theoretical spatial phase structure. The search is done through a nonlinear least squares fitting procedure, considering also a

weighting function to give more weight to the points nearest to the analysis point and with large eigenvector magnitude. Initial guesses for the value of wavenumber and wave direction (seed angle) are necessary for this nonlinear fit. Using the so estimated wavenumber and corresponding frequency, the local water depth is computed using Equation (4.2). In the end of the first step, a set of frequency-dependent water depths and the relative $\Omega - k$ pairs are obtained for each analysis point.

In the second step, a frequency-independent analysis is performed to combine the frequency-dependent estimates and yield a single value of depth for each analysis point. A simple average of the results obtained from the first step is not accurate due to the nonlinearity of the dispersion equation. At each analysis point, the algorithm considers information from the analysis points within a new tile. All the $\Omega - k$ pairs with an appropriated skill of the previous fit are used in the following analysis. The final estimated depth is the one that yields the best match between the previous estimated and modelled wave number using the nonlinear dispersion relationship as a model. The search is done through a nonlinear least square fitting procedure, using a weighting factor that is function of the skill of the previous fit and of the distance between the points of the tile and the analysis point.

The depths estimated in first and second steps are the heights of the water column. Therefore, to get the bed elevation, the water depth must be tide corrected. Thus, the code subtracts the relative tide level to the estimated value. In this way hourly-estimated bathymetries are obtained.

The hourly-estimated results depend on the current wave climate and weather, thus they can be partially incorrect. In the third step the estimation of a running-averaged depth is carried out to fill gaps in limited time or space. A data-assimilation analysis is carried out using a Kalman filter to smooth and average hourly-estimated depth results.

The Kalman filter analysis is performed in the time domain and the updated average depth (h_{update}) is defined on the basis of the previous running averaged bathymetry (h_{prior}) and new information deriving from current hourly estimates (h_{hour}):

$$h_{update} = h_{prior} + \mathcal{K}(h_{hour} - h_{prior}) \quad (4.6)$$

where \mathcal{K} is the Kalman gain, a parameter (between 0 and 1) that gives the reliability of the new estimation. \mathcal{K} is function of the process error (Q) that represents the depth variability due to waves and currents along two estimated bathymetries. The processor error must be

evaluated at each site. An example of the process error defined for the case of Duck (NC, USA) is reported in Figure 4-1. This third step makes cBathy robust even for long-term analyses.

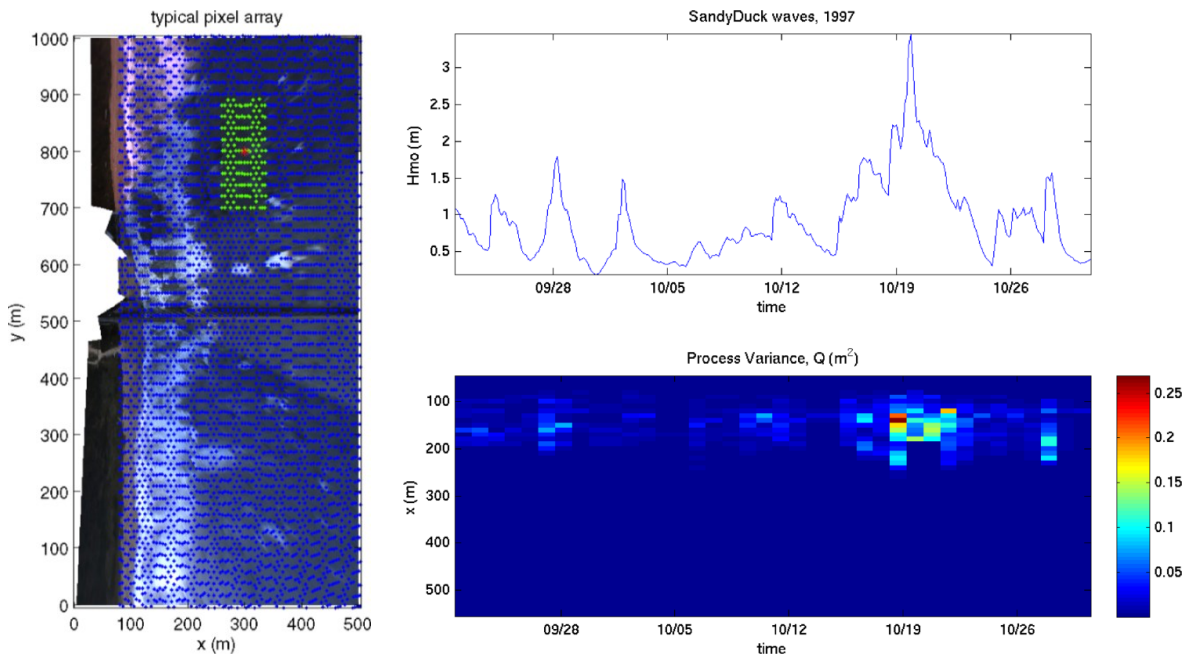


Figure 4-1 The left panel shows an example pixel array used for cBathy analyses: sampling pixels (blue dots, half shown), an example of analysis point (red asterisk) and pixels in the nearby region (green dots). The right panels show an example of offshore wave height (top) and of Process error, Q (bottom), found from bathymetric variability during the Sandy Duck field experiment, 1997. Adapted from Holman et al. (2013).

Other important characteristics of cBathy are the possibility to run in parallel processors and an accurate debugging procedure implemented in the code. The algorithm can be run in two different modes: a “production mode”, where the debug procedure is not performed and a “debug mode”, where diagnostic images are reproduced to investigate the nature of possible errors.

The results of cBathy were first validated with data from Duck (NC, USA) and Agate Beach (OR, USA), for which good performances were obtained. The highest errors occurred in deep water and near the shoreline, where the small-amplitude assumption of the linear theory was no longer valid. Some bias was found also in the breaking zone and for increasing wave heights, but the bar locations and seabed shape were correctly described. Afterwards, the code has been improved and applied to many other sites.

Since February 2018 a new release of cBathy is available on the CIRN repository. It is called cBathy v1.2. The update of the code was driven by the need to fix some errors that sometimes

have been observed in field application of the algorithm. The poor results were in general characterized by very shallow anomalies with small errors. In theory, local poor results are resolved by applying the Kalman filter but, because the error is small, the hourly mistaken results are, however, assimilated into the Kalman results. The problem has been related to short waves that are not correctly resolved from cBathy v1.1. Under particular conditions, the number of points in the tile is not sufficient to represent the actual phases of the waves and the algorithm estimates incorrect wavelength values. Version 1.2 uses a different method to adapt the size of the tile to the wavelength and implements a new approach to determine the seeds of wavenumber and wave direction with the aim to avoid incorrect local minima on the nonlinear fit. In addition, cBathy v1.2 resolves also the problem of inaccuracies in depth estimation at the camera boundary, due to phase shifts along seams. To fix this issue the code follows an approach similar to that explored by Bergsma et al. (2016).

4.2 Application of cBathy to the SGS Data

Use of cBathy on data coming from a new site requires to properly define the input data collection and the setting parameters (cBathy Manual, online on CIRN website). The input array of the intensity time series was extrapolated from videos recorded by the cameras, as illustrated in Section 3.1. The sampling area extended for around 500 m (from -121m to -550 m in the local system) in the longshore direction and for around 900 m (from 70 m to 1000 m in the local system) in the cross-shore direction. The space sampling resolution was 3 m. The data collected and the relative local coordinate of the sampling points were organized to be coherent with the analysis coordinate system and readable from cBathy. The recorded period was 10 minutes long with a temporal sampling resolution of 2Hz. The setting file was modified to give parameters suitable for the study site. The main modified input parameters were the domain setting, the smoothing length scale, the frequency domain, the depth truncation and the max number of points per tile. To implement also the tide correction in the depth estimation, a function that calls the tide elevation of the site was added. Measured tidal data was not available for the specific site; thus, the tidal level recorded in the Ancona harbour (30 km south of Senigallia) was used. It is known that the differences between the tidal level in Ancona and in Senigallia are very small. This was also checked by direct measure of the tide elevation from the SGS Timex images, where the

mean water level of the ten recorded minutes can be clearly seen against the wall of the river channel (Figure 4-2). To perform this estimation a new accurate geometry was calculated and, for one day, the video-derived tide level was also verified with in-situ measurements. The difference between the tidal level in Ancona (from the Ancona buoy, ISPRA) and the tidal level in Senigallia (estimated by images) was around 0.015m, which is smaller than the cBathy bathymetry error. Instead, a new process error (Q) has not yet been defined (see Section 4.1), since the previous main cBathy analysis gave unexpected results and it was not possible to proceed with the Kalman filter processing.



Figure 4-2 Measure of the tide elevation from the SGS Timex images.

During the preliminary analysis only cBatht v1.1 was used. Some setting parameters, such as the range of frequency and domain spacing, have been changed to find the more appropriate values. An example of the parameters used in the preliminary analysis is shown in Table 4-1.

The preliminary application of cBathy to the SGS optical data produced results that varied in quality as a function of the location and wave conditions, but in general, cBathy underestimated the water depth over much of the domain (Figure 4-3a, Figure 4-4).

Table 4-1 – Example of setting parameters used to apply the cBathy algorithm to the Senigallia site.

```

%%%PARAMS
%%% Site-specific Inputs
params.stationStr = 'SGS';
params.dxm = 9; % analysis domain spacing in x
params.dym = 13; % analysis domain spacing in y
params.xyMinMax = [150 600 -550 -121]; % min, max of x, then y
% default to [] for cBathy to choose
params.tideFunction = 'cBathyTide'; % tide level function for evel

%%%%%%%% Power user settings from here down %%%%%%%%%
params.MINDEPTH = 0.25; % for initialization and final QC
params.QTOL = 0.5; % reject skill below this in csm
params.minLam = 10; % min normalized eigenvalue to
proceed
params.Lx = 2*params.dxm; % tomographic domain smoothing
params.Ly = 2*params.dym; %
params.kappa0 = 3; % increase in smoothing at outer xm
params.DECIMATE = 1; % decimate pixels to reduce work
load.
params.maxNPix = 80; % max num pixels per tile (decimate
excess)
params.minValsForBathyEst = 4;

% f-domain etc.
params.fB = [1/10: 1/50: 1/4]; % frequencies for analysis (~40
dof)
params.nKeep = 4; % number of frequencies to keep

% debugging options
params.debug.production = 1; %1) Production mode 0) Debug
mode
params.debug.DO PLOT STACK AND PHASE MAPS = 1; % top level debug of phase
1)do this debug 0)no do this debug
params.debug.DOSHOWPROGRESS = 1; % show progress of tiles
1)do this debug 0)no do this debug
params.debug.DO PLOT PHASE TILE = 1; % observed and EOF results
per pt 1)do this debug 0)no do this debug
params.debug.TRANSECTX = 500; % for plotStacksAndPhaseMaps
params.debug.TRANSECTY = -200; % for plotStacksAndPhaseMaps

% default offshore wave angle. For search seeds.
params.offshoreRadCCWFromx = 0;

```

The comparison was performed with the bathymetric survey carried out in 2013. The survey is not very recent, but the zone is characterized by a general stability of the bottom and by local variation of the features of the bars. The anomalous shallow depths are associated with low estimated errors (95% confidence intervals), therefore the code seems to be very confident in these incorrect results (Figure 4-3b). Several days were analysed, but a bad match between the estimated and the measured sea bottom profiles was obtained every time, even if some small differences were observed when the wave condition changed.

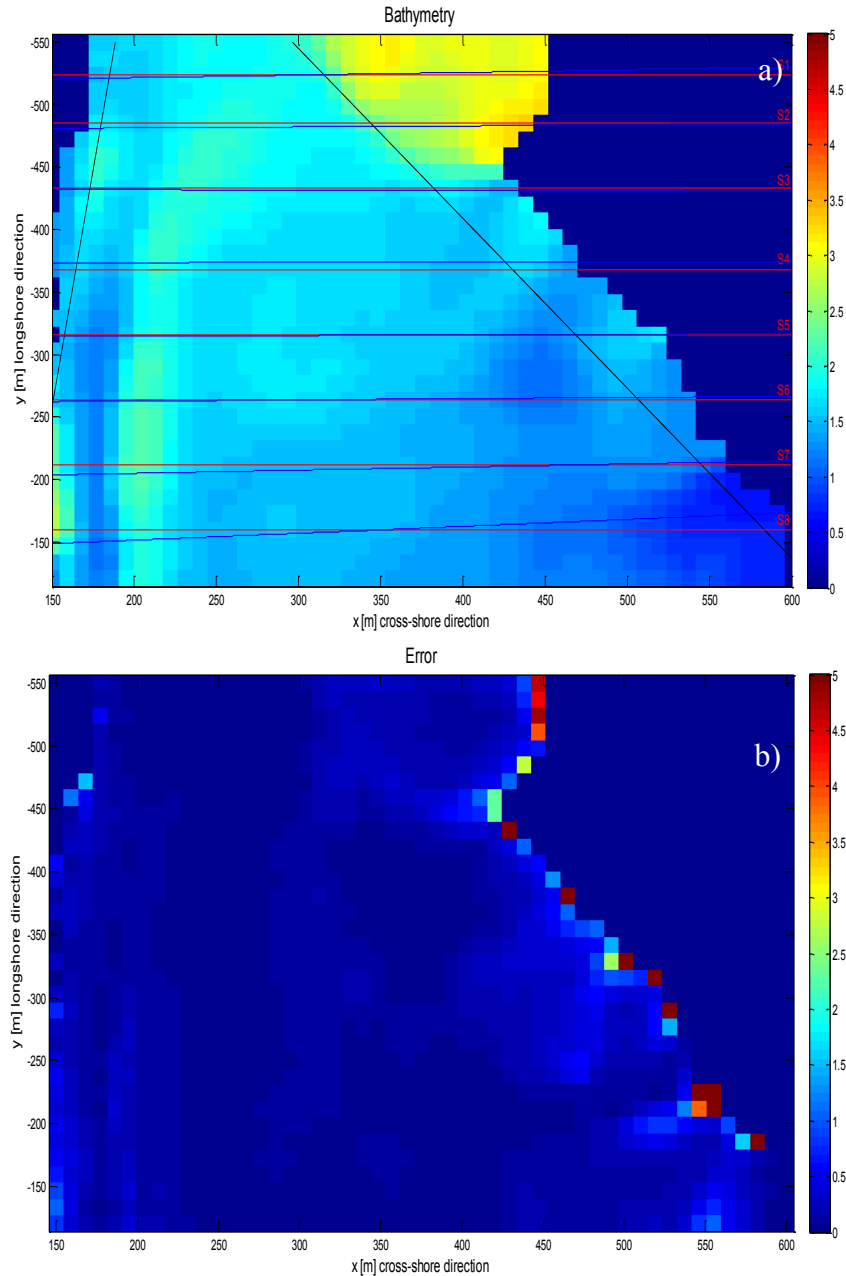


Figure 4-3 – a) cBathy Phase II estimated bathymetry. The blue lines are the sections of survey profiles (2013), the red lines are the sections of the cBathy grid, and the black lines are the camera boundaries. b) Error Map (95% confidence intervals) from cBathy Phase II. Depth colormaps have blue for shallow and red for deep. The harbour is located in the upper part of the domain ($y \sim -700\text{m}$), while the Rotonda is located in the lower part ($y=0\text{m}$).

The cBathy estimates give the systematic presence of an unlikely flat area toward the offshore. Instead, the code seems to well identify the first submerged bar around $x=200\text{m}$. Moreover, the results of the first sections (closer to the SGS station) are quite accurate, but the quality of the estimation decreases when moving far from the station.

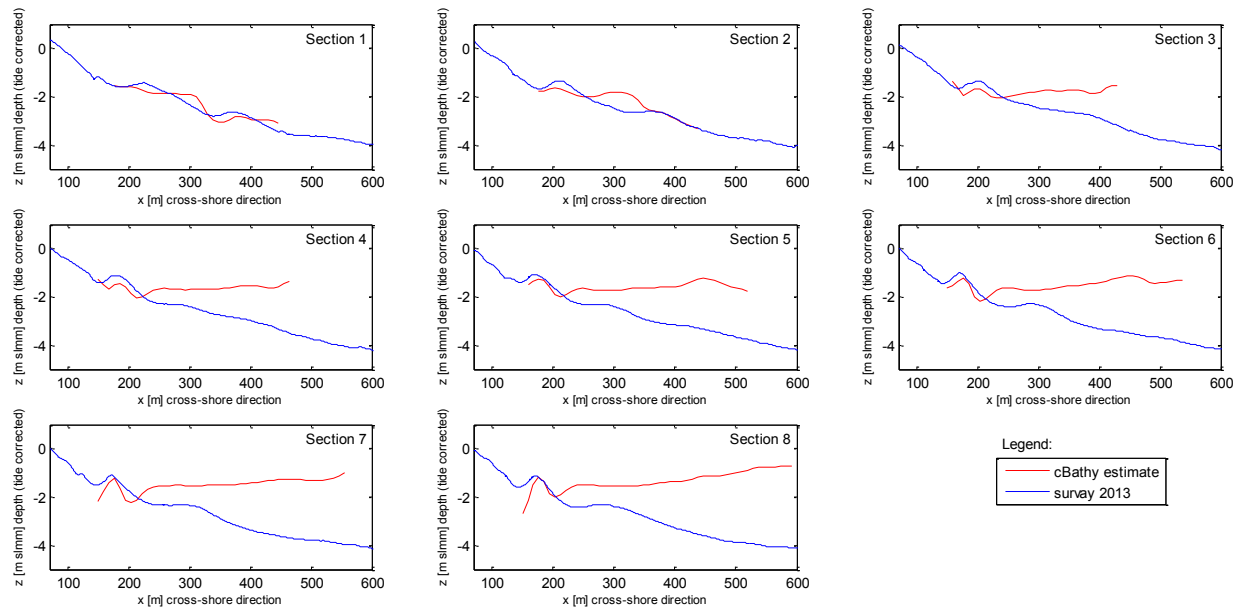


Figure 4-4 – Comparison of estimated and measured bathymetry. The blue lines are the survey bed (2013) and the red lines are the cBathy estimated bed. The profiles are related to the transects shown in Figure 4-3.

The reasons why cBathy underestimates the depth when it is applied to the SGS data is not well understood as yet. Several different analyses were performed to better approach and fix the problem. In the following Sections, an accurate debugging analysis is reported and the main explored issues discussed.

4.3 Debugging analysis

4.3.1 cBathy debug mode

cBathy contains a suite of good debugging tools that help the user to investigate the nature of unexpected poor results (cBathy Manual, online on CIRN website). By running the code in the debug mode it is possible to visualize some important diagnostic figures, such as two selected (cross-shore and alongshore) transects, phase maps for the entire collection domain for all possible frequencies and phase maps of the dominant EOF within a tile for a particular frequency. In this section the classical approach of cBathy debug is followed, even if other investigations have been performed at the same time.

The underestimate in depth was present in almost all the analyzed data, but for the debug analysis only the registration collected on 30 December 2016 at 13:00 has been used. For the considered hour, the results, in production mode have been already illustrated in Figure 4-3 and Figure 4-4.

Timestack inspection

The first aspect to check when poor results are obtained is the presence of the wave signal in the input optical Timestack. Inspection of a representative cross-shore transect ($y=-316\text{m}$) selected in the central part of the domain (Figure 4-5), reveals that the shoreward wave propagation (oblique trajectories of waves) is clearly visible over a large part of the cross-shore extent (at least until $x=400\text{m}$).

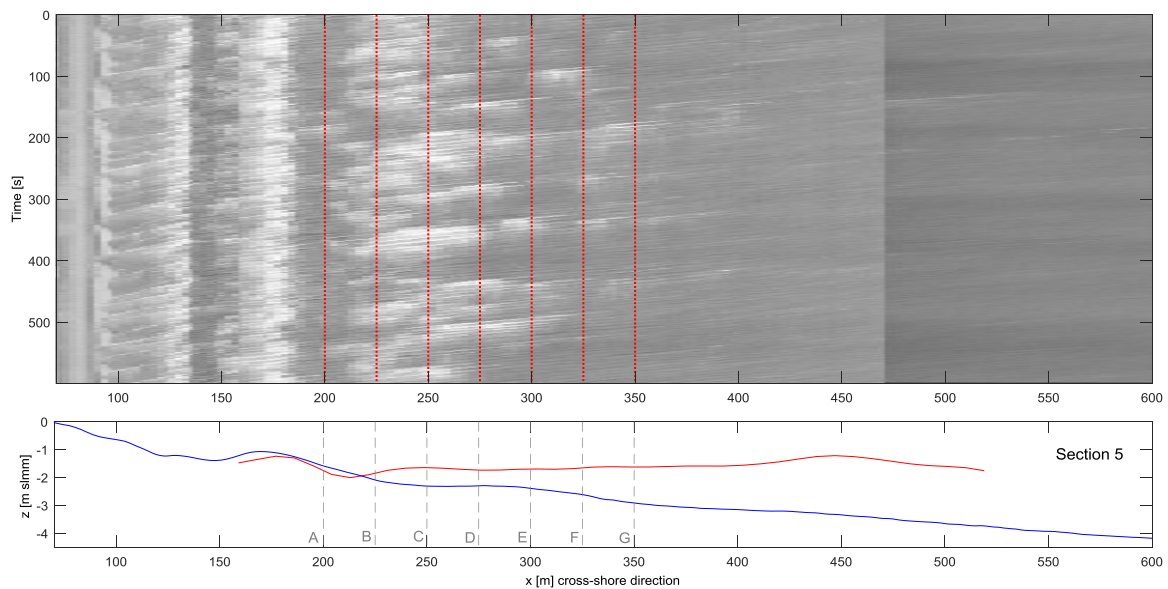


Figure 4-5 - Time series and profile at $y=316\text{m}$. The upper panel gives the Timestack, where the red dotted lines are the x -positions of the debug points. In the lower panel the blue line is the survey seabed (2013), the red line is the cBathy estimated bed and the grey lines are the x -positions of the debug points.

However, for the analysed site, the wave signal is, in general, not visible outside the surf zone. Then, we can identify the first submerged bar, we can see the swash motion and that there are not floating objects, like boats. The same characteristics may be observed in the movie of the Timestack. Moreover, the wave propagation is sometimes not characterized by dark trajectories, which are representative of wave fronts, but by white trajectories, which are representative of wave breaking, since they are mainly in the surf zone. In this region the linear dispersion relationship is probably not adequate, so the problem could be related

to nonlinear wave effects. Many authors analyzed the influence of nonlinearity on the dispersion equation and many models have been developed to take into account nonlinear properties (Grilli, 1998; Catálan and Haller, 2008; Yoo et al., 2011). Nevertheless, these models are not commonly used in coastal monitoring due to their complexity and time consumption (Rutten et al., 2017). In this thesis nonlinear effects are not analyzed in depth. If waves are present, both the wavelength and the period can be read from the Timestack. Observing a specific cross-shore location, the distance between two consecutive trajectories represents the period, while, observing a specific time, the distance between two consecutive trajectories represents the wavelength in the cross-shore direction. This analysis is very approximate, but gives an overall description of the wave characteristics that are contained in the optical image. For the analyzed Timestack the wavelengths and periods are coherent with the cBathy estimates (period around 5.5s, and wavelength around 20m).

Phase maps inspection

The first important diagnostic image automatically produced from the CBathy debug mode is the “phase maps for the entire collection domain and for user-selected frequencies” (Figure 4-6). Also in these images the progressive waves must be visible. This means that the full color range (corresponding to $-\pi$ to π) must be present and the color transition must be progressive and with spatial patterns comparable with sea waves.

Phase maps of the test hour (Figure 4-6) show clear wave patterns over the whole domain, in particular for frequencies equal to 0.16Hz-0.18Hz-0.20Hz. The spatial lengths are of about 20m, in agreement with the Timestack measures and with the cBathy estimate. Similar values have been derived also from the ortho-rectified snapshot (Figure 4-7). Instead, the wave angle is somehow variable.

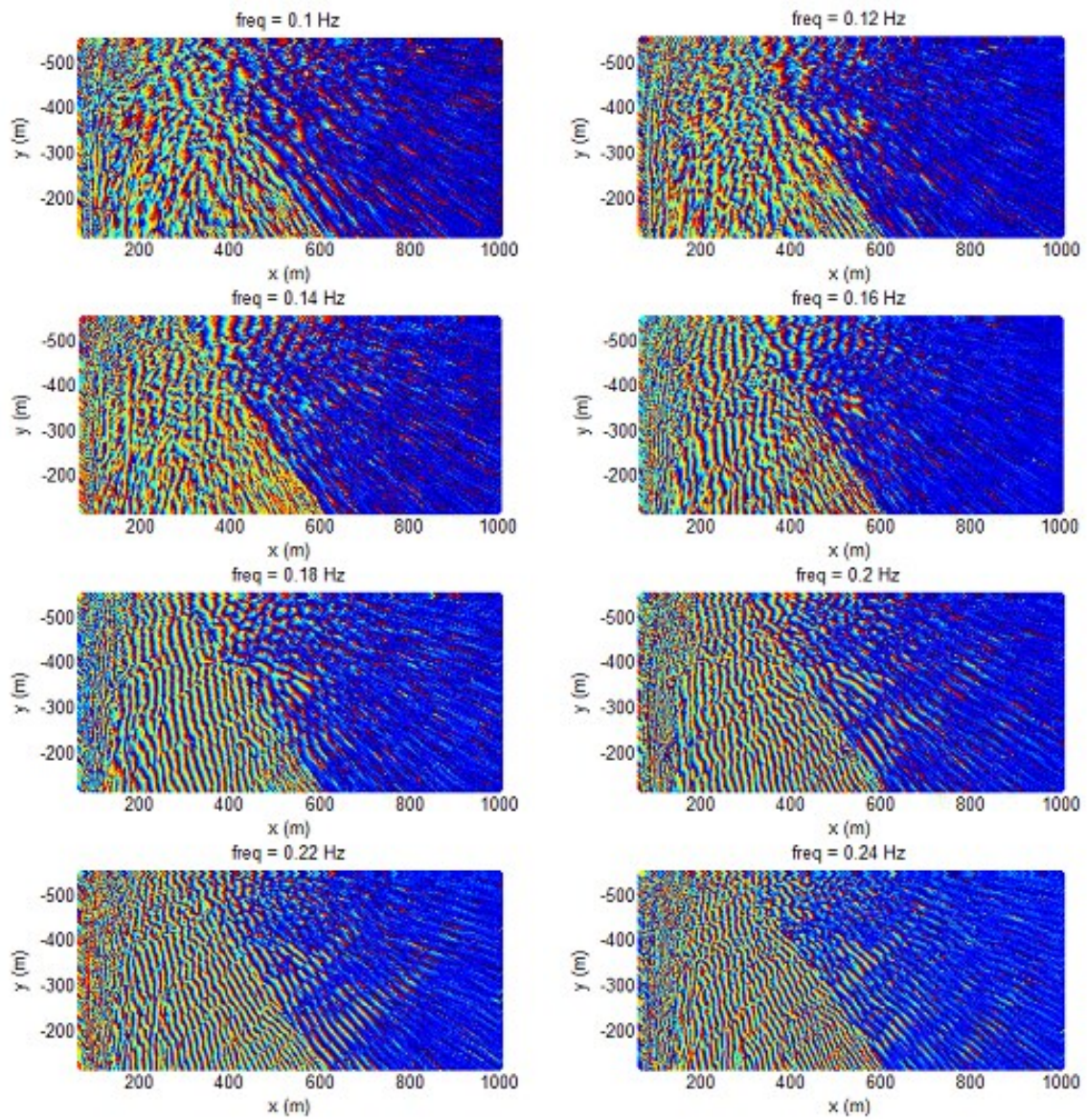


Figure 4-6 - Phase maps for the range of frequencies selected in the setting file.

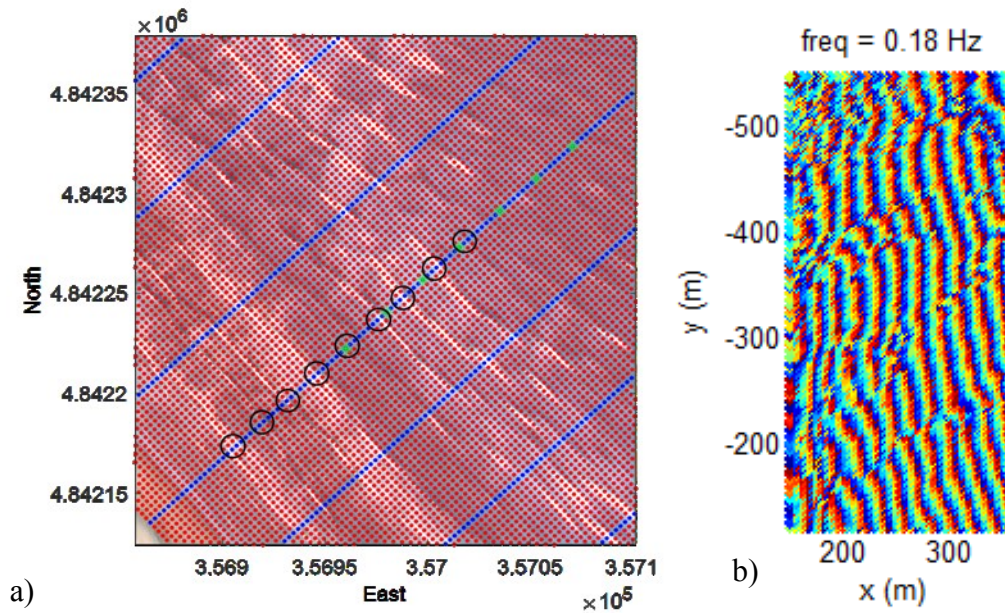


Figure 4-7 - a) Zoom of the ortho-rectified snapshot. The red dots are the points of the sampling grid (spaced 3m), the blue dots are the points of the sections, the green dots are the debug points and the black circles identify the wave crests. b) Zoom of the phase map for the frequency 0.18Hz.

Nonlinear fit

Other very important diagnostic figures are the “phase and magnitude maps for the tiles” and for the most important frequencies (4 in the analysed test). These images are provided for each analysis point, in the debug mode. To simplify the analysis only a small subset of the analysis points has been investigated. With focus on the representative transect discussed above, seven points have been selected for the debugging (x equal to 200m, 225m, 250m, 275m, 300m, 325m, 350m). Figure 4-5 shows the locations of the debug points both in the Timestack and in the profile. Figure 4-8 and Table 4-2 show the results of the debug analysis for a specific tile. For each tile and for each frequency, the left two subplots, in Figure 4-8, show the observed and modelled phase of the dominant eigenvector, while the right two subplots display the observed and modelled magnitude of the same dominant eigenvector. In the phase maps, around one or two wavelengths, a correct fitting should appear. Sampling many wavelengths is unnecessary. Then, the observed surface should match the modelled surface. In the table of the numerical results (Table 4-2), the skill values show the quality of the fit, while the lam1 values (normalized eigenvalues) should be large to indicate high levels of energy in the first EOF. For the selected debug points sometimes the waves are not evident in the maps, but the nonlinear fit performs well. Moreover, the skills are, in general,

high, this indicating a good match. Even if the error on the depth estimation seems to increase when moving offshore, the debug does not highlight any characteristic issue.

To compute the nonlinear fit, cBathy decimates the sampling points in the tile down to the maximum allowed number of points per tile fixed by the user (usually 80). If the waves are small, the pixel array in the analysed tile may be too sparse to identify the wave patterns (problem highlighted and fixed in cBathy v1.2). In the specific case, in the full phase maps (Figure 4-6) the wave patterns are visible and the total number of points in the full array is higher than the imposed limit of 80 (sampling points in each tile: A=368, B=368, c=425 D=425, E=450, F=513 G=513). Therefore, a new analysis, has been performed using a “maximum number of points per tile” equal to 500. For this new analysis the waves in the phase maps are very clear and the fit really good, but the estimated frequency, wavenumber and depth are similar to the previous results (Figure 4-9, Table 4-3). Therefore, the underestimation of the bathymetry seems not correlated with an incorrect nonlinear fitting. A comparison between the bathymetric results obtained using the old (80) and the new (500) maximum number of points per tile is shown in Figure 4-10.

A sea wave can be decomposed into an infinite number of components. Therefore, deeper analyses have been executed by changing the user-defined “range of possible frequencies” and the related resolution. The number of dominant frequencies to analyse in the single tile has been increased as well; however no useful information has come from these studies.

Debug in the alongshore direction

It is important to observe that the goodness of the estimated bathymetry decreases also by moving far from the camera location. Thus, the cBathy debug has been performed also observing the phase maps of the dominant EOF in the alongshore direction. Similarly to the previous cross-shore analysis, an alongshore section has been chosen and the phase maps of a number of debug points observed. Like for the cross-shore tiles, the nonlinear fitting is correctly performed for the all points but incorrect depths have been nevertheless estimated. No additional information, useful to understand the problem has been highlighted from this analysis.

Inaccuracies on the camera boundary

Significant bathymetry underestimations have also been observed in other sites (Duck in USA, Egmond and Zee and the ZandMotor in the Netherlands, Porthtowan in England). In

those cases the errors were related to inaccuracies on the camera boundary. A non-perfect synchronization may exist between two adjacent cameras when multiple cameras are used, therefore inappropriate phase maps may be achieved on the camera seams. Moreover, small errors in the individual camera geometries could lead to important differences in depth estimations. Following Bergsma et al. (2016) an analysis has been performed by considering separated cameras. First, an individual Timestack for each individual camera has been built and individual cBathy runs have been executed for each camera without modifying the original algorithm. Secondly, the method used to analyse tiles containing multiple (double) cameras has been slightly changed. Two different operative methodologies have been used to this scope. In the first procedure, the code estimated the bathymetry twice for the entire domain, considering, in the overlapping area, the first time one camera, the second time the other camera (similar to Bergsma et al., 2016). In this way two different depths and relative errors have been estimated. The two depths have been finally averaged, using the error as a weighting. In the second procedure, the code has executed the tile analysis twice in those tiles containing multiple cameras by considering the first time one camera, the second time the other camera. With this approach, at the end of the first cBathy step, for some analysis points two sets of results have been obtained. Then, all the results have been used to estimate the depth in the second step of cBathy. All of these procedures did not improve significantly the bathymetry results (plots are not reported because the small differences are not visible). This demonstrates that the underestimation of depths observed by applying cBathy to SGS data is not correlated to problems in the camera boundaries.

Table 4-2. Numerical results for the debug point D ($x=275\text{m}$, $y=-316\text{m}$). The depths are not tide corrected yet. $\text{maxNpix}=80$ points.

fB : [0.1600 0.1800 0.2400 0.2000]
 k : [0.2902 0.3101 0.4290 0.3879]
 a : [-0.0554 0.1592 0.2455 0.0075]
 dof : [14.9332 17.1916 13.9243 14.3968]
 skill : [0.9313 0.9035 0.8889 0.6175]
 lam1 : [38.7736 36.6898 26.5967 22.9769]
 $k\text{Err}$: [0.0479 0.0441 0.0350 0.0603]
 $a\text{Err}$: [0.1363 0.1103 0.0692 0.1146]
 $h\text{Temp}$: [1.2787 1.4445 1.4090 1.1377]
 $h\text{TempErr}$: [0.4163 0.4159 0.2458 0.3520]

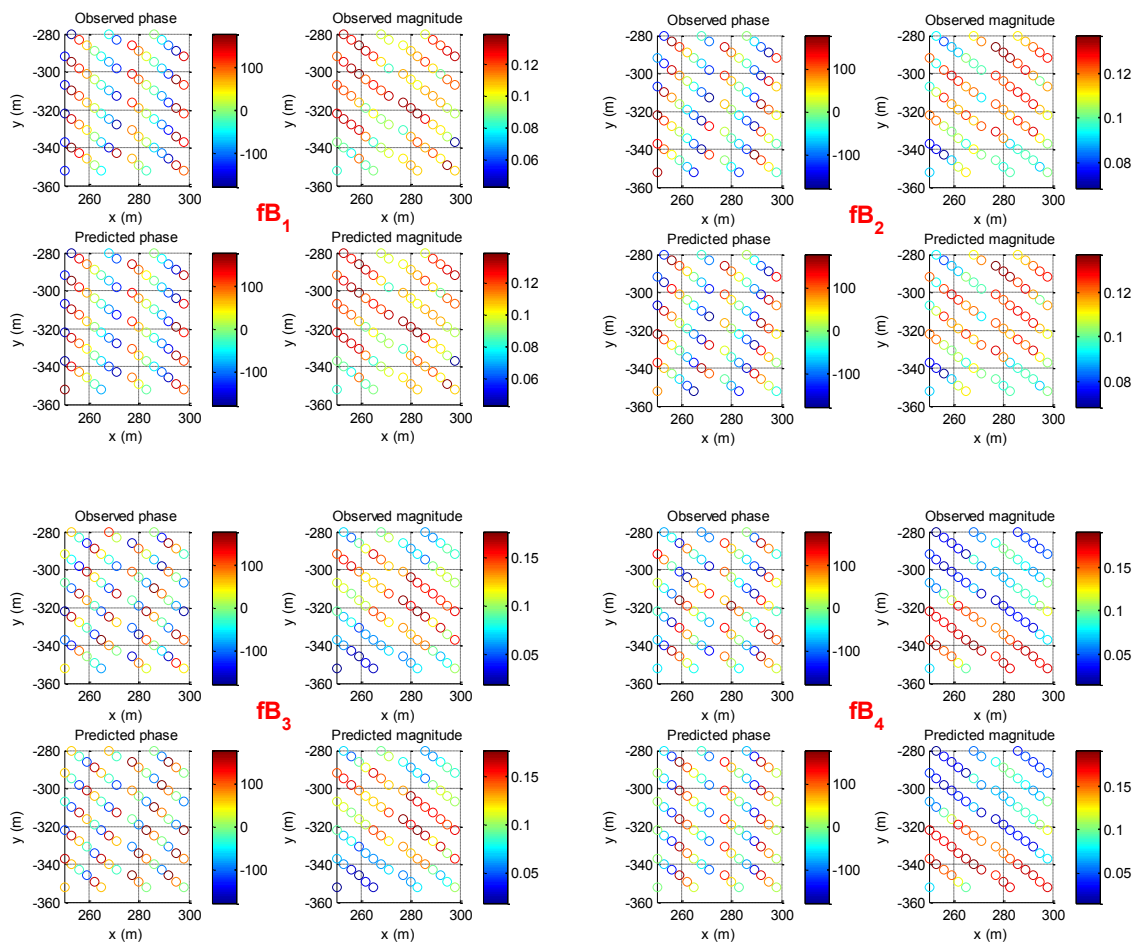


Figure 4-8 Comparison between observed and predicted phase and magnitude maps for the tile relative to the analysis point D ($x=275\text{m}$, $y=-316\text{m}$). The maps are ordered from the most coherent frequency ($fB1$) to the less coherent frequency ($fB4$). $\text{maxNpix}=80$ points.

Table 4-3 Numerical results for the debug point D ($x=275\text{m}$, $y=-316\text{m}$). The depths are not tide corrected.
 maxNpix=500 points.

fB: [0.1600 0.1800 0.2400 0.2000]
 k: [0.2875 0.3101 0.4290 0.3862]
 a: [-0.0601 -0.1564 -0.2445 -0.0011]
 dof: [85.7591 89.0097 77.6508 77.0300]
 skill: [0.9194 0.9258 0.8969 0.6647]
 lam1: [207.2152 197.9405 141.1917 121.5801]
 kErr: [0.0202 0.0187 0.0144 0.0256]
 aErr: [0.0502 0.0439 0.0278 0.0433]
 hTemp: [1.3038 1.4443 1.4090 1.1481]
 hTempErr: [0.1809 0.1759 0.1013 0.1519]

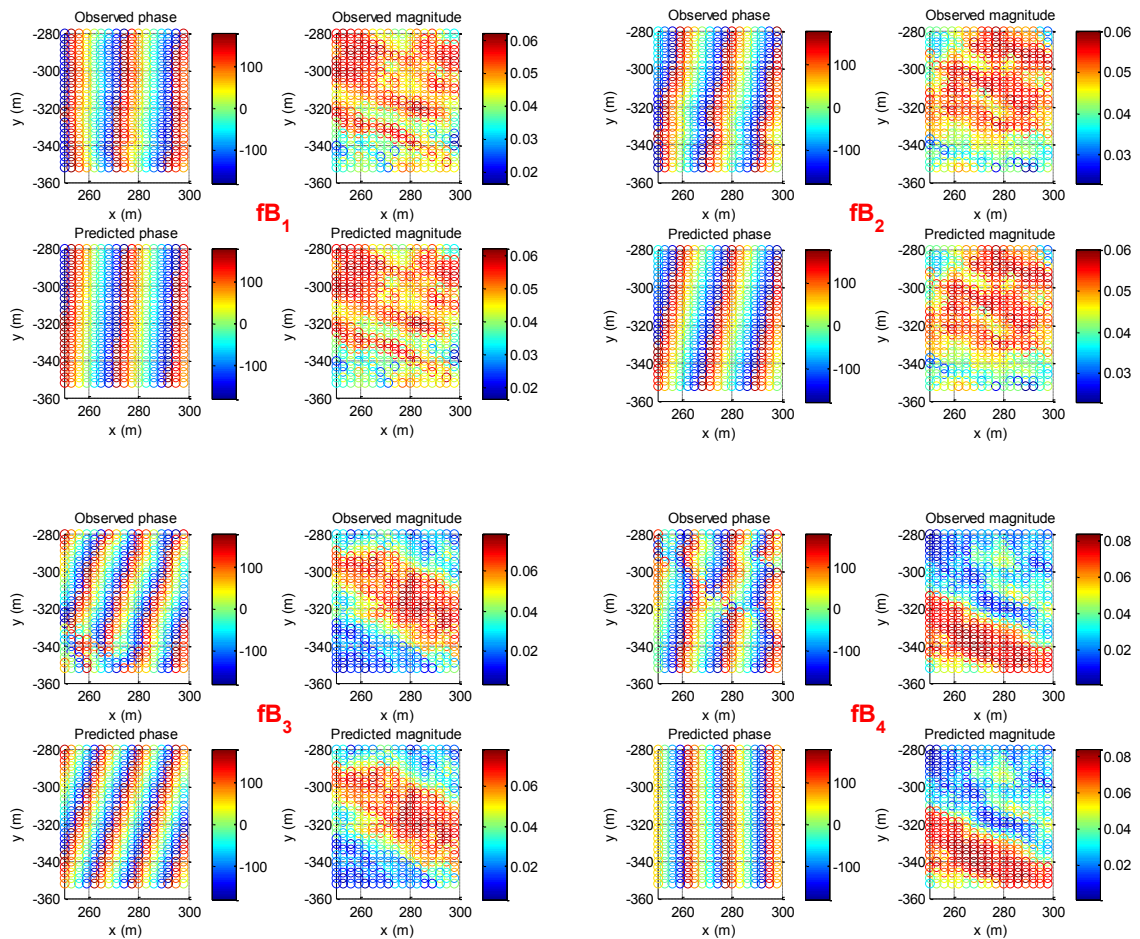


Figure 4-9 Comparison between observed and predicted phase and magnitude maps for the tile related to the analysis point ($x=275\text{m}$, $y=-316\text{m}$). The maps are ordered from the most coherent frequency (fB1) to the less coherent frequency (fB4). maxNpix=500 points.

Short waves and wave direction

A new updated version of cBathy (Section 4.1), called cBathy v1.2, was recently developed, in which important changes were implemented. The new code uses a frequency–dependent tile whose size adapts to the expected wavelength. Because of this, the new code can provide reliable results for both short and long waves. Moreover, the new version implements a new method to find the seed angles and a procedure to fix the inaccuracy on the boundaries of multiple cameras. cBathy v1.2 has been used to estimate the bathymetry using the SGS data. By using the new code the estimated area increased (less NaN in the domain) but the underestimated zone of flat bathymetry persisted (Figure 4-10).

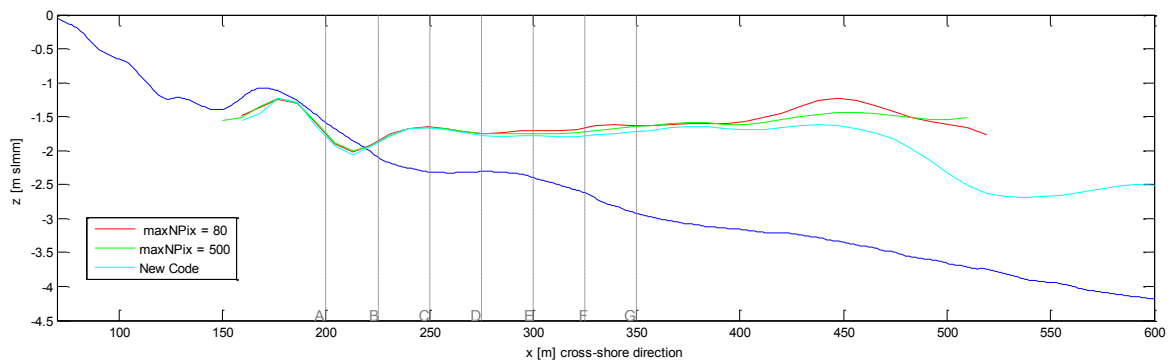


Figure 4-10 Profile at $y=316\text{m}$. The blue line is the survey bed (2013), the red line is the cBathy estimated bed with $\text{maxNPix}=80$, the green line is the cBathy estimated bed with $\text{maxNPix}=500$, the cyan line is the estimated bed using cBathy v1.2 and the grey lines are the x -positions of the points used for the debugging.

Manual computation of physical quantities

Overall, the above-mentioned analyses show that cBathy seems to correctly estimate the wave period over the whole domain, even if the quality of the depth estimate varies in space. Since the estimate of the bathymetry is function of the period and of the wavelength, an incorrect wavelength estimate was suspected. No error in the nonlinear fitting has been observed, even for those points giving an incorrect water depth estimate.

Table 4-4 summarizes a comparison between the cBathy speed and estimated celerity. The cBathy speed has been calculated by the linear theory, through the relation:

$$c = \frac{2\pi\Omega}{k} \quad (4.7)$$

where the frequencies (Ω) and the wavenumbers (k) have been taken from the first cBathy step, this giving four values for each variable. The estimated speed has been calculated in two different ways. First, it was calculated as the slope of the trajectory in the Timestack, around a selected point. Secondly, it has been computed by the linear theory in shallow water:

$$c = \sqrt{gh} \quad (4.8)$$

where h is the depth derived from the survey (2013) and g gravity acceleration. Probably the speed estimated from the Timestack is less accurate than the others because it is difficult to define a suitable neighbourhood where to calculate the slope and because it is an instantaneous calculation (it does not consider the whole time series). The same analysis has been computed for each point of the debug analysis. In general, the celerity is underestimated, which suggests an underestimation of the wavelength, which, in turn, gives a final underestimation of the depth.

Table 4-4 - Celerity analysis, point D.

| | | | | | |
|------------------------------------|--|---|--|--|---|
| speed estimated by timestack | <p><u>point of analysis</u></p> <p>y= -316 m x= 274 m t= 262 s</p> | <p><u>point of right</u></p> <p>y= -316 m x= 283 m t= 260 s</p> | <p><u>point of left</u></p> <p>y= -316 m x= 265 m t= 265 s</p> | | |
| | <p>$\Delta x = 18$ m $\Delta t = 4.9$ s $c = \Delta x / \Delta t = 3.7$ m/s</p> | | | | |
| speed estimated by survey | <p><u>point of analysis</u></p> <p>y= -316 m x= 275 m</p> | <p>g= 9.81 m/s² h= 2.31 m</p> | <p>$c = (gh)^{1/2} = 4.8$ m/s</p> | | |
| speed calculated by cBathy results | <p><u>point of analysis</u></p> <p>y= -316 m x= 275 m h= 1.7291 m</p> | <p>hTemp [m]</p> <p>1.6687 1.8345 1.7990 1.5277</p> | <p>fB [1/s]</p> <p>0.1600 0.1800 0.2400 0.2000</p> | <p>k [1/m]</p> <p>0.2902 0.3101 0.4290 0.3879</p> | <p>c=2*π*fB/k [m/s]</p> <p>3.4642 3.6471 3.5151 3.2396 <i>mean.</i> 3.4665</p> |

A likely inaccuracy in the wavelength estimation can be also deduced by plotting frequency and wavenumber maps over the whole domain (Figure 4-11).

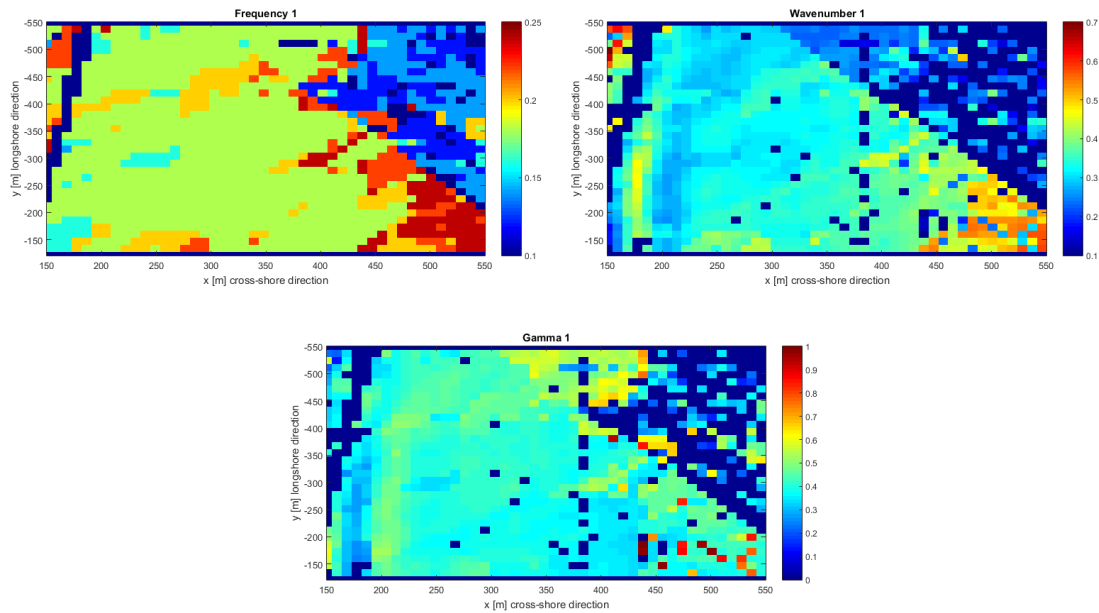


Figure 4-11 Plots of: first dominant frequency of each point (top left panel), relative wavenumber (top right panel) and gamma (bottom panel).

Frequencies were correctly estimated around 0.18Hz in quite the whole domain. The accuracy of this value has already been verified earlier by looking also at the video. The relative wavelengths show a fairly constant value (around 0.3 1/m) over the whole domain, instead of increasing toward the shore, as expected from the linear theory (assuming constant periods). Figure 4-12 shows the results of a manual computation of the wavelengths. Moreover, the Gamma coefficient (γ) plotted in Figure 4-11 shows that the wave “feels” the seabed, because running in shallow/intermediate waters. Gamma (Equation 4.9) is the ratio of deep water wavenumber (k_{deep}) to local wavenumbers (k):

$$\gamma = \frac{k_{deep}}{k}; \quad k_{deep} = \frac{4\pi^2 \cdot \Omega^2}{g} \quad (4.9)$$

Gamma equal to one indicates deep water.

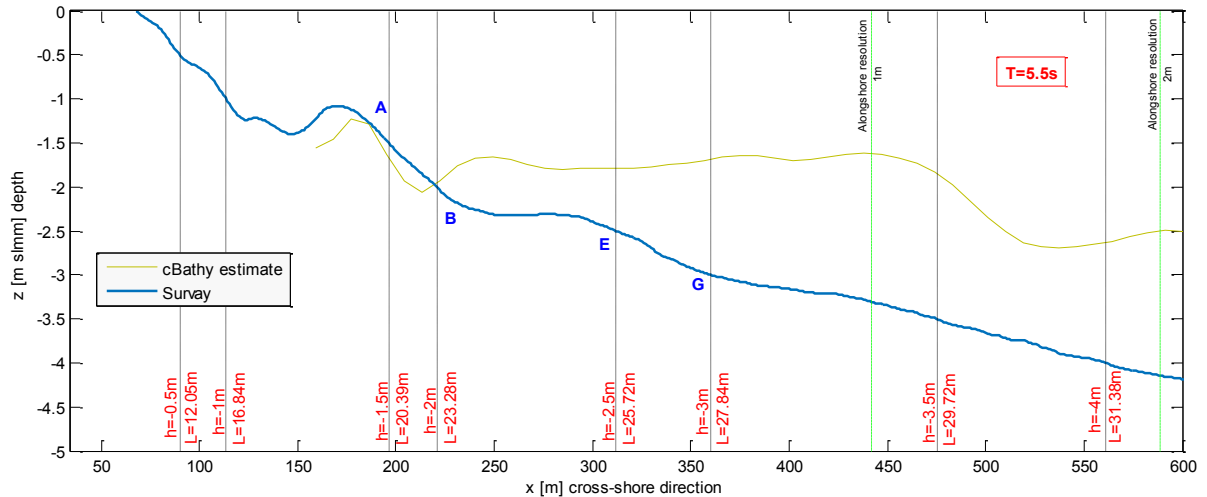


Figure 4-12 - In red the calculated values of wavelength for a period of 5.5s and the corresponding depth. The dotted black lines show the approximated position of these depths along the survey profile. The blue letters show the approximated position of some points of the debug analysis. The blue line is the survey profile (2013) while the brown line is the cBathy estimated profile. The green lines are the contours of the camera resolution.

4.3.2 Further Analyses

In Section 4.3.1 an accurate debug analysis of cBathy has been presented and discussed, to conclude that the underestimation of the Senigallia bathymetry is probably correlated to an underestimation of the wavelengths, but the nature of such error has not yet been found. Therefore, other aspects have been investigated to better understand the problem.

First, gross errors have been excluded by applying the Demo version of cBathy available on the CIRN website. Second, the accuracy of the camera geometries has been checked by comparing the image-derived locations of some objects with their known actual locations. Since the results varied in quality as a function of the location, the camera resolution and possible geometric effects have been analysed. Finally, the relevance of the direction of the incident wave angles has been investigated.

Camera resolution

Figures from Figure 4-13 to Figure 4-16 give the resolution along a domain sampled in local coordinates, for the cameras installed at the SGS station. The sampling grid used in the cBathy analysis has a 3 m resolution. Therefore, the camera resolution is lower than the grid

resolution for a wide area of the domain. Additionally, the resolution is suitable for the wavelength estimation.

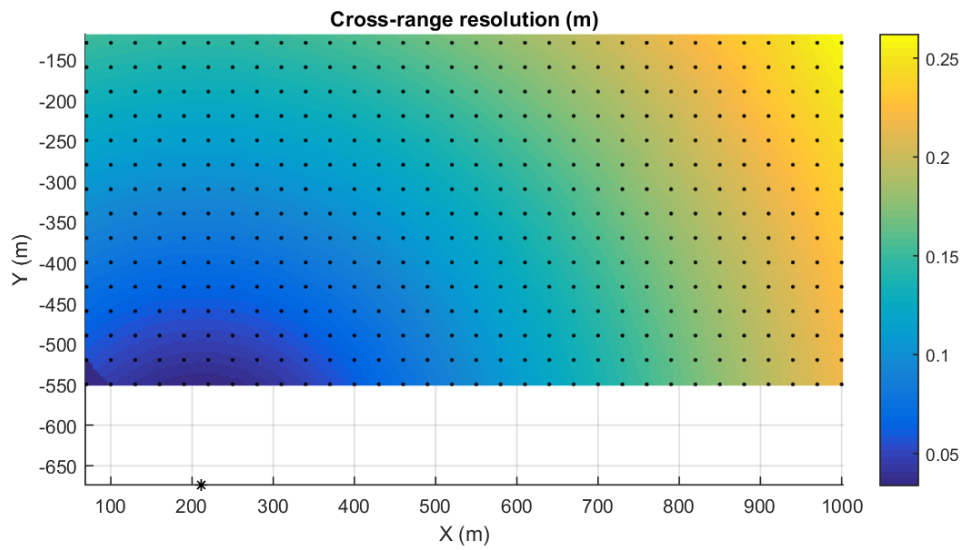


Figure 4-13 Resolution along the cross-axis of the cameras (normal to main axis of the camera). The black asterisk is the camera location. The black line is the 3 m contour. The y-axis is inverted.

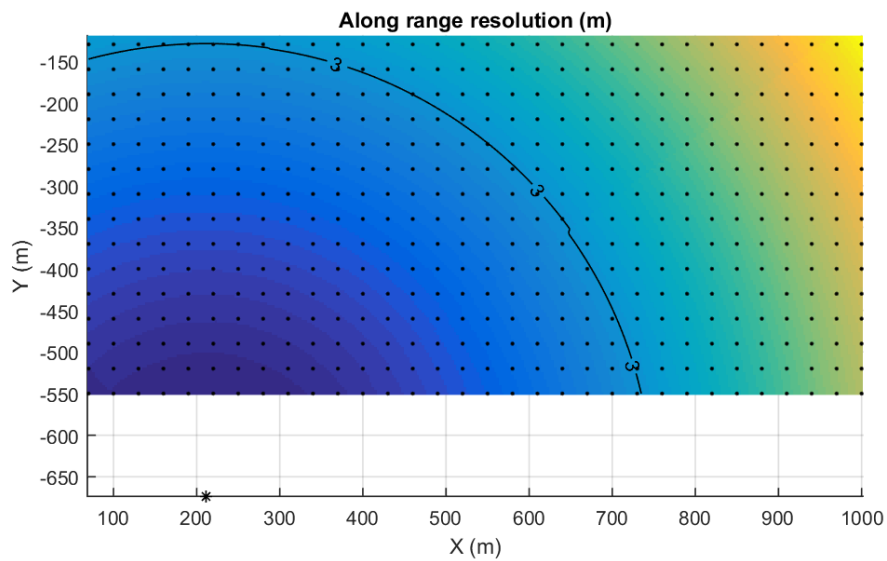


Figure 4-14 Resolution along the main axis of the cameras. The black asterisk is the camera location. The black line is the 3 m contour. The y-axis is inverted.

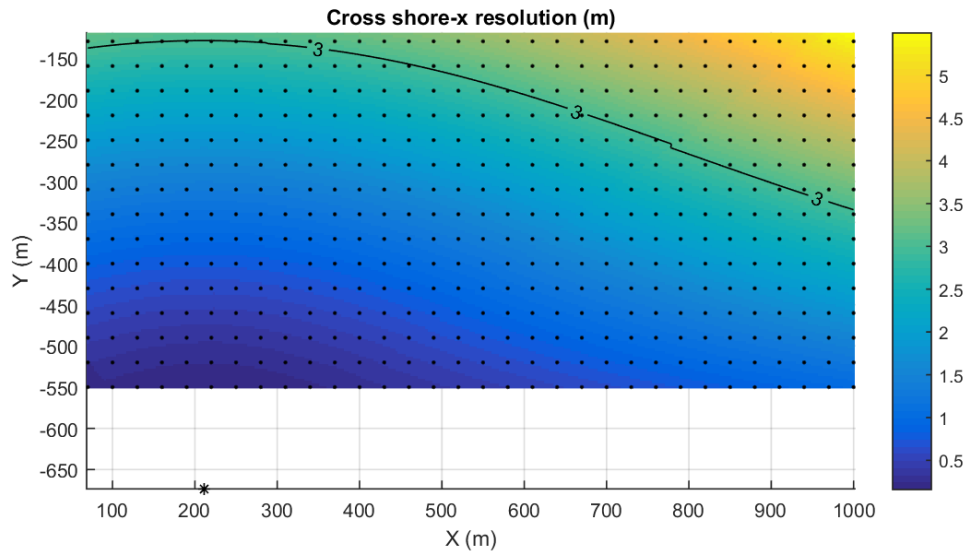


Figure 4-15 Resolution in cross-shore direction. The black asterisk is the camera location. The black line is the 3 m contour. The y-axis is inverted.

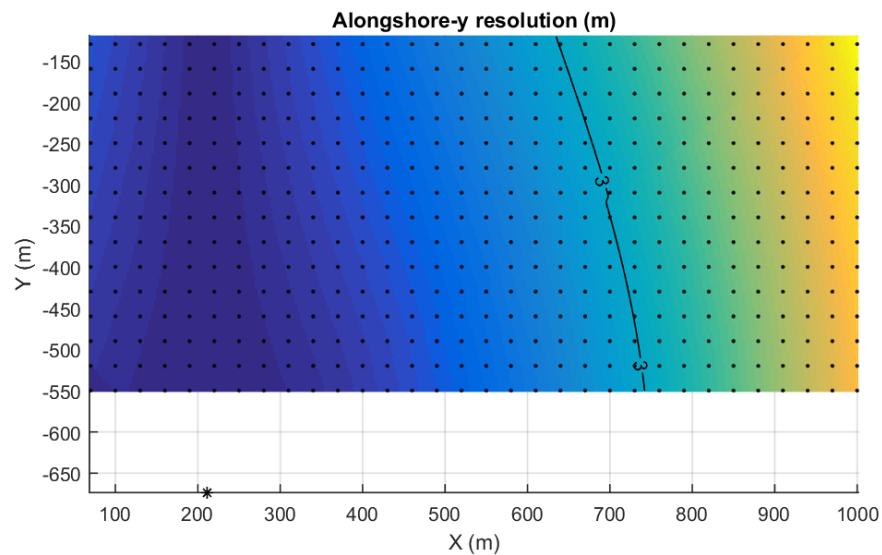


Figure 4-16 Resolution in alongshore direction. The black asterisk is the camera location. The black line is the 3 m contour. The y-axis is inverted.

Geometric effects

This does not exclude the possibility of a pixel shifting both in the cross-shore and alongshore direction. For example, in macro-tidal environments, a set of pixels can move towards or further from the camera and thus change its spatial footprint. For instance, an increase in water level underestimates the wavelengths and thus the depths. This influences the measurements of physical properties in optical images (Holman and Stanley, 2007) and

also the bathymetry estimation (Bergsma et al., 2016). A procedure to overcome this effect has been proposed by Bergsma et al. (2016). Even if the Senigallia beach is a micro-tidal environment, a test to check the tide effects has been performed. In particular, the intensity time series have been usually extracted from specific points in real plane coordinates by imposing a z -coordinate that is always equal to zero. Then, these coordinate have been transformed in image coordinates and used to extract the time series. To analyse tide effects the z -coordinate has been imposed equal to the current tide level. New Timestacks have been built and used as input for cBathy. The bathymetry results obtained using tide-corrected Timestacks are very similar to the previous ones, therefore the tide does not affect the depth estimations.

Always to avoid errors on the Timestack, a video stabilization has been implemented on the code that reads the video and builds the time series (the procedure is illustrated in Section 3.2). The stabilized Timestacks have been used to estimate the bathymetry, but it has been observed that the shift of the images points due to a camera movement does not sensibly modify the depth estimations.

Finally, also the shift due to lens distortion has been analysed. The image coordinates of the sampling pixels have been converted from undistorted to distorted coordinate by applying the radial and tangential distortion coefficients. New Timestacks have been built and used in the bathymetry analysis. Also, in this case the results confirmed that possible shifts in the pixel locations do not affect the quality of the depth estimation.

Wave viewing angle

A general important aspect for the depth inversion techniques using optical data is the camera orientation with respect to the direction of wave propagation since the waves are generally not visible in the optical image when the camera looks along the crest (Stilwell, 1969; Chickadel, 2007).

Given the particular location of the SGS station (Figure 3-1), the cameras used for cBathy application look the study beach predominantly in the longshore direction. Unlike typical cBathy applications that commonly use data from shore-based stations, the application of cBathy using SGS data could be more affected by errors related to wave viewing direction. The relevance of this aspect has been investigated more in depth in Section 4.4, using computer-generated data.

4.4 Synthetic Tests

An important aspect for the results of the depth inversion is the relationship between the camera viewing angle and the direction of wave propagation. Optical applications of remotely-sensed depth inversion methods like cBathy require video images of waves. The contrast between wave crests and troughs produces the time dependent signal in optical imaging of surface gravity waves. The highest optical contrast occurs when the camera looks in the direction of wave propagation while the waves are generally not visible when the camera looks along the crest (Chickadel, 2007). The quality of the optical signal depends on the viewing angle (Holman et al., 2017), hence the quality of the depth inversion also depends on the viewing angle. Additionally, cBathy v1.1 requires an initial guess at the direction of wave propagation to seed the nonlinear fit used to obtain directions and wavenumbers. Therefore, the choice of the seed angle also impacts the final estimate of water depth.

The SGS station is not located on the beach but on the middle of the harbor jetty, so the waves are mainly looked by the cameras parallel to the crest rather than perpendicular, as it happens for the usual shore-based video monitoring stations. The diagram in Figure 4-17 shows the differences in location. The error in depth estimation, obtained by using cBathy to the Senigallia Beach data, could be related to the way the cameras look at the waves. To better investigate this aspect we performed some dedicated Synthetic Tests.

Synthetic tests have been used for a sensitivity analysis, to avoid the complexities of real imagery such as breaking waves, irregular bathymetry, currents, non-uniform lighting conditions and, sometimes, reflection or diffraction of waves and interaction with engineered structures, such as harbors and jetties. Synthetic tests simplify the problem and focus the analysis on the role of light reflection off the water surface and wave viewing angle on error in estimated water depth as well as frequency and wavenumber.

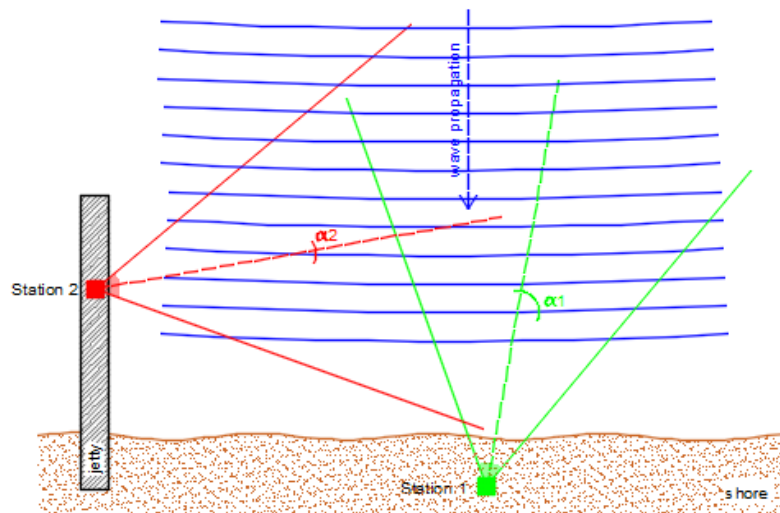


Figure 4-17 - Scheme of the way of the cameras look at the waves in relation to their location.

The aim of the present section is to quantify the influence of the camera viewing angle relative to the incident wave direction on the frequencies and wavenumbers estimated by cBathy v1.1 and the final depth inversion results. Optical images of linear, non-breaking waves propagating over a flat seabed in intermediate water depth have been simulated, where none of the assumptions of the cBathy algorithm have been violated. In addition, the sensitivity of the cBathy v1.1 nonlinear fit to the initial guess of wave direction has been assessed.

4.4.1 Method

A suite of sea states (Table 4-5, Table 4-6) has been probed to improve our understanding of the effect of wave propagation direction on the estimated bathymetry using linear depth inversion. First, synthetic sea surface elevation time series have been generated based on either measured or analytic input spectra. A time series of synthetic imagery from simulated reflected radiance has been built for the simulated sea surface (Chapman, 1981; Chapman and Irani, 1981). Then, the synthetic optical time series have been used as input to the cBathy v1.1 depth inversion algorithm, to estimate the bathymetry. The error has been finally quantified by comparing the estimated bathymetry to the frequencies, wavenumbers, and water depth used to create the synthetic sea surface. In this analysis, the x -axis has been

conventionally thought as the cross-shore direction, while the y -axis has been conventionally thought as the alongshore direction.

4.4.1.1 Input spectra

Two types of input spectra have been considered to generate the synthetic imagery, which included analytic frequency-directional spectra (Table 4-5) and real spectra representative of protected seas characterized also by bi-modal spectra (e.g., Adriatic Sea), (Table 4-6) (Brocchini et al., 2015). Then, to analyse the effects of wave viewing direction, the directional peak of the wave spectra has been varied.

Table 4-5 - Summary of analysed sea states and parameters, from analytical source. For each case the table displays the index, the peak period, the significant wave height, the spreading parameter, the camera height, the camera tilt angle (fixed in the patches) and the water depth.

| case | Tp (s) | Hs (m) | s | hc (m) | tilt (°) | h (m) |
|------|--------|--------|----|--------|----------|-------|
| A10 | 7.00 | 3.00 | 5 | 25 | 14 | 7 |
| A11 | 7.00 | 3.00 | 2 | 25 | 14 | 7 |
| A12 | 7.00 | 3.00 | 10 | 25 | 14 | 7 |
| A13 | 7.00 | 3.00 | 20 | 25 | 14 | 7 |
| A20 | 10.00 | 2.50 | 5 | 25 | 14 | 7 |
| A21 | 10.00 | 2.50 | 5 | 40 | 18 | 7 |
| A22 | 10.00 | 2.50 | 5 | 25 | 14 | 10 |

Table 4-6 - Summary of analysed sea states and parameters, from EsCoSed experiment source. For each case the table displays the index, the peak period, the significant wave height, the wave energy, the camera height, the camera tilt angle (fixed in the patches), the water depth, and the time of measurement.

| case | Tp (s) | Hs (m) | Smax (m ² s) | hc (m) | Tilt (°) | h (m) | time |
|------|--------|--------|-------------------------|--------|----------|-------|----------------------|
| E01 | 8.79 | 2.95 | 10.85 | 25 | 14° | 7 | 25-Jan-2014 02:00:00 |
| E02 | 8.79 | 3.09 | 8.74 | 25 | 14° | 7 | 25-Jan-2014 04:00:00 |
| E03 | 9.44 | 2.99 | 5.31 | 25 | 14° | 7 | 25-Jan-2014 01:00:00 |
| E05 | 4.82 | 0.51 | 0.29 | 25 | 14° | 7 | 26-Jan-2014 06:00:00 |
| E07 | 5.94 | 1.54 | 1.51 | 25 | 14° | 7 | 25-Jan-2014 16:00:00 |
| E08 | 9.44 | 2.92 | 14.21 | 25 | 14 | 7 | 25-Jan-2014 03:00:00 |

The analytic frequency-directional spectra, $S(f, \theta)$, has been expressed as

$$S(f, \theta) = E(f)D(f, \theta) \quad (4.10)$$

where $E(f)$ is the one dimensional, frequency dependent wave spectrum, and $D(f, \theta)$ is the directional distribution, which depends on both frequency, f , and direction, θ . The shape of the frequency spectrum is defined in terms of the significant wave height, H_s , and the mean zero-upcrossing period, T_z , by fitting the JONSWAP spectrum. For $E(f)$, the formulation of Carter (1982) was used, where $T_p = 1.286T_z$ is the spectral peak period,

$$E(f) = G(f)0.0749H_s^2T_z(T_zf)^{-5}\exp[-0.4567/(T_zf)^4] \quad (4.11)$$

$$G(f) = 3.3 \exp\left[-\frac{(1.286T_zf-1)^2}{2\sigma^2}\right] \quad (4.12)$$

$$\sigma = \begin{cases} 0.07 & \text{for } 1.286T_zf < 1 \\ 0.09 & \text{for } 1.286T_zf > 1 \end{cases} \quad (4.13)$$

A simple method has been, instead, used to define the direction distribution (Nwogu et al., 1987; Scarsi, 2009). Consequently, the direction distribution, $D(\theta)$, depends only on the wave direction, θ ,

$$\begin{cases} D(\theta) = D_0 \cos^{2s}[\theta - \theta_p] & \text{if } |\theta - \theta_p| < \pi/2, \\ 0 & \text{otherwise} \end{cases}, \quad (4.14)$$

$$D_0 = \frac{1}{\pi^{0.5}} \frac{\Gamma(s+1)}{\Gamma(s+1/2)}, \quad (4.15)$$

where θ_p is the spectral peak direction, Γ is the Gamma Function, D_0 is the normalization factor and s is the spreading parameter. The parameters used for the analytical spectra are summarized in Table 4-5 and an example of the resulting frequency-directional spectra is shown in Figure 4-18b. Two general cases, characteristic of the Central Adriatic wave climatology, have been used but the results may be generalized for other sites. The first case used $H_s = 3.0$ m and $T_p = 7$ s, is typical of storm waves in the Adriatic approaching the Italian coast from ESE (A10-A11-A12-A13). The second case used $H_s = 2.5$ m and $T_p = 10$ s, is typical of storm waves approaching from NNE (A20-A21-A22). Wave spectra have been then generated for a range of peak directions. In these analyses, the wave propagation direction, α_n , is measured from the x -axis (taken as the cross-shore direction) in the counter-clockwise direction.

The second type of spectra used to develop synthetic imagery comes from observed spectra (Table 4-6). These spectra are representative of the Adriatic winter storm conditions (Brocchini et al., 2017). Observations were collected with a Sentinel Acoustic Doppler Current Profile (ADCP) deployed in about 7.3 m water depth and 850 m offshore of the mouth of the Misa River, Senigallia, Italy (43° 43.588' N, 13° 13.941' E). The spectra were statistically estimated from ADCP velocity observations (Table 4-6). The analysis has focused on a storm that occurred on 25 January 2014. Spectra around the peak of the storm have been selected, for which wave height and energy were maximum (E01-E02-E03-E08). Then, one spectrum has been selected related to the mean storm energy (E07) and one spectrum representative of calm sea conditions (E05). The peak direction of each selected spectrum has been manually modified, shifting the wave angle but preserving the spectral shape and energy (Figure 4-18a).

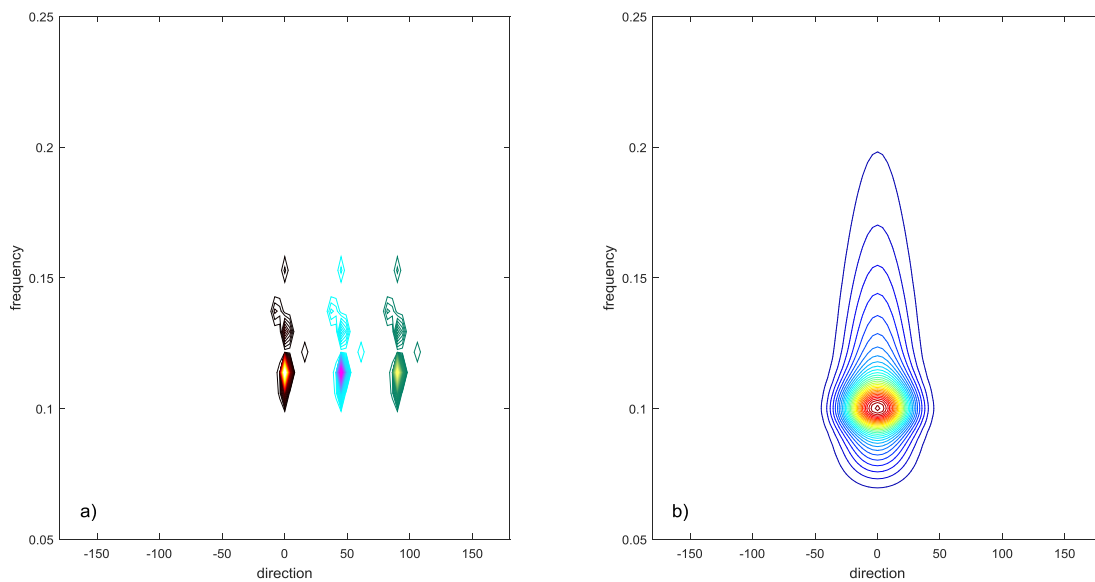


Figure 4-18 – a) Example of peak shifting for case E01 with peak directions of 0° (red), 45° (blue), and 90° (green). b) Example of frequency directional spectrum (A20) designed using equations (4.11) to (4.15).

4.4.1.2 Sea surface simulation

For each of the cases reported in (Table 4-5, Table 4-6) synthetic sea surface time series have been generated within the simulated camera field-of-view following Percival (1992) and Scarsi, (2009). The sea surface elevation time series, $\eta(x, y, t)$, can be represented as

$$\eta = \text{ifft}(W) \quad (4.16)$$

where $\text{ifft}(W)$ is the inverse Fourier transform. The Fourier series is defined as

$$W = A_w(\cos(\varphi) + i \sin(\varphi)) + A_n(\cos(\varphi_n) + i \sin(\varphi_n)) \quad (4.17)$$

where A_w is the amplitude of the wave signal in the frequency domain and is related to the input spectral characteristics; A_n is the amplitude of the noise signal in the frequency domain and is proportional to the noise to signal ratio, while φ and φ_n are the phases of the harmonic variability of the waves and noise, respectively. Since the spectrum is independent of the phase of the harmonic variability, the phases, φ and φ_n , are arbitrary, hence have been computed with a random function,

$$\varphi = \varphi_r - k x \cos \theta - k y \sin \theta, \quad (4.18)$$

$$\varphi_n = \varphi_{r,n} \quad (4.19)$$

with random values, $0 \leq \varphi_r < 2\pi$, $0 \leq \varphi_{r,n} < 2\pi$, and k , the wavenumber. The approach allows for an infinite number of possible time series to be generated with the same input spectrum. Time series for each wave direction have been first generated, and then, summed for all wave directions. Only the real part for the first N_s elements of the transformed series has been considered.

4.4.1.3 Optical model

Synthetic optical time series corresponding to the simulated wave time series have been generated using a radiance modulation model (Chapman, 1981). The radiance reaching the camera sensor from a point on the sea surface, I , depends on the light reflected off the sea surface, as well as the light upwelled from below the sea surface Walker, 1994. I can be expressed as the sky radiance distribution, \mathcal{L} , modified by the Fresnel reflection coefficient, \mathcal{R} ,

$$I = \mathcal{L}\mathcal{R} \quad (4.20)$$

where \mathcal{L} depends on the brightness of the sky, the angle of incidence of the light, and may be modelled in different ways for different sky conditions (Chapman, 1981). Only a uniform sky condition has been considered for simplicity, which is equivalent to considering only the Fresnel coefficient, \mathcal{R} , (Walker,1994),

$$I = \mathcal{R} = \frac{1}{2} \left[\frac{\sin^2(\omega - \omega')}{\sin^2(\omega + \omega')} + \frac{\tan^2(\omega - \omega')}{\tan^2(\omega + \omega')} \right] \quad (4.21)$$

The Fresnel reflection coefficient describes the reflectivity of the surface for an unpolarised radiance source where ω is the angle of incidence of the sky radiance with respect to the sea surface normal. Therefore, ω is equal to the angle of the camera viewing direction with respect to the sea surface normal, while ω' is the angle of refraction related to ω by Snell's law, $\sin(\omega) = 1.34 \sin(\omega')$. The sea surface can be defined by the local wave slope, therefore it is possible to calculate the vector normal to the wave sea surface,

$$r_n = \frac{r_n'}{\|r_n'\|} \quad \text{where} \quad r_n' = \left[\frac{\partial \eta}{\partial x}, \frac{\partial \eta}{\partial y}, 1 \right]. \quad (4.22)$$

The camera viewing direction,

$$r_c = [-\cos \tau \cos \alpha_c, -\cos \tau \sin \alpha_c, \sin \alpha_c], \quad (4.23)$$

depends on both camera tilt from horizontal, τ , and azimuth, α_c , where the latter is measured from the x -axis in the counter-clockwise direction. The incident ray, r_i , can be defined knowing the surface normal and the extrinsic camera parameters as,

$$r_i = 2r_n(r_n \cdot r_c) - r_c \quad (4.24)$$

Then, the incidence angle, ω , can be defined as (Stilwell,1969),

$$\omega = \cos^{-1}(r_n \cdot r_c) \quad (4.25)$$

The Matlab© functions developed to model the synthetic time series based on the work of Chickadel (2007) are available (<https://github.com/Coastal-Imaging-Research-Network/station-design-toolbox>).

4.4.1.4 cBathy

The optical time series generated in Section 4.4.1.3 have been used as input to the cBathy v1.1 algorithm to estimate water depths. Different testes performed with different wave angles have been used to evaluate the sensitivity of cBathy to the wave viewing angle. The cBathy algorithm is described more in detail in Section 4.1. In the current Section only the aspects useful for the synthetic test analysis are highlighted.

The application of cBathy requires an initial definition of the optical time series and of the setting parameters. For this analysis the time series have been synthetic built with the procedure illustrated in Sections 4.4.1.1-3 while the main parameters set in the input file are listed in Table 4-7.

Table 4-7 - Summary of cBathy parameters. The x-axis is the cross-shore direction, and the y-axis is the alongshore direction.

| cBathy parameter name | value | description |
|------------------------------|--|--|
| params.dxm | 9 m | Analysis domain spacing in x |
| params.dym | 13 m | Analysis domain spacing in y |
| params.xyMinMax | [0 1000 0 1000] for Grids [50 250 50 250] for Patches | Spatial extent of the analysis grid |
| params.MINDEPTH | 0.25 m | Min limit set for the nonlinear depth search in phase 2. |
| params.QTOL | 0.5 | Min skill |
| params.minLam | 10 | Min normalized eigenvalue to proceed |
| params.Lx | 2*params.dxm | Smoothing length scales in x |
| params.Ly | 2*params.dym | Smoothing length scales in y |
| params.kappa0 | 3 | Multiplier that increase Lx seaward |
| params.maxNPix | 80 | Max number of pixels per subgrid |
| params.fB | [1/15 : 1/100 : 1/4] | List of frequencies for analysis |
| params.nKeep | 4 | Number of frequencies to keep |
| params.offshoreRadCCWFromx | Variable | Seed angle |

The first step of the cBathy algorithm carries out a frequency-dependent analysis and estimates the (usually four) most coherent pairs of wave frequencies and wavenumbers (see also Section 4.1). Following (Plant et al, 2008), for each analysis point, the algorithm considers a subgrid in which the dominant frequencies are estimated by Fourier transform of the input optical signal and the cross-spectral matrix is computed between all pixel pairs in the subgrid. The cross-spectral matrix is filtered using spatial eigenvector analysis to identify the dominant spatial phase of the waves. The corresponding wavenumbers are derived by fitting the observed spatial phase structure to the wave forward model,

$$v_1'(x, y) = \exp(i[k\cos(\alpha)x_p + k\sin(\alpha)y_p + \phi]) \quad (4.26)$$

where k is the wavenumber, α is the wave direction, ϕ is the scalar phase angle (to provide an appropriate phase shift) and (x_p, y_p) is the sampling point. The values of k are those that yield the best match between observed and modelled wave structures. Initial guesses at the value of wavenumber and wave direction (seed angle) are necessary for this nonlinear fit.

The second step in the cBathy v1.1 algorithm combines the frequency-wavenumber pairs from Step 1 to give a single depth estimate (see also Section 4.1). At each analysis point, the algorithm chooses the $\Omega - k$ pairs from within the subgrid to use in the depth estimate by weighting by distance from the analysis point and skill of the modelled wave phase. Then, the algorithm calculates the depth as the value that yields the best weighted nonlinear fit between the first step $\Omega - k$ pairs and the dispersion Equation (4.1).

The third step carries out a data-assimilation analysis using a Kalman filter to smooth and average the estimated depth results (see also Section 4.1). The third step is neglected in this analysis.

4.4.2 Effects of wave direction on water depth estimation

The procedure described in Section 4.4.1 was applied for each analytical and experimental input spectrum listed in (Table 4-5, Table 4-6).

First, a qualitative investigation of the effects of the wave direction in a “realistic” camera view has been performed, where both tilt and azimuth angles varied over the field-of-view. For the analysis, a grid extending over a 1 km by 1 km region with 3 m resolution, hereinafter called “Grid”, has been used. The camera height was 25 m and the water depth was constant and equal to 7 m. The camera has been located at the origin of coordinate system and looked along the x -direction, but the tilt and azimuth changed over the Grid, so that the angular difference between the wave and camera view directions varied over the Grid. For each case, the wave direction has been varied in the synthetic images to evaluate the sensitivity of the radiance model to the angle difference between the wave direction, α_n , and the camera view direction, α_c , based on the errors in the optical cBathy v1.1 estimation. Three different angles of wave propagation have been inspected, including, 0° or from the x -direction (Figure 4-19a-d), 90° or from the y -direction (Figure 4-19c-f) and 45° (Figure 4-19b-e). Waves approaching from the x -direction have the convention, $\alpha_n - \alpha_c = 0^\circ$.

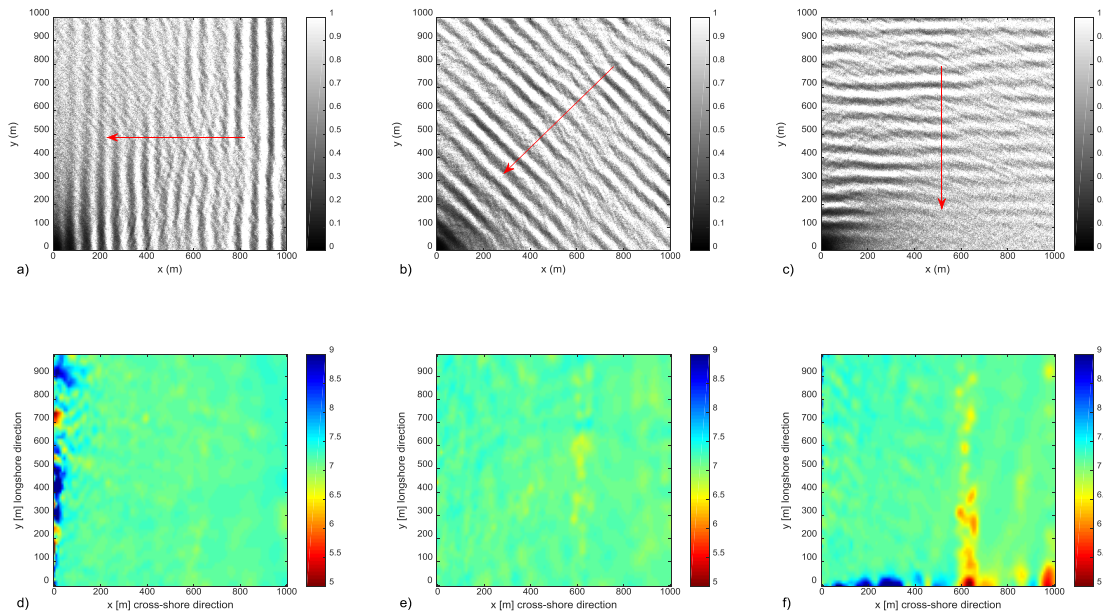


Figure 4-19 - Optical images (upper panels) and estimated bathymetry (lower panels), for case E01, for wave angles equal to 0° (a,d), 45° (b,e), and 90° (c,f). The angles are positive in the counter-clockwise direction from the x -axis. The red arrows indicate the wave direction. The seed angle has been set coherent to wave propagation.

Optical imagery depends on tilt and azimuth angles. The effects of the tilt variation manifest as variation of the intensity magnitude so that when moving closer to the origin of the camera system, the tilt angle increases and the intensity magnitude decreases (Figure 4-19 a,b,c). The effects of the azimuth variation are more complex and they are related to the direction of wave propagation. In fact, changes in wave direction, α_n , are equivalent to changes in azimuth direction, α_c . In the first-order Taylor approximation of the radiance model (Equation 4.27), wave visibility depends on both wave slope, γ_n , and wave viewing angle (Stilwell, 1969; Chickadel, 2007). Therefore, the highest optical contrast occurs when the camera looks in the direction of wave propagation while the waves are generally not visible when the camera looks along the crest in the first order approximation,

$$I \approx I_{\gamma_n=0} + \gamma_n \cos(\alpha_n - \alpha_c) K_1 \quad (4.27)$$

where γ_n is the wave slope and K_1 is a constant.

Qualitatively, synthetic imagery (Figure 4-19) demonstrates the effect of varying $\alpha_n - \alpha_c$ on both image intensity and bathymetric estimation. By increasing the angular difference,

the longer wavelength waves are no longer visible in the optical image, and wave crests propagating parallel to the viewing direction are dominated by high frequency clutter. Likewise, the estimated water depth is more variable in regions dominated by clutter. For example, in Figure 4-19a) and Figure 4-19d), the error is largest close to the y -axis, where the angle difference is maximum (90°), and the error decreased moving toward the x -axis, where the angle difference is minimum (0°). In Figure 4-19b) and Figure 4-19e), the bathymetric error is lower because the angle difference does not exceed 45° . In Figure 4-19c) and Figure 4-19f), the maximum error, corresponding to the maximum angle difference, is close to the x -axis. In these cases, the seed angle used in the nonlinear fit has been set equal to the wave propagation direction.

Subsequently, $\alpha_n - \alpha_c$ has been progressively increased from 0° to 90° over a smaller analysis domain, hereinafter called “Patch”, representative of a small region within a larger image. For this analysis, a 200 m by 200 m region with 3 m resolution has been used. The camera has been located at the origin of coordinate system and looking along the x -direction. The camera tilt has been set to 14° or 18° and the camera height to 25 m or 40m, respectively. The bathymetry has a constant depth of 7 m, and the seed angle has been set equal to the peak direction of the incoming waves. For each combination of input parameters listed in Table 4-5 and Table 4-6, ten random realizations of the sea surface, optical image, and estimated the water depth have been computed. Then, the errors have been calculated and averaged to reduce the noise due to the random phases. The relative error is quantified as,

$$relative\ error = \sqrt{\frac{\sum_{n=1}^N |(n_E - n_T)/n_T|^2}{N}} \quad (4.28)$$

where n_E is the estimated water depth, n_T is the true depth, and N is the number of comparison values.

Consistent with results from the qualitative study and previous studies (e.g. Stockdon and Holman, 2000; Plant et al, 2008), both wave viewing direction and directional spreading influence estimates of water depth. The errors for angular differences of less than 75° are linearly dependent on $\alpha_n - \alpha_c$ (Figure 4-20a, Figure 4-20b); for larger angular differences, the error rapidly increases. For the analytical spectra, the effect of directional spreading of the incoming waves is evident (Figure 4-20b); the magnitude of the error is proportional to the directional spreading of the spectrum. On the contrary, when directional spreading is

small, cBathy v1.1 can provide a good estimate of water depth, even if the viewing angle is large. The tilt angle does not affect the general reconstruction of the bathymetry. This can be observed changing the camera height (see differences between case A20 and case A21) and, as a consequence, the tilt angle (Figure 4-20a). Also the selected water depth does not affect the bathymetric estimation if it respects the algorithm assumptions. In fact, no significant differences can be observed between case A20 and case A22 (Figure 4-20).

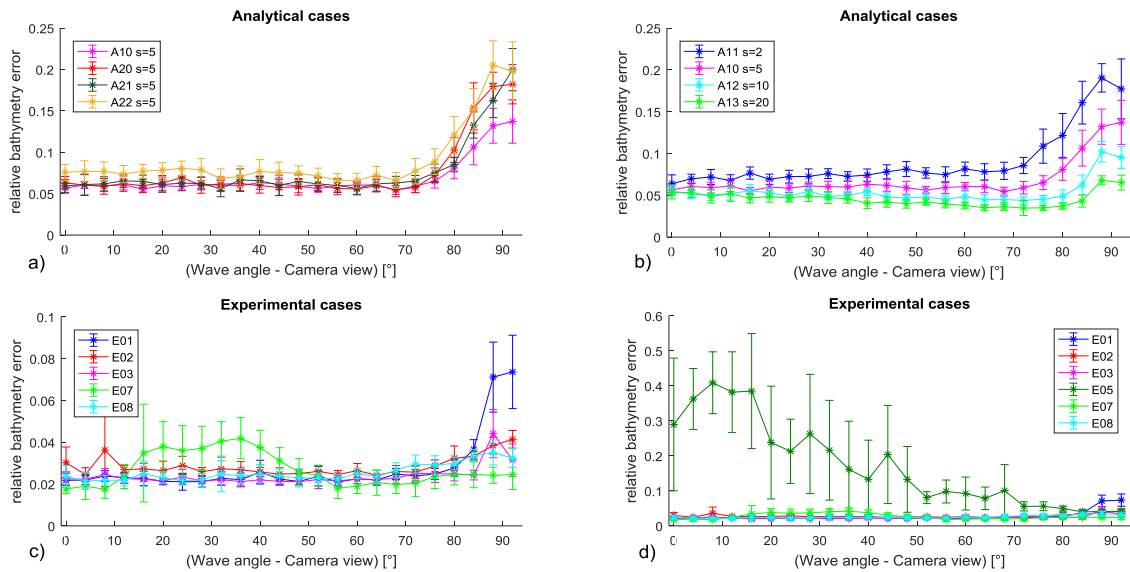


Figure 4-20 – Results of bathymetric error as function of difference between wave angle and camera viewing direction. a) analytical spectra A10, A20,A21, A22; b) analytical cases A10, A11, A12 and A13 with different directional spreading; c) observed spectra E01, E02, E03, E07 and E08; d) same as c) but includes case E05.

Error analysis with experimental spectra has produced similar results to the analytical spectra, with a few notable differences. In most cases the experimental input spectra are less directionally spread than the analytical spectra. The error magnitude of the experimental cases is similar to the error magnitude of the analytical cases with low directional spreading (A13). The error in the bathymetry estimation is also affected by wave height and energy (Figure 4-20c). The most energetic cases (E01, E02, E03, E08) have error shapes similar to the shape of the analytical cases. In contrast, the case E07, which has moderate energy and a moderate wave height, shows a different shape of the error. A large increase in error is observed for case E05 (Figure 4-20.d), which is characterized by a small wave height, short wave period, and low energy. The anomalous behavior of case E05 is also related to its frequency value, which is close to both the deep-water limit and the frequency threshold

defined in the input parameters of cBathy (Table 4-7). Errors for the synthetic tests (order 0.2 m – 0.5 m) over angular differences of $< 75^\circ$ are consistent with the error reported in observational studies when algorithm assumptions are not violated (e.g. Brodie et al, 2018).

4.4.2.1 Seed sensitivity

The sensitivity of cBathy v1.1 to the initial guess of the nonlinear fit coefficients in the first step of cBathy v1.1 has been quantified.

Usually the cBathy v1.1 seed angle is set by assuming that the waves come from the cross-shore direction (0°). However, in operational application of cBathy v1.1 the incoming wave direction varies with time, resulting in the seed angle being a potential source of error in the estimated bathymetry. The new version of cBathy (cBathy v1.2) removes the need to specify the incoming wave angle by estimating the seed angle from the spatial phase structure.

This analysis has been performed using the larger Grid and considering three directions of wave propagation (0° , 45° , 90°). Only one realization has been made for each incident wave direction, but cBathy has been ran spanning over a range of seed angles (from 0° to 90°). The others cBathy parameters are listed in Table 4-7.

Large errors in seed angle results in undulatory features in the bathymetric surface, resulting from poor solutions during the nonlinear fit (Figure 4-21). In all cases, the error is minimized when the seed angle is close to the real wave direction. In the results of Section 4.4.2, the seed angle has been set coherent to analyzed wave propagation.

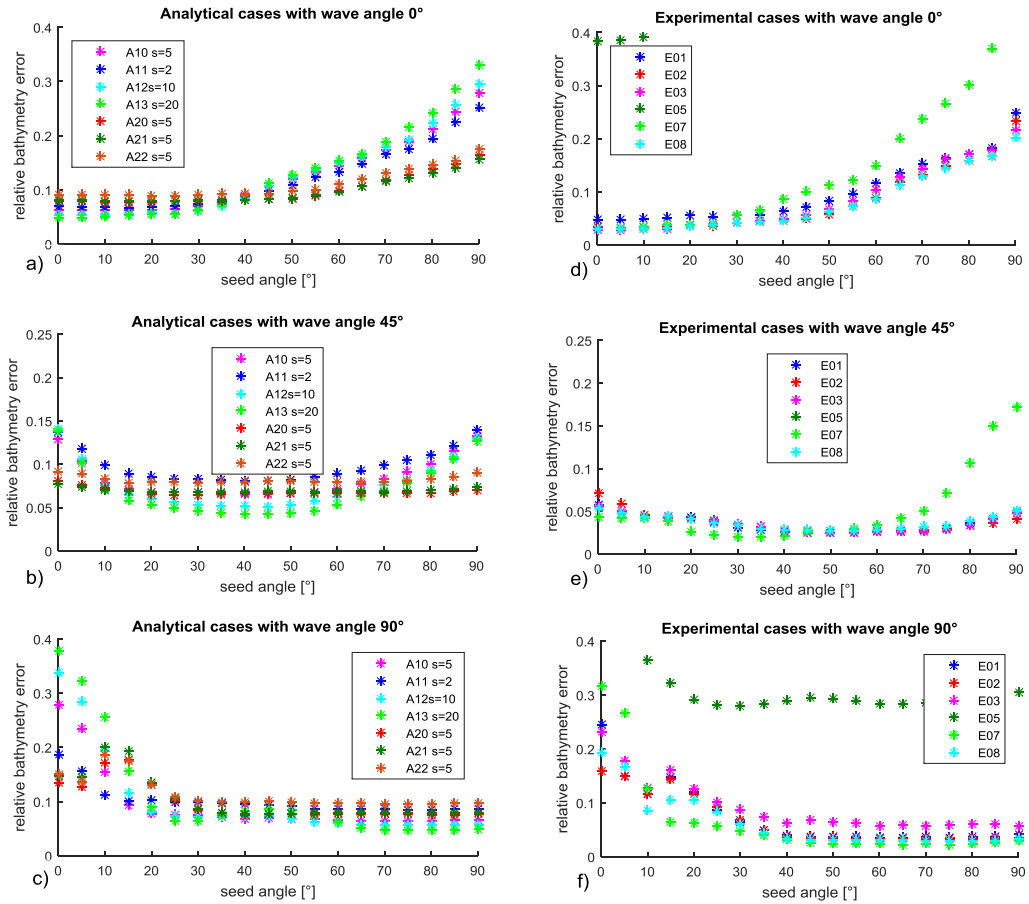


Figure 4-21 – Seed angle sensitivity for analytical (a-c) and experimental (d-f) cases with wave angles of 0° (a,c), 45° (b,e), and 90° (c,f).

4.4.2.2 Frequency and wavenumber estimation

An accurate estimation of bathymetry by cBathy depends upon accurate estimates of frequency and wavenumber, thus the cBathy v1.1 estimates of $\Omega - k$ pairs have been analysed to determine the source of error. The values of frequencies and wavenumbers, estimated from cBathy v1.1, have been compared with the peak of frequencies and wavenumbers from the synthetic spectra. The cBathy v1.1 derived frequencies and wavenumbers come from the four most coherent frequency-wavenumber pairs obtained in Step 1 of the algorithm. The relative error has been calculated for both angular difference analysis and seed analysis. For both analyses, the errors in frequency and wavenumber are proportional to the skill of the fit in Step 1 of the cBathy v1.1 algorithm.

For this analysis, the residual between true and estimated values, with respect to the true value (Equation 4.29) and the relative error (Equation 4.30) have been quantified as,

$$residual = (n_E - n_T)/n_T \quad (4.29)$$

$$relative\ error = \sqrt{\frac{\sum_{n=1}^N |(n_E - n_T)/n_T|^2}{N}} \quad (4.30)$$

where n_E is the estimated value, n_T is the true value, and N is the number of comparison values.

Figure 4-22 and Figure 4-23 present details of the relative difference (Equation 4.29) for the $\Omega - k$ pairs with the highest skill and summary analysis of the relative error (Equation 4.30) for the other $\Omega - k$ pairs.

The difference between true and estimated values is small in cases with waves coming from 0° (Figure 4-22a-b-c), whereas frequency-wavenumber error is large in cases with waves coming from 92° (Figure 4-22d-e-f). Both frequency and wavenumber errors increase for large angles, similar to the trend for the water depth error (Figure 4-22g, Figure 4-22h). This confirms that the error due to a poor signal in the optical image comes from both an error in frequency estimation and an error in wavenumber estimation.

Furthermore, the role of the seed angle in $\Omega - k$ errors in Step 1 of cBathy v1.1 has been investigated. For cases with no error in seed angle, errors in $\Omega - k$ and depth are minimal (Figure 4-23a-b-c). In contrast, errors in wavenumber and depth are large when the seed angle is equal to 90° but frequency, which is defined before the nonlinear fit, is insensitive to the seed angle error (Figure 4-23.d-e-f). Errors near the y -axis are probably due to a poor signal in the optical image, as discussed previously, while the underestimation of the depth in the centre of the field of view is related to an overestimation of the wavenumber and good estimation of frequency (Figure 4-23.g, Figure 4-23.h).

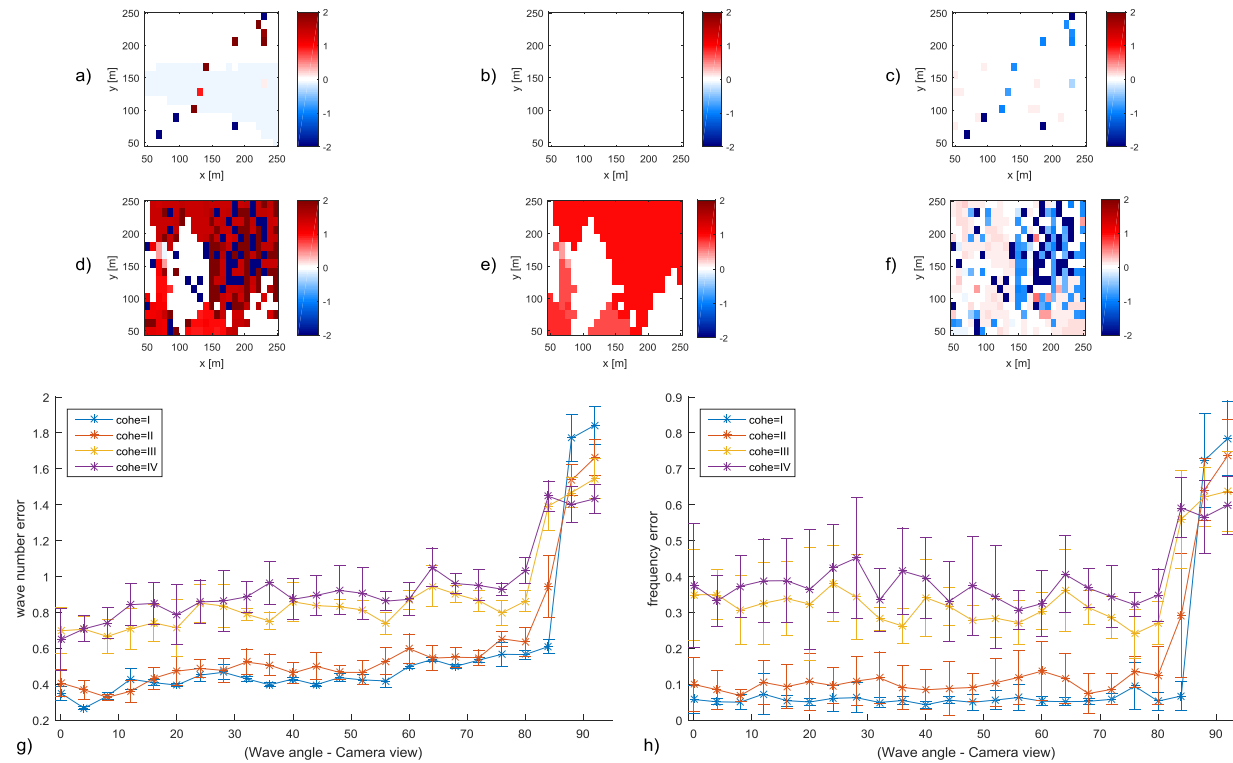


Figure 4-22 – For case E01, the residual calculated using (4.29) for wavenumbers (a,d), frequencies (b,e) and depths (c,f) are plotted. Only the first coherent frequency and one realization for waves coming from 0° (a-c) and 92° (d-f) is illustrated. Mean (*) and standard deviation (bars) of relative error (4.30) are shown for wavenumber (g) and frequency (h) as a function of wave viewing direction.

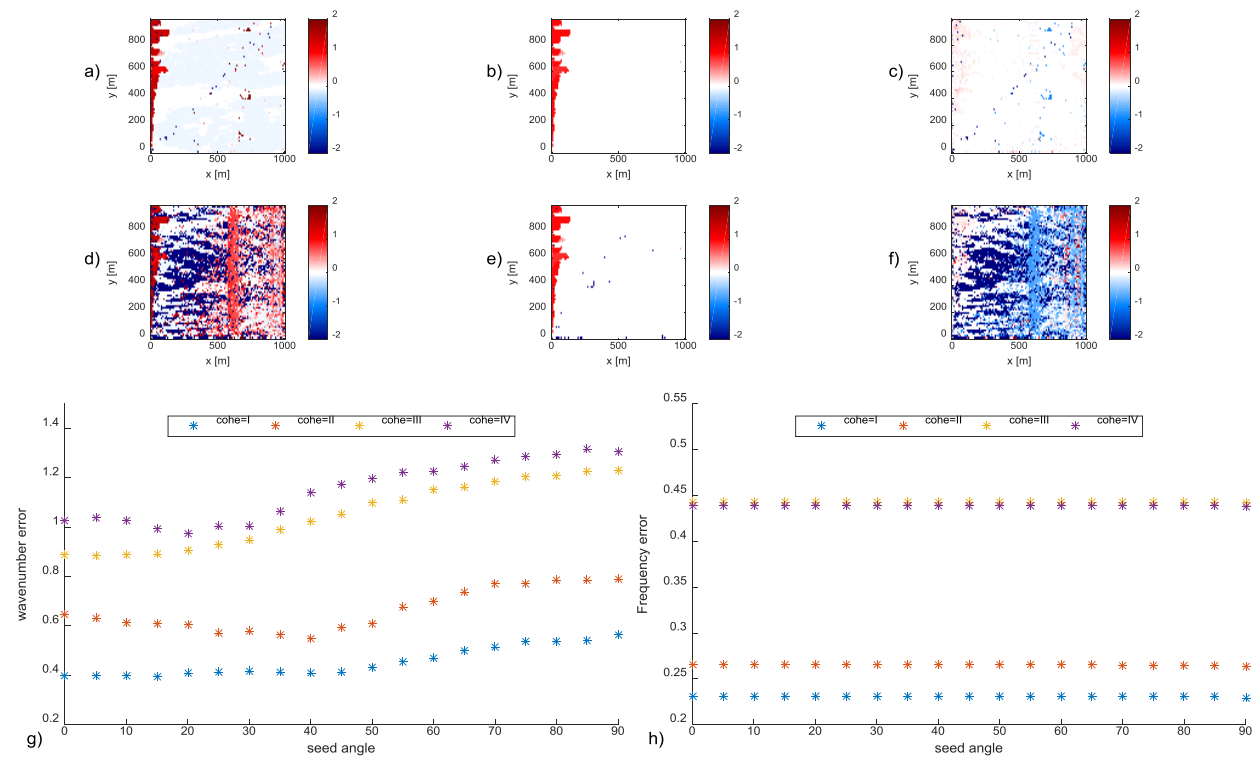


Figure 4-23 – For case E01, the residual calculated using (4.29) for the seed analysis of wavenumbers (a,d), frequencies (b,e) and depths (c,f) are plotted. Only the first coherent frequency for seed equal to 0° (a-c) and 90° (d-f) is illustrated. Relative wavenumber (g) error is affected by seed angle, while frequency (h) is determined before the non-linear fit in step 1 of the cBathy algorithm and is therefore not sensitive to seed angle

Chapter 5 Sandbar analysis

5.1 Sandbar identification

The mildly-sloping beach of Senigallia is in a micro-tidal environment and it is characterized by an array of sandbars, which has been monitored in the past by dedicated bathymetric surveys (Chapter 2). The features and the behaviour of this sandbar system are not yet completely understood and we here try to provide more information by means of the optical data collected by the SGS station. In fact, SGS allows us to monitor the morphological patterns of the analysed area with a very high resolution, larger than that of classical surveys, and for a long period. Quantitative information can be extracted from optical signatures and used to investigate the dynamics of the area. Since the study site of Senigallia is representative of Adriatic sandy beaches near river mouths, this study will also be useful to improve the knowledge of the behaviour of similar coastal environments placed along the Central Adriatic Sea.

Sandbar locations can be indirectly estimated using optical data collected from the SGS station. Detection of submerged bars by video-monitoring is possible due to the correlation between bars and wave breaking (Section 1.2.2). Waves tend to break as they pass over shallow sandbars and previous studies demonstrated that the bar crest position can be correlated with a maximum in image intensity caused by waves breaking over the sandbar (e.g. Lippmann and Holman, 1990; van Enckevort and Ruessink, 2001).

To identify the sandbar positions from video monitoring data Timex images are typically used, i.e. time exposure images derived from the elaboration of the videos collected by monitoring stations. These are the average of the intensity values of each pixel over the sampling period. In this kind of images the areas over which waves break appear as white bands (Section 3.2). Stabilized ortho-rectified images, created from the post-processing of

the sampling videos, have been used to analyse the characteristics of the submerged sandbars of Senigallia. For the SGS station the geometries of the cameras have been calculated only for one image and then it was assumed that they remain the same. However, some little motion was observed due to both temperature differences and wind. For this reason an image stabilization procedure was implemented during the post-processing activity (Section 3.2). The correction of the image movements is important to avoid errors in the sampling of sandbar locations.

To identify the position of the sand bars at Senigallia beach, an Argus toolbox has been used. It is based on the semi-automated Barline Intensity Mapper (BLIM) algorithm developed by van Enckevort and Ruessink (2001). In this algorithm, each vertical row of pixels in a region of interest is scanned from left to right for the maximum intensity value. The vertical positions of the pixels with maximum intensity are then smoothed, which results in a continuous smooth line (Blimline) that follows the location of the high-intensity band in the image. Figure 5-1 shows an example of sampling Blimlines and also the intensity profile along three cross-shore sections for the analysed area.

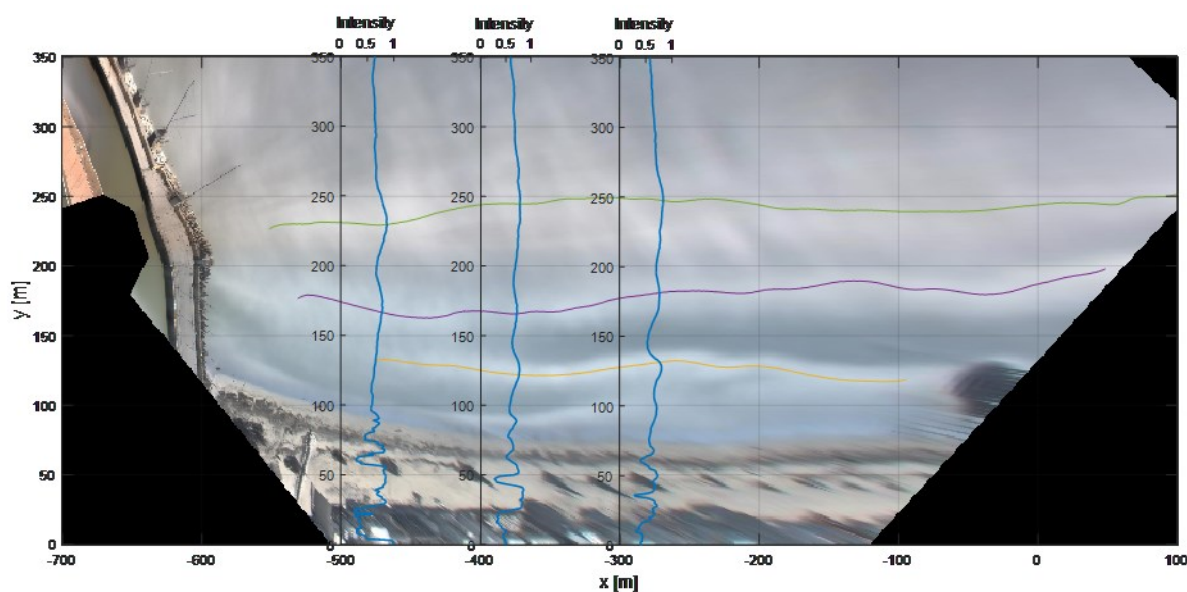


Figure 5-1 – Extrapolation of intensity from imagery. Three Blimlines are identified in the images (green, violet and orange lines). The vertical continuous black lines indicate the location of three cross-shore sections (-500m, -400m, -300m) for which the sampling intensity profile is shown (blue lines).

The Blimline is the sampling of the maximum image intensity and represents the location of preferential wave breaking. This indicates the presence of a submerged sandbar or of an

inner terrace but it is not necessarily the location of the crest of the sandbar. Hence, a more detailed analysis is needed to define the correlation between the bar crest positions and the location of the image intensity. Also the wave climate and tide, affecting the breaking area, should be analysed, but this requires more recent bathymetries and in-situ surveys. For the present thesis, the Blimlines have been taken as representative, with a suitable accuracy, of the sandbar locations.

The available Timex images from 2015 to 2017 have been used to create a database of sampled sandbar locations. Then, one image per day has been chosen for further analyses. In this choice, the effects of tidal sea level changes have not been accounted for, in view of the small tidal range of the site, and images with the clearest wave breaking patterns have been manually selected. To indirectly extract the sandbar locations from the wave breaking patterns, the latter ones must be visible in the images, this depending on the current wave climate. During calm sea conditions, waves are small and do not break over the bars, thus sandbars cannot be identified and the corresponding images must be neglected. On the contrary, during important storm events, it is not possible to identify a region of prevailing breaking, because a persistent surface foam makes the surf zone too wide to extract sandbar locations. Also in this case the images must be neglected. At the end of this analysis a set of images, with variable sampling time, has been obtained. Using the BLIM toolbox, the breaking lines of all the selected images have been semi-automatically sampled.

Previous studies have shown that the Senigallia beach is characterized by three alongshore uniform orders (Chapter 2) of sandbars. However, such three orders of bars are not visible in all images. The outer bar, located in deeper water, is usually identifiable only for the more intense sea states, while the signature of the inner bar, located in very shallow water, sometime gets confused with the shoreline. Moreover, the bars do not have a perfectly linear shape and the shape complexity complicated the bar identification process. Near the harbour, a shallow-water region is observed due to the natural accumulation of the sand near the pier structure, this also complicating bar identification. At the end of the bar identification procedure a set of Blimlines, divided in three orders, has been obtained.

The results found using the BLIM toolbox have been compared with the bathymetries available from the surveys to evaluate the capability of the optical technique to correctly identify the position of the sand bars. The analysis confirmed a fairly good agreement

between the digitized sandbar positions and the location of the crests highlighted in the surveys executed in 2010-2013. Figure 5-2 shows an example of the comparison between the bar crests identified from ortho-rectified Timex image and the bar crests identified from the bathymetric survey of 2013. Three sand bars were consistently observed and variability is related to seasonal evolution of the bars, particularly for the outer one, which is the more variable in position and size, as shown in Postacchini et al. (2017).

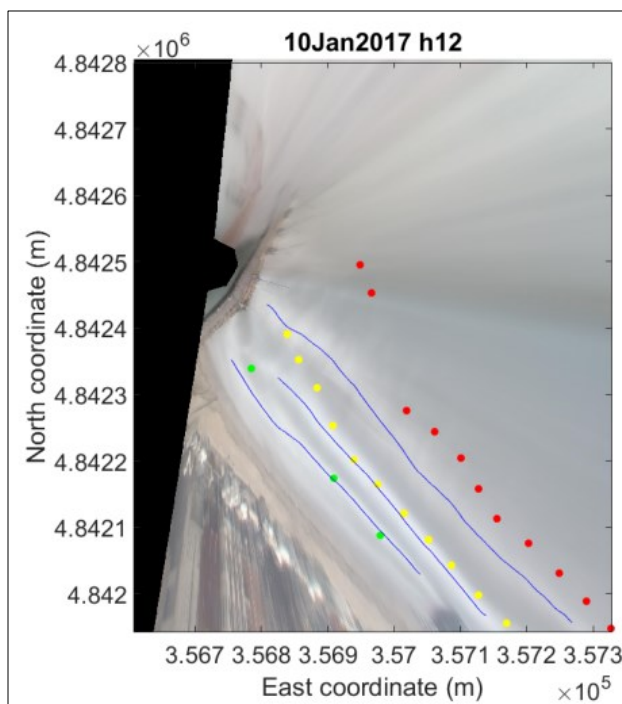


Figure 5-2. Example of bar crest identification from stabilized ortho-rectified Timex images and comparison with the bathymetric survey of 2013. Blue lines give the breaking lines from BLIM; red, yellow and green dots are, respectively, the location of the outer, intermediate and inner bar crests from the bathymetric survey.

5.2 Morphological features

The results obtained from the bar identification process have been analysed to describe the morphological features of the sandbar system of Senigallia.

In general, the sandbars can be linear and longshore uniform (2D) or display a more complex shape, such as an oblique orientation or longshore rhythmic crescentic form (3D). Linear shore-parallel sandbars are usually related to cross-shore dynamics and sediment transport,

while the three-dimensional sandbars are related to current circulation patterns. Many authors (Wright and Short, 1984; Lippmann and Holman, 1990; Armaroli and Ciavola, 2011; Price and Ruessink, 2011) classified the beach morphology using statistical observation approaches, improving the traditional summer-winter profile approach to better describe the morphodynamic evolution of barred-beaches.

Two different approaches are generally used to explain the generation of nearshore sandbars. The first of these is the “forced-response mechanism” (Holman and Sallenger, 1993), which regards the initial formation of the bars as a passive response of the seabed to the hydrodynamic forcing. The second model is the “self-organization mechanism” (Plant et al., 2001), which states that sandbars are formed because of the growth of seabed perturbations by the strong interaction between sediment transport, waves and currents.

After their formation sandbars interact with waves and currents and display morphological changes and a cyclic behavior characterized by migrations both in offshore and onshore direction. To study bar evolution, the researchers mainly explored three different migration mechanisms. In the Net Offshore Migration model (NOM) the bar is generated close to shore. Then, the bar shows an alternation of slow onshore movements during calm conditions and quick offshore movements during storm conditions that lead to a net seaward migration. Finally, the bar degenerates at the outer surf zone (van Enckevort and Ruessink, 2003). In the Net Onshore Migration model (NOnM), instead, the bar is generated at the breaking point, due to the interaction of undertow, wave orbital velocity asymmetry and infragravity waves, and then undergoes a net onshore migration (Aagaard et al., 2004). The third model used to evaluate the bar evolution is the Oscillation around a Position of Equilibrium (OPE), which suggests a cyclic oscillation of the bar position under alternate calm and storm condition, with no net motion to either the offshore or the onshore (Certain and Barousseau, 2005). The latter behavior is typical of regions where the duration of the storms is shorter than the time necessary to induce bar migration. To predict the bar migration, also several numerical models have been developed. In general, a rapid offshore migration has been observed under high energetic conditions and has been related to the breaking-induced undertow (Gallagher et al., 1998). A gradual onshore migration has been observed under milder, but not weak, wave conditions and has been related to wave acceleration skewness (Hoefel and Elgar, 2003).

Observing the plane view distribution of the Blimelines extracted from the SGS images, some morphological characteristics of the sandbar system of Senigallia can be determined. Overall, a multiple bar system located between 100 m - 300 m in the cross- shore direction (local coordinates) has been observed, confirming previous studies (Postacchini et al., 2017). The bar system is composed mainly by three orders of bars that are typically alongshore uniform, but occasionally display some planar complexity. For example, sometimes two different breaker lines join together (see Figure 5-3e and Figure 5-3f), perhaps indicating some “bar welding”, while other times a single breaker line divide into two separate lines, as shown in Figure 5-3c, this gap generation within an alongshore bar can possibly indicate the presence of a rip current. Moreover, for specific conditions bars may not extend over the entire length of the observed coastline (Figure 5-3a and Figure 5-3b). Additionally, the linear development of the bars is modified by the presence of the harbor, this resulting in a bending of the bars (see Figure 5-3d). The shallow depths near the harbor sometimes produce also very complex breaking patterns. Multiple bands of breaking have been sometimes observed near both the harbour and the Rotonda pier. As mentioned above, the third (outer) bar is not always evident, while the first (inner) bar is very close to the shore and sometimes emerges during very low tide periods. The first bar can also be regarded as an inner terrace. In general, tidal modulation of wave braking can weakly influence bar identification. Moreover, the waves coming from ESE are characterized by longer wavelengths and higher sea surge that can prevent the breaking of the smaller waves over the bars. Finally, complex morphologies have been observed particularly during calm periods.

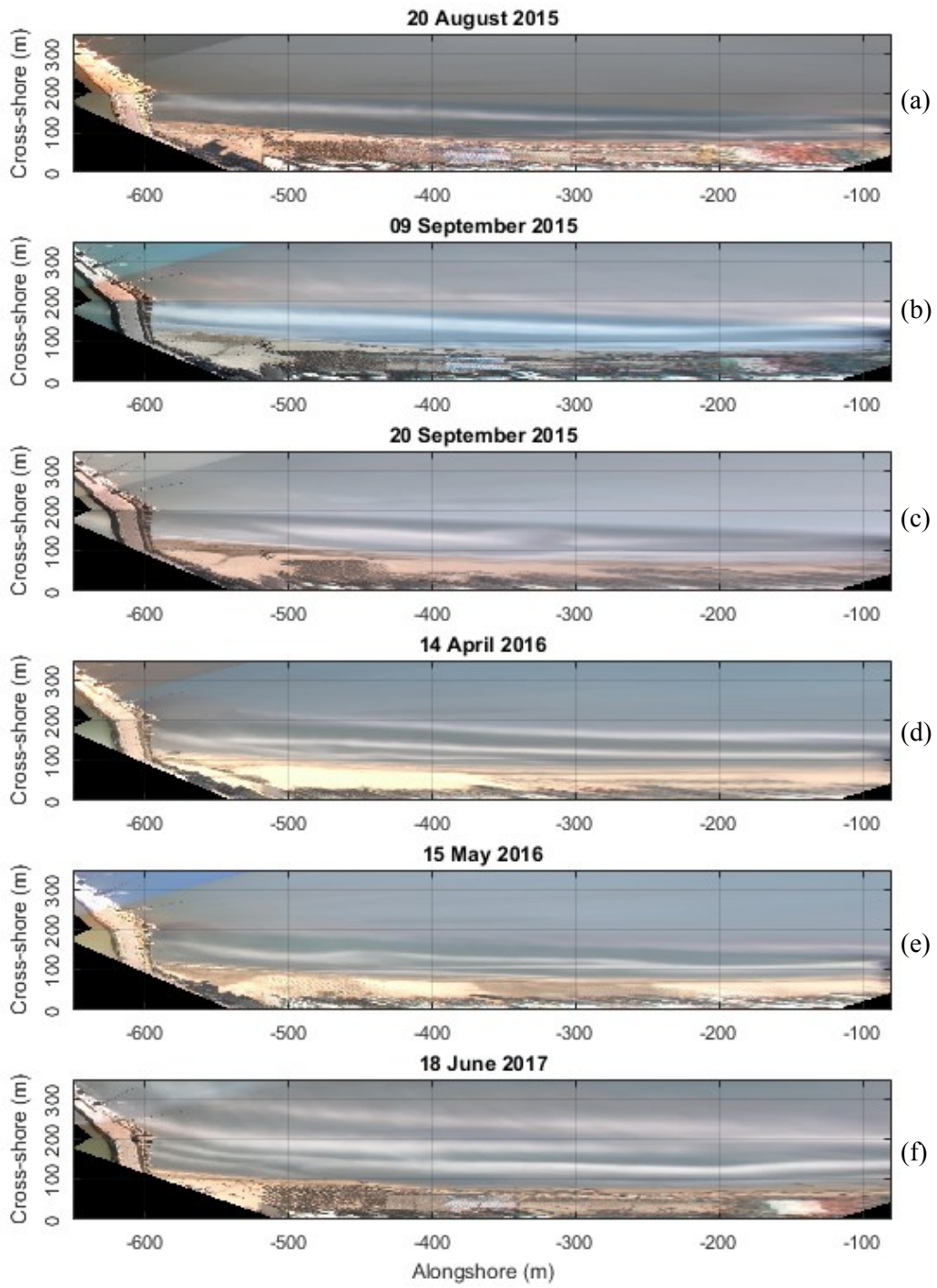


Figure 5-3 Sandbars configurations occurring during the SGS station functioning.

5.3 Morphodynamic evolution

The remote sensing of the sandbars of Senigallia allowed us also to observe the evolution of the bar system in time. On the contrary of in-situ surveys, the video-monitoring technique allows one to investigate also short- to medium-time processes (Section 1.2.2). The analyses of present section focus on the effect of seasonal wave climate and on individual storm events.

From a preliminary analysis, a moderate sandbar movement has been observed, even if important offshore migration has been occasionally detected. As well-known from the literature, the cross-shore bar migration is strongly correlated with both wave climate and currents. Therefore, the sandbar evolution has been related to the local wave climate.

The wave characteristics used for this analysis have been derived from the COAWST Model, a global circulation model available for the Adriatic Sea (see Section 2.1.1). In detail, the time series of wave height, wave period and wave direction of the point P2 of the model has been used (Section 2.1.1). The time series are those of the years 2015-2016-2017. During this time the waves came predominantly from NNE or NE and rarely (only in 2016) from ESE (Figure 5-4). Since the waves coming from ESE are typically more energetic, the preliminary visual analysis focused on this year. In particular, we see that in the end of the February 2016 (29 February 2016) a very intense storm came from ESE (storm 6 of Figure 5-4, see also Figure 5-8).

Figure 5-5 shows a preliminary link between the modelled wave height time series at point P2 and the migration of the sand bars, from January to September 2016. All the storms occurred in this period came from NNE, exception made for the storm of February 28-29 (storm 6), which came from ESE and, therefore, was, theoretically, the most energetic storm of the observed period. Inspection of the bar positions, before and after the storm (panels b and c of Figure 5-5), reveals a rapid shift toward offshore of the breaker line, and consequently of the submerged bars, particularly for the outer and intermediate bars. Overall, the outer bar was more influenced by single storm events than the inner and other bars. No relevant modifications of the bar positions occurred over the rest of the analysed period, even if other intense storms occurred.

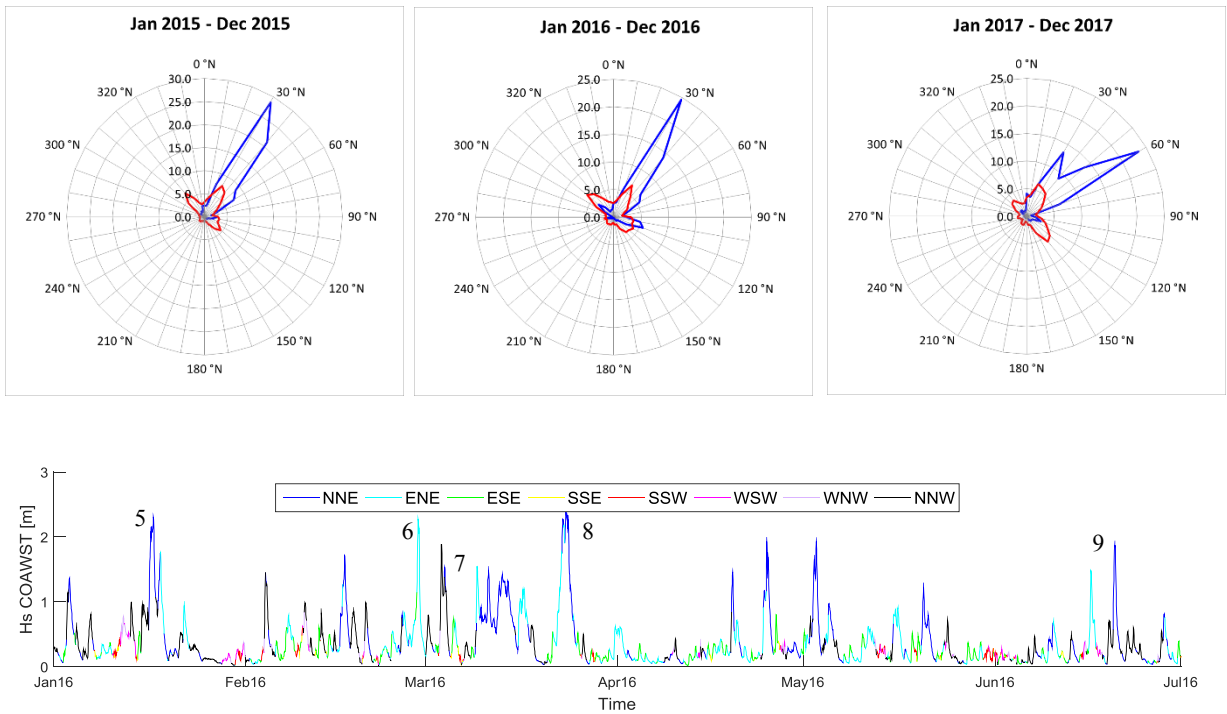


Figure 5-4 Wave climate from the COAWST model. The three upper panels show the frequency distribution of significant wave height (red line) and wave energy flux (blue line), in the years 2015, 2016 and 2017 (respectively from left to right). The lower panel shows the time series of the significant wave height for the first six months of 2016. The variation of the colour indicates the wave direction. The numbers indicate the progressive storms

The storms coming from NNE were in less energetic and were not able to significantly modify the cross-shore position of the bars, though some local changes, mainly in alongshore direction can be observed, in particular for the inner and intermediate bars (panels from d to f of Figure 5-5).

Given the alongshore linearity of the bars, only the alongshore mean bar position has been analysed in this study. This allows us to reduce the cross-shore bar location to a single point. Studying the mean bar position, on one side makes it easier to track the bar and its correlation with the wave climate, but, on the other hand, this can generate errors if the bars are not sufficiently linear. Moreover, the effects of the wave climate on the alongshore variability cannot be taken into account.

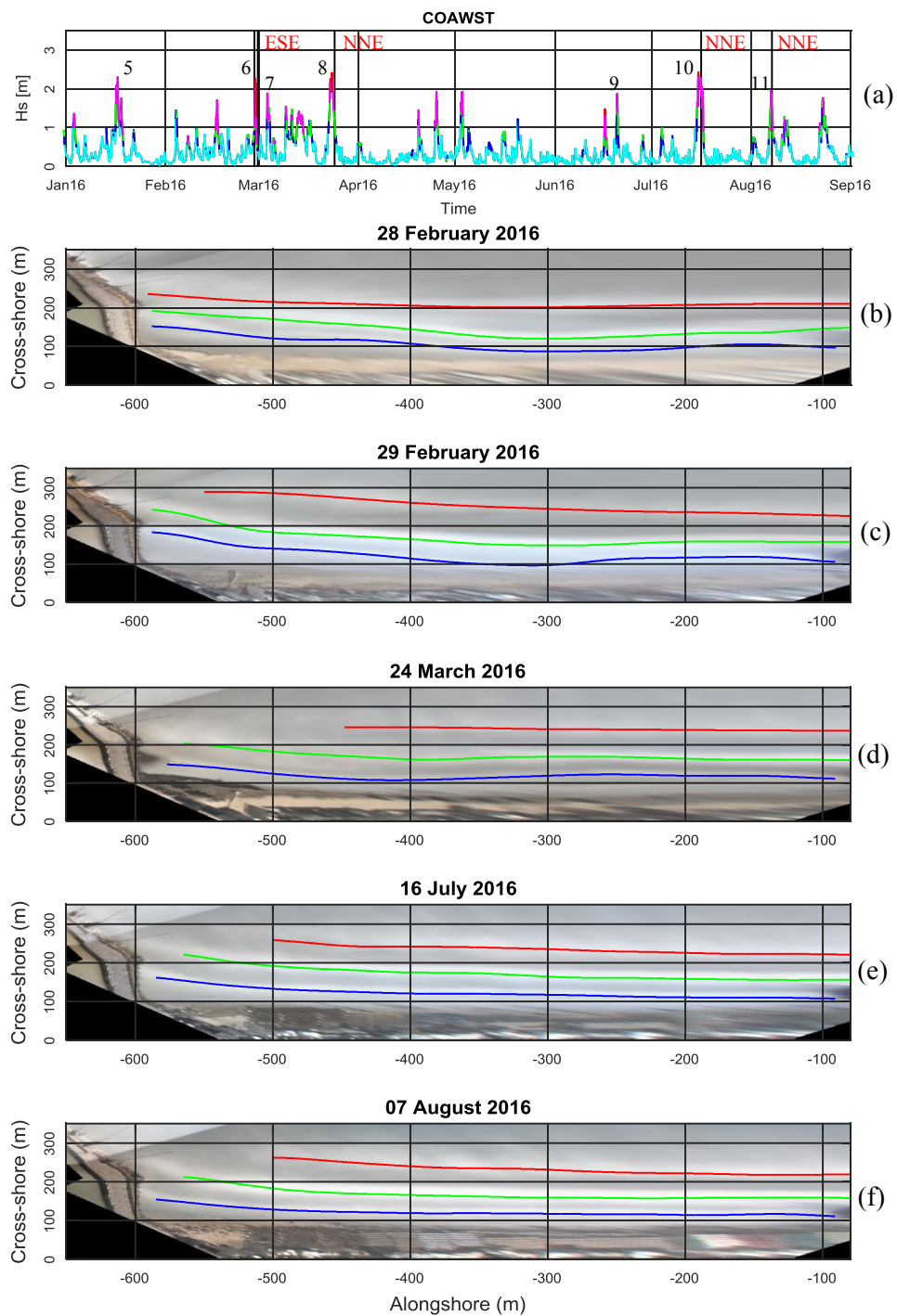


Figure 5-5 - Sandbar position in relation to the wave climate. (a) Significant wave height from the COAWST model. The variation of the colour indicates the wave periods (light blue <math>< 5s</math>, blue=$5s$, green=$6s$, magenta=$7s$, red>$7s$). The numbers indicate the progressive storms. The vertical black lines indicate the days shown in the bottom panels. (b)-(f) breaker lines extracted from Timex images: blue, green and red lines are for inner, intermediate and outer bars respectively.

Figure 5-6 shows, in the upper panel, temporal and spatial variability of the cross-shore mean locations of the three sandbars visible at the Senigallia beach, for the whole analysed period. The related significant wave height computed at point P2 by the model is plotted in the lower panel.

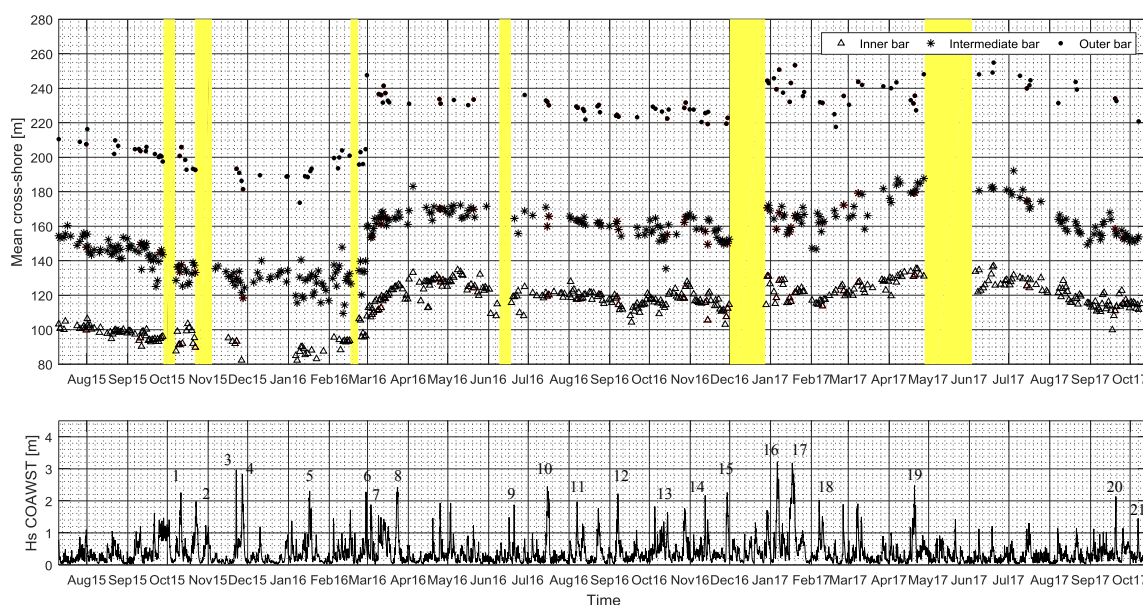


Figure 5-6 Correlation between the mean sand bar location (upper panel) and the wave climate (lower panel), for the full analysed period. The numbers indicate the progressive storms. The yellow bands indicate the period in which the station did not work.

The overall analysis shows the same behaviour for all the three sandbars, with synchronous movements for the inner and intermediate bars and a slightly different behaviour for the outer bar. In fact, the outer bar seems to be more influenced by one single storm event (e.g. 15-22 January 2017, storms 16-17) than the others. In general, an onshore migration is observed between July 2015 and February 2016, a gradual offshore migration between February and April 2016, with a net offshore movement on 29 February 2016, as visually observed above. Then, the bars weakly migrated onshore until January 2017 and again weakly offshore until May 2017. Finally, an onshore migration is observed to occur over the last part of the analysed period. Even if a very strong correlation between the net bar movement and single storms is not clearly observed (except for the storm of 29 February 2016), offshore migration generally occurred during periods of intense wave forcing, similar to other field observation (Lee et al., 1998; Alexander and Holman, 2004). The main onshore

migration, instead, occurred during periods of persistent mild wave forcing (e.g. in agreement with Hoefel and Elgar, 2003 and Hsu et al., 2006).

Focusing on the mean cross-shore locations of the intermediate sandbar in 2016, the net offshore migration of 29 February, and the subsequent weak bar movements, already visually observed, is inspected in detail. Figure 5-7 shows the correlation between this observed behaviour and the modelled wave climate.

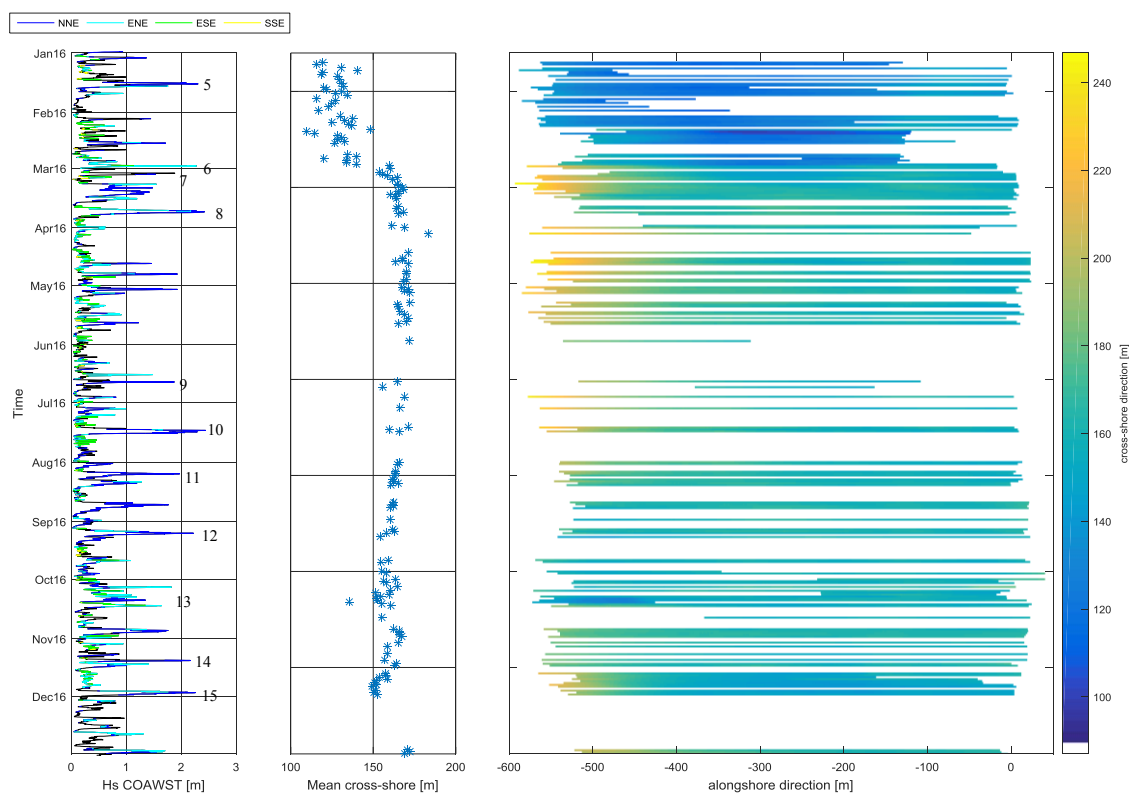


Figure 5-7 – Correlation of the cross-shore mean intermediate bar position (central panel), the alongshore variability (right panel) and the wave climate for year 2016 (left panel). The numbers indicate the progressive storms.

Also the alongshore variability is reported in this figure, where the colour variation indicates the cross-shore position (a bar with constant colour is more straight than a bar that changes colour). The variation of colour along the wave height time series indicates the variation of wave direction and highlights that a net offshore migration only occurs as forced by the single storm coming from ESE. The offshore migration can be quantified in about 50 m.

To better understand the nature of this observed behaviour, the energy flux has been calculated for the storm events. For this analysis, the wave data of point 3 of the COAWST model has been used (Section 2.1.1).

Storm events have been identified through the wave height time series using the “Peak Over Threshold” (POT) method. The threshold has been chosen as the wave height that is exceeded 2% of the time. The events shorter than (or equal to) 3 hours have been neglected in this analysis.

By considering one single storm event, the wave height (H_s), peak period (T_p) and direction with respect to the cross-shore direction (θ_0) are available for each hour of the selected storms.

The total energy flux (F) has been calculated as the sum of the total energy fluxes of each hour (F_i):

$$F = \sum_{i=1}^{N_h} F_i = \sum_{i=1}^{N_h} E_i \cdot c_{gi} \quad (5.1)$$

where N_h is the number of hours. For a specific hour the total energy flux has been calculated as the product of the total wave energy over one-meter square (E_i) times the group speed (c_{gi}). The total wave energy and the group speed have been computed as:

$$E = \frac{1}{8} \rho_a g H_s^2 \quad (5.2)$$

$$c_g = \frac{1}{4\pi} g T_p \quad (5.3)$$

where ρ_a is the water density and g is gravity acceleration.

The flux has then been decomposed into the cross-shore component and the alongshore component, respectively:

$$F_x = F \cdot \cos(\theta_0) \quad (5.4)$$

$$F_y = F \cdot \sin(\theta_0) \quad (5.5)$$

Where θ_0 is the offshore wave direction with respect to the cross-shore direction, positive clockwise, looking towards offshore.

Figure 5-8 shows the results of the analysis. The most important events, both in terms of energy and temporal duration, occurred at the beginning of January 2017 and correspond to an offshore migration. This confirms the occurrence of significant offshore transport under important storm events, however, the net movement of February 2016 has not been highlighted by this analysis. The main difference between storm 6 of 29 February 2016 and the other storms is the angle of the incident waves. During storm 6 the waves coming from ESE approach the shore with a larger angle than the storms coming from NNE that approach the coast in shore-normal direction.

The offshore bar migration, that usually occurs during important storm events characterized by high offshore significant wave height, has been linked to the strong undertow generated under breaking waves (Gallagher et al., 1998). The undertow is an offshore-return current fed by the water volumes brought shoreward by breaking waves (Svendsen, 2006). It is more intense near the bar crest and erodes the shoreward side of the bar to deposit the sediment on the seaward part. Nevertheless, in case of oblique incident waves also the role of the longshore current cannot be neglected since it increases the amount of the resuspended sediment that can be transported. The importance of the longshore current on bar migration has been also highlighted by Walstra et al. (2012) who observed that, for large incident wave angles, the longshore wave-driven current influences the magnitude of the bed shear stress and subsequently the sediment transport and the bar amplitude response.

In order to investigate the possible link between an offshore bar migration, the undertow and the longshore current two storm events (Table 5-1.), with similar wave height but different direction and different effects on bar movement, have been analysed through an analytical computation of the undertow current and the longshore current. Then, a criterion to define a net offshore sediment transport has been used.

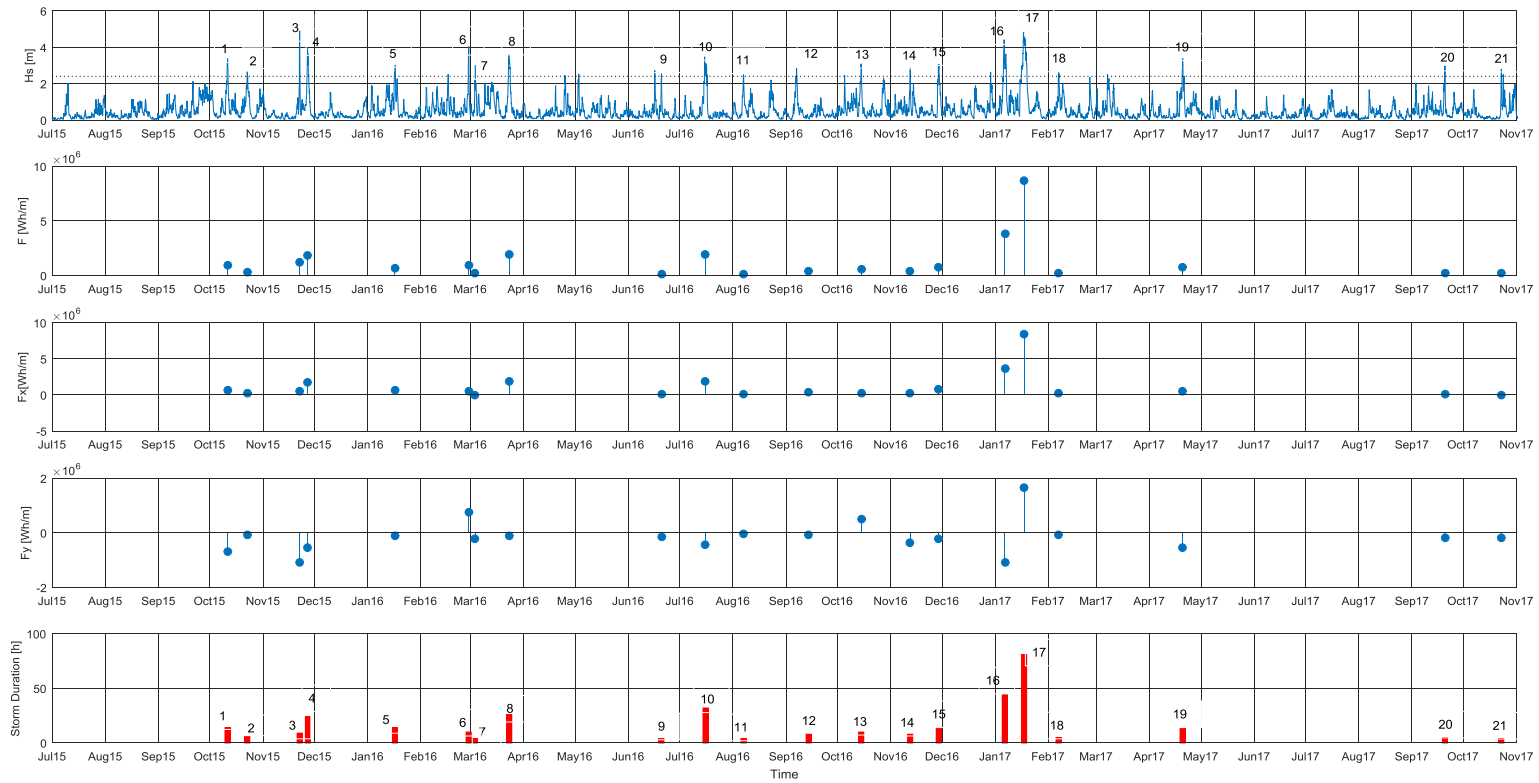


Figure 5-8 From the upper to the lower panel: significant wave height time series from P3 of the COAWST model, the numbers indicate the progressive storms; total energy flux for each storm; cross-shore component of the energy flux; alongshore component of the energy flux; duration of the storms in hours.

Table 5-1 Wave characteristics of two representative storms from the COAWST model. H_s is the significant wave height, T_p is the peak wave period, θ is the wave direction with respect to the cross-shore direction, positive clockwise, looking towards offshore. Test 1 is the ESE storm n.6 of Figure 5-8, while Test 2 is the NNE storm n. 8 of Figure 5-8

| | P1 COAWST (depth=5m) | | | P3 COAWST (depth=50m) | | |
|--------------|----------------------|---------|------------|-----------------------|---------|------------|
| | H_s | T_p | θ_0 | H_s | T_p | θ_0 |
| TEST 1 - ESE | 1.856 m | 8.348 s | 25.9143° | 3.142 m | 8.348 s | 60.5563° |
| TEST 2 - NNE | 2.11 m | 7.368 s | -12.4427° | 3.153 m | 7.368 s | -16.8747° |

The wave characteristics of the two representative storms are shown in Table 5-1. Test 1 is storm 6 of Figure 5-8, coming from ESE and forcing an important offshore migration, while Test 2 is storm 8 of Figure 5-8, coming from NNE and forcing no significant bar migration. The wave information of point 3 of the COAWST model has been used, thought to be representative of wave characteristics in deep water. Then, the propagation of regular waves, only affected by shoaling and refraction has been considered:

$$H = H_s K_s K_r \quad (5.6)$$

$$K_s = \frac{\cosh(kh)}{\sqrt{kh + \sinh(kh) \cosh(kh)}} \quad (5.7)$$

$$K_r = \frac{\sqrt{\cos(\theta_0)}}{\sqrt{\cos(\theta)}} \quad (5.8)$$

where H is the local wave height, H_s is the deep water wave height, K_s is the shoaling coefficient, K_r is the refraction coefficient, k is the local wavenumber, h is the local water depth, θ_0 is the deep water wave angle with respect to the cross-shore direction and θ is the local wave angle calculated by the Snell's law. The wavenumber has been determined by iteratively resolving the linear dispersion relation (Equation 4.1) and knowing that point 3 of the COAWST model refers to a 50 m water depth. For the seabed profile a transect of the bathymetry of the 2013 survey has been used (section 2.1.2). The breaking point is determined by assuming saturation at the value $\delta = H/h = 0.78$, this also giving the wave height inshore of the breaking point.

The undertow has been analytically computed following Rattanapitikon and Shibayama (2000) and the application of their formulation made by Abreu et al., (2012). The depth-averaged time-mean undertow velocity (U_b) was assumed to be composed by the mean velocity due to the Stokes drift (U_w) and the mean velocity due to the surface roller (U_r):

$$U_b = U_w + U_r \quad (5.9)$$

Seaward of the breaking point, the effect of the surface roller is negligible, as there is no surface roller in the offshore zone. To define the more appropriate formulation of U_w and U_r the authors investigated the performance of various formulas suggested by the previous researchers and chose the best one. From the adaptation of the various formulations present in the literature with available experimental data Rattanapitikon and Shibayama (2000) determined the following expression:

$$U_b = -0.76 \frac{B_0 g H^2}{c h} - b_3 1.12 \frac{B_0 c H}{h} \quad (5.10)$$

$$b_3 = \begin{cases} 0 & \text{offshore zone} \\ \frac{1/\sqrt{H} - 1/\sqrt{H_b}}{1/\sqrt{H_t} - 1/\sqrt{H_b}} & \text{transition zone} \\ 1 & \text{inner surfzone} \end{cases} \quad (5.11)$$

$$B_0 = 0.125 + 0.6m - 0.089 \frac{H}{h} \quad (5.12)$$

where $c = \Omega/k = L/T$ is the phase velocity, g is the acceleration of gravity, B_0 is the wave shape parameter, H is the wave height, H_b is the wave height at the breaking point, H_t is the wave height at the end of the transition zone, h is the mean water depth, T is the wave period, L is the wave length and m is a uniform bottom slope.

The longshore current has been analytically computed based on the formulation of Longuet-Higgins (1970):

$$V = \frac{h}{h_b} \begin{cases} V_0 & h < h_b \\ 0 & h > h_b \end{cases} \quad (5.13)$$

where h is the local water depth, h_b is the water depth at the breaking point and V_0 is the maximum longshore velocity at the breaker line with no horizontal mixing. The adopted

formulation of V_0 follows the indications of the Coastal Engineering Manual (2003) and is computed as:

$$V_0 = \frac{5\pi}{16} \frac{m}{C_f} \sqrt{\gamma} \sqrt{g H_b} \sin(\theta_b) \cos(\theta_b) \quad (5.14)$$

where γ is the height-to-depth ratio of breaking waves in shallow water, θ_b is the wave angle at the breaking line and C_f is a friction coefficient due to the waves and currents and commonly taken equal to 0.01. This formulation has a triangular shape with a strong discontinuity at the breaking point since it does not take into account the effects of the presence of horizontal mixing. Horizontal mixing smooths the triangular profile. Following Lounguett-Higgins (1970), it is possible to consider the effect of mixing on the velocity at the breaking line by multiplying for the coefficient β , with suggested value of 0.2.

$$V_b = \beta V_0 \quad (5.15)$$

V_b is the longshore velocity at the breaker line by considering the presence of horizontal mixing, but the smoother velocity profile has maximum shifted closer to shore. The Shore Protection Manual (1984) suggests to multiply the velocity at the breaking line by 2.3 to have the maximum velocity with mixing effect.

The criterion selected to define a net offshore sediment transport is based on Wang, 2016 and states:

$$\frac{w_s}{U_b^*} \leq 0.8 \quad (5.16)$$

where w_s is the settling sediment velocity evaluated with the Zanke (1977) formulation (see Section 2.1.2), $U_b^* = \sqrt{\tau_b / \rho_a}$ is the friction velocity, ρ_a is the water density and τ_b is the bed shear stress. The quadratic friction equation due to undertow and longshore current is written as:

$$\tau_b = \frac{1}{2} \rho_a f_c (U_b'^2 + V_b'^2) \quad (5.17)$$

$$f_c = 2K_v^2 \left(\frac{1}{\ln\left(\frac{h}{k_s}\right)} \right)^2 \quad (5.18)$$

where f_c is a friction coefficient (Wang, 2016), $K_v = 0.407$ is the von Karman's constant, $k_s = 2D_{50}$ is the roughness height of the stationary bed, U'_b is the maximum value of the undertow current, that generally occurs in the end of the transition zone, and V'_b is the maximum value of the longshore current. If the criterion (Equation 5.16) is satisfied, a net offshore transport occurs.

The results of this analysis for the two selected tests are shown in Figure 5-9, Figure 5-10 and in Table 5-2.

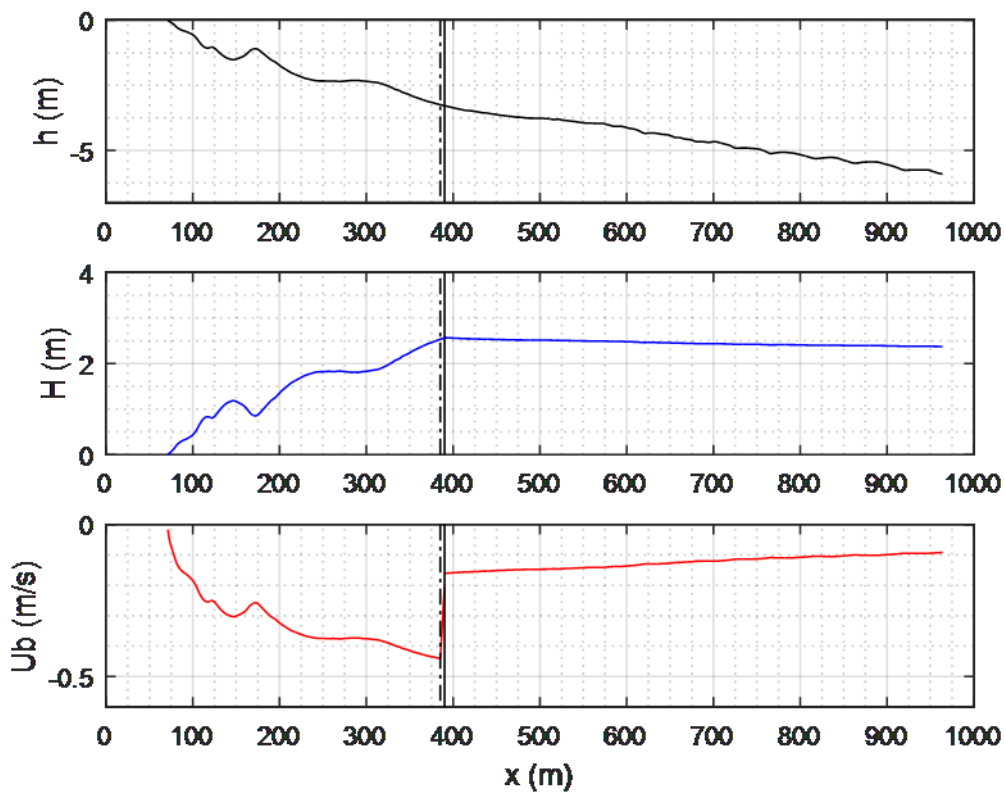


Figure 5-9 – Test1 (ESE) – Upper panel: seabed profile. Middle panel: wave height. Lower panel: mean undertow current. The vertical solid line is the breaking point, the vertical dash-dot line is the end of the transition zone.

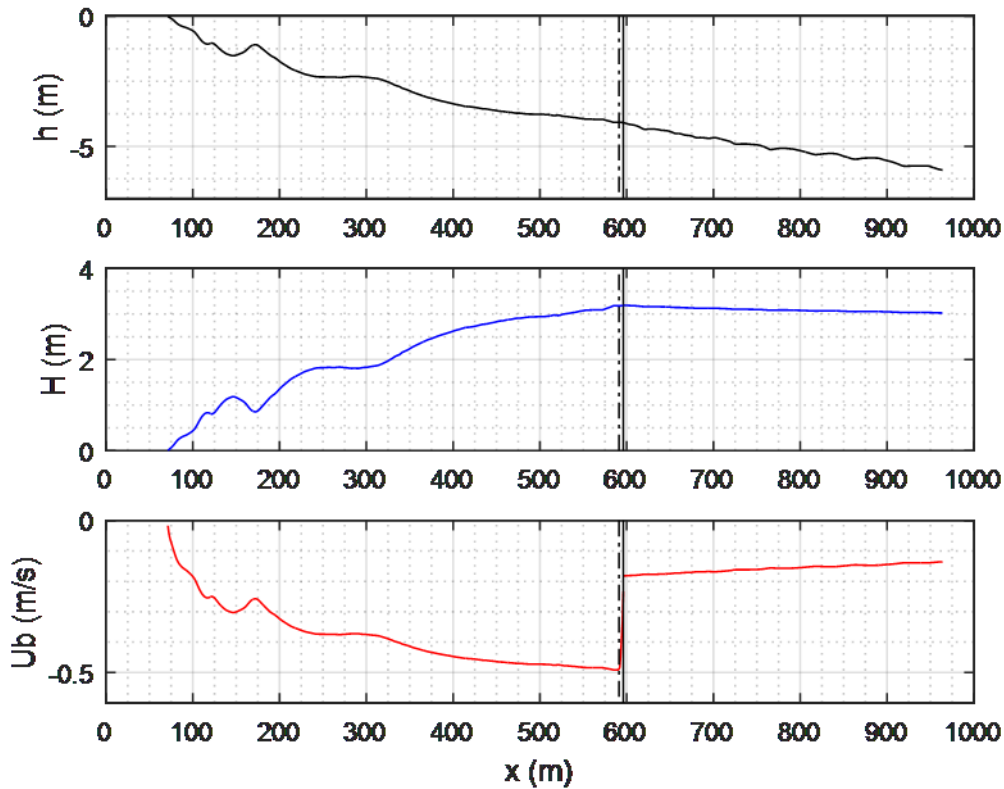


Figure 5-10 – Test2 (NNE) – Upper panel: seabed profile. Middle panel: wave height. Lower panel: mean undertow current. The vertical solid line is the breaking point, the vertical dash-dot line is the end of the transition zone.

Table 5-2 Results of the first net offshore transport analysis. Analytical model of equations (5.9)-(5.18).

| | V_b' [m/s] | U_b' [m/s] | τ_b [Pa] | U_b^* [m/s] | ω/U_b^* | |
|--------------|--------------|--------------|---------------|---------------|----------------|------|
| TEST 1 - ESE | 0.3895 | 0.4408 | 0.7047 | 0.0266 | 0.9663 | >0.8 |
| TEST 2 - NNE | 0.1907 | 0.4915 | 0.5403 | 0.0232 | 1.1057 | >0.8 |

These results show very similar values of the undertow for both tests (Figure 5-9 and Figure 5-10), the only difference being in the break-point location, which is more offshore for Test 1 (ESE storm) than for Test 2 (NNE storm). As expected, the ESE storm being characterized by significantly larger longshore velocities than those of the NNE storm (Table 5-2). Nevertheless, the criterion states that no net sediment transport occurs under both wave condition. On the one hand, it correctly describes the general stability of the bar system,

while on the other it does not detect the net bar migration observed under wave coming from ESE.

In view of the not truly conclusive results, two Boussinesq model numerical simulations have been run, considering the two representative storms, to try to highlight characteristics that could possibly explain the different observed behaviours. The seabed profile used in this analysis was the bathymetry of the survey performed in 2013, while the wave characteristics of the P1 of the COWAST model (Table 5-1) was used for the spectral wave input, since the available offshore boundary corresponds to the 5m bathymetry. The coordinates of the analysis grid were related to a local coordinate system of the model with x -axis pointing onshore and y -axis pointing in south-east direction (Figure 5-11). The resolution of the grid was 2.5m.

The simulation results highlighted no major differences in wave shape, velocity and acceleration skewness (Figure 5-12) or velocity distribution. Only a stronger longshore current forced by the ESE storm has been observed.

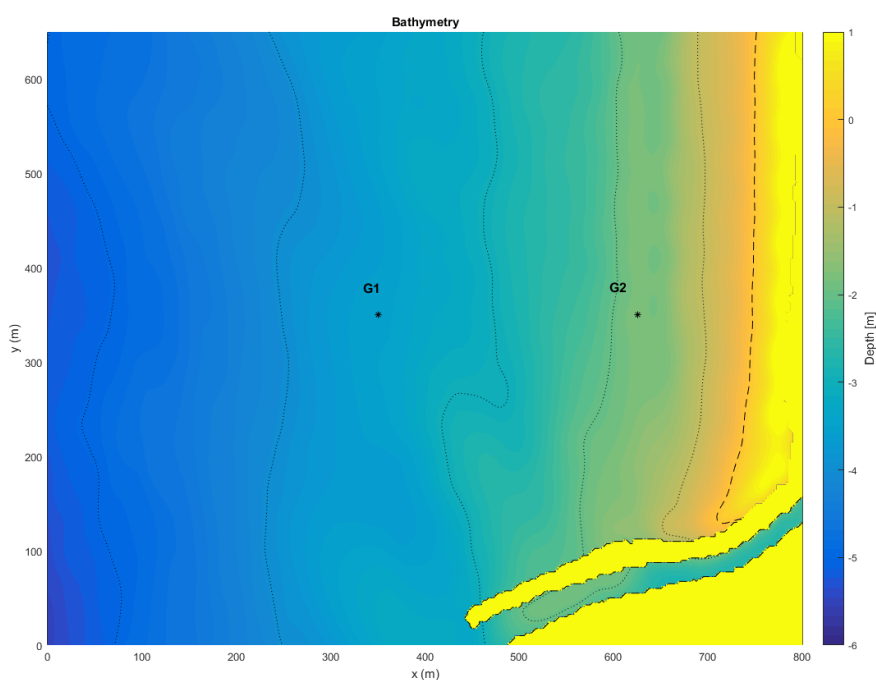


Figure 5-11 –Bathymetry and geometry used in the Boussinesq simulation. Points G1 and G2 are two probes.

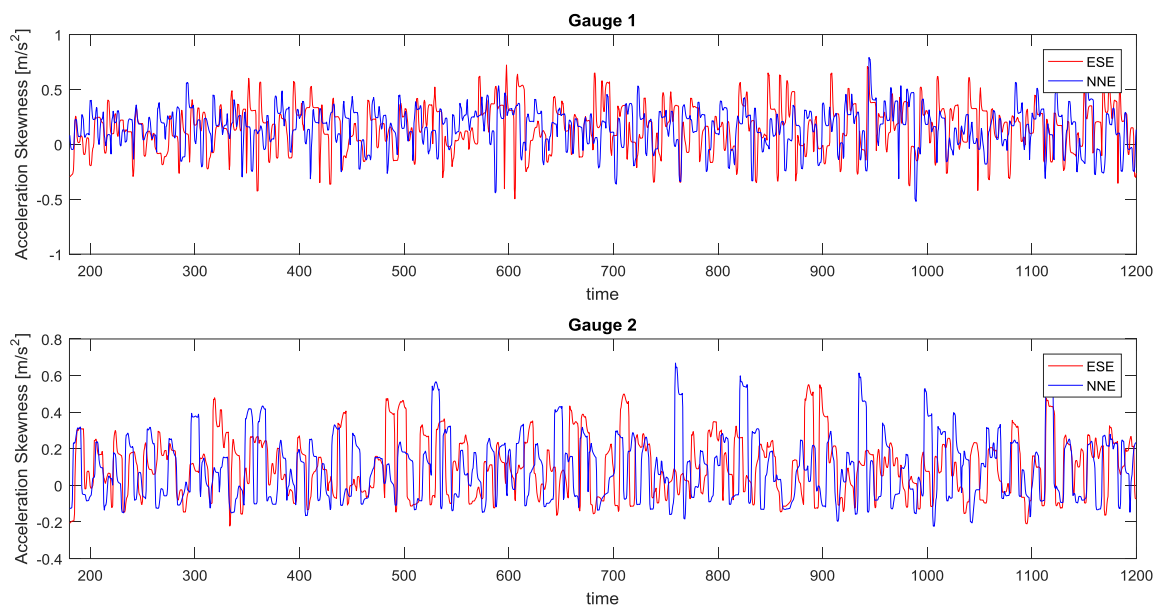


Figure 5-12 – Acceleration skewness recorded from gauge 1 (upper panel) and from gauge 2 (lower panel). The red lines represent the ESE storm while the blue lines represent the NNE storm.

An important aspect to note is that the Boussinesq simulations have been performed by taking into account, unlike the analytical analysis, the nearby river pier. Considering the presence of the jetty is important because the ESE incident waves travel perpendicular to the pier and are strongly reflected there. Therefore, new simulations, have been performed by removing the river pier to investigate possibly different behaviors. The comparison reveals that the wave reflection of the river pier induces an important increase of the longshore velocity, which has been estimated proportional to a factor of 1.8 for both tests.

Then, the analytical analysis of the net offshore transport criterion has been performed by considering the above-mentioned reflection effects, i.e. by increasing the analytically-computed longshore velocity of a 1.8 factor:

$$V'_b = 1.8 V_b \quad (5.19)$$

The results are shown in Table 5-3. For Test 1 (ESE storm) the criterion is now satisfied, indicating a net offshore sediment transport, while for Test 2 (NNE storm) the increase in

longshore velocity is not enough to satisfy the criterion and no offshore sediment transport is predicted. The new results are coherent with the behavior observed from the images. This means that, by considering the reflection off the river pier, the criterion correctly represents the migration behavior of the sandbar system for both forcing conditions (NNE and ESE storms).

Table 5-3 Results of the net offshore transport analysis. Analytical model of equations (5.9)-(5.18) with increased longshore velocities by reflection off the river pier (equation 5.19).

| | V_b' [m/s] | U_b' [m/s] | τ_b [Pa] | U_b^* [m/s] | ω/U_b^* | |
|--------------|--------------|--------------|---------------|---------------|----------------|------|
| TEST 1 - ESE | 0.7012 | 0.4408 | 1.4022 | 0.0374 | 0.6863 | <0.8 |
| TEST 2 - NNE | 0.3433 | 0.4915 | 0.6987 | 0.0264 | 0.9723 | >0.8 |

Summarizing, the aptitude of the waves coming from ESE to generate an important offshore bar migration has been related to the higher longshore velocity increased by the reflection of the waves off the river pier. This because, although the offshore sediment transport is mainly due to the undertow current, the mobilization of the sediment is due to both the undertow current and the longshore current. This behavior has been well represented with the described criterion. The criterion can be easily computed and used as a simple indicator.

Chapter 6 Conclusions

This thesis explored the capability and the first applications of a new video monitoring station, called the “Sena Gallica Speculator” (SGS). The SGS data have been used for the study of the indirect estimation of the bathymetry and of the behaviour of a multiple sandbar system.

The new video monitoring station, was installed in July 2015 at the Senigallia harbour, central Adriatic, as part of the Estuarine Cohesive Sediments (EsCoSed) project (Brocchini et al., 2015). SGS is not part of the Argus network but it was designed on the bases of typical Argus systems. SGS is equipped with four cameras located on the top of a 25m high tower. Unlike Argus stations that store only elaborated images, ten minutes of full-frame video data are collected at 2Hz every hour, during daylight hours, and then post-processed. The beach within the SGS field-of-view is the northern part of a 12 km long stretch of unprotected sandy coast, which is representative of Adriatic beaches placed near river mouths. Even the mouth of the Misa River is within the SGS field of view, therefore the data recorded by the cameras represent a major source of information to improve knowledge on estuarine dynamics. Some morphological and climate characteristics of the observed area have been derived from four bathymetric surveys executed between 2010 and 2103 and historic observations of the wave conditions collected from the Ancona Buoy (RON) between 1999-2006 and 2009-2013. The bathymetric surveys show a general invariance of the seabed profile and the presence of a multiple bar system in a water depth of around 0-3m (Soldini et al., 2014; Postacchini et al., 2017). The maximum tidal range of this area is around 0.6 m, therefore the environment is wave-dominated. The data coming from the Ancona buoy show that the wave climate in Senigallia is characterized by waves coming from two main directions: ESE and NNE. The SGS station is a new tool for investigating nearshore and estuarine hydro-morpho-dynamics in the study area. This technique can give much more

data than in-situ methods with higher temporal and spatial resolution over a long period of observation.

The video data collected by the SGS station has been first post processed using some Matlab© routines coming from the Argus Database and the CIL toolbox. The main products of this elaboration are: the full time series (Timestack) from the recorded period for a selected grid of pixels and the time exposure images (Timex) created by averaging the intensity of each pixel over the 10-minute sampling period. The Timestacks have been used to indirectly estimate the bathymetry, while Timex images have been first orthorectified and stabilized and, then, used to estimate the sandbar locations. Videos of the period 2015-2017 have been elaborated.

The indirect estimation of the bathymetry was carried out by applying the widely used cBathy algorithm to the Timestacks derived from the post processing of the SGS data. The results varied in quality as a function of the location and wave conditions and, in particular, a significative underestimation of the depth in a large portion of the domain has been found. Therefore, a detailed debugging analysis has been performed. At first a classical cBathy debug, implemented in the code, has been run and the Timestack, the full phase maps and the phase maps of individual analysis point have been investigated. Since no significant errors have been highlighted, further analyses have been carried out to check if the code estimated properly the dominant frequencies and wavelengths. To this scope a manual computation of the wavelength and wave celerity has been done. To exclude problems related to the camera boundary also an analysis with separated cameras has been performed. Moreover, errors related to low resolution, optical distortion and geometry have been analyzed and excluded. All the several analyses performed during the debugging highlighted that the code estimates well the wave period, while it underestimates the wavelength, and thus the depth, even if the nonlinear fitting that the code executed to define the wavelength runs correctly. Moreover, the wavelength estimates have been found coherent with the signatures visible on the optical images. Additionally, an influence of the wave direction on the results has been noted. This is important for the SGS station, which persistently looks the waves quite along the crests. Since it is known from the literature that in this condition the waves are not correctly visible on the optical images, the effect of this issue on the results of cBathy has been analysed. Therefore, synthetic tests were run to analyze the effects of the

wave direction on the water depth estimation, using the optical implementation of cBathy v1.1. The error in the water depth estimates where wave viewing angle was less than 75° were consistent with previous field observations (order 0.2 m – 0.5 m). Given that the synthetic tests were designed to adhere to the algorithm's assumptions, the result suggests the limit of accuracy that can be expected from the algorithm. When the wave viewing angle exceeded 75° , the wave crests became obscured, leading to errors in both frequency and wavenumber and giving errors in the depth reconstruction. Errors were larger for directionally-spread waves. The importance of correctly setting the initial direction that is used by cBathy v1.1 to start the nonlinear fit was also investigated by means of synthetic tests. Such results can be applied to design future fixed camera coastal video monitoring stations or to develop sampling schemes for small Unmanned Aerial Systems (sUAS) with viewing direction different from the typically offshore-pointing azimuth direction.

A second study focused on the capability of the SGS station to study a multiple sandbar system present at the Senigallia beach. For this analysis stabilized time exposure images have been used, since these images display the areas of preferred wave breaking as white bands. The semi-automated Barline Intensity Mapper (BLIM) algorithm has, then, used to identify the position of the sandbars at Senigallia. The analysis covered the years 2015-2017. Three orders of bars have been well identified from the images, in agreement with previous investigations carried out by in-situ bathymetric surveys. Therefore, the SGS station is able to monitor such seabed features and the results can be used to study the physical behavior of the bar system. An overall analysis of the identified bars has shown that the Senigallia sandbar system is made of three bars that are typically alongshore uniform, but occasionally display some complexity such as bar welding, forked shapes and bars separation. Such complexity should be better investigated since it could be related to important physical phenomena such as rip currents (gap opening in longshore bars). The bar motion has then been correlated with the wave climate, modelled by means of the COAWST model. Given the alongshore linearity of the bars, only the mean position has been considered for this analysis. A general offshore migration was observed during periods characterized by intense wave action, while an onshore migration was observed during periods of persistent mild waves, in agreement with the literature. Moreover, the outer bar position was found to be more influenced by single storm events. The most important aspect observed from this

analysis is a different behavior of the bar migration in relation to the angle of the incoming waves. In fact, a net offshore migration was observed only during a strong ESE storm, while for the storms with waves coming from NNE no significant bar migration has been observed. An analysis of the energy flux and duration of the single storms has shown that the offshore migration of the bars, especially the outer bar, is related to the high levels of storm energy flux and to the duration of the storm, as expected from the literature, but it did not explain the net offshore bar migration under waves coming from ESE since they are as energetic as the others. An analytical criterion to define a net offshore transport, that takes into account both the undertow current and the longshore current, has been used to investigate offshore bar migration for two representative tests. From a first analysis the criterion stated that no net transport would occur for both the analyses tests. Boussinesq simulations have been performed to pinpoint the main differences between waves coming from different directions. These simulations did not show specific differences in wave shape or velocity distribution but highlighted the importance of accounting for wave reflection off the nearby river pier, which largely intensifies the magnitude of the longshore current responsible for seabed sediment stirring. By considering such increment the analytical criterion in use well represented both the negligible migration due to NNE events and the net offshore migration forced by waves coming from ESE, as observed by the images. This analysis allowed also to highlight the relevance of rigid structures on the sandbar dynamic.

The two first applications of the SGS data discussed in this thesis explored only a small part of the capability of the station. Given the peculiarity of the data stored (videos) and the strategic location of the station, the SGS will allow for intriguing future studies. Some riverine and estuarine processes are still under investigation. For example, a river emerged sandbar was periodically observed near the mouth of the Misa River while, after storm events, floating object and plume are clearly visible from the recorded video. Analysis of all these dynamics is partly ongoing and planned for the near future.

References

- Aagaard, T., Nielsen, J., Jensen, S. G., & Friderichsen, J. (2004). Longshore sediment transport and coastal erosion at Skallingen, Denmark. *Geografisk Tidsskrift-Danish Journal of Geography*, **104**(1), 5–14.
- Aarninkhof, S. G. ., Turner, I. L., Dronkers, T. D., Caljouw, M., & Nipius, L. (2003). A video-based technique for mapping intertidal beach bathymetry. *Coastal Engineering*, **49**(4), 275–289.
- Aarninkhof, S. G. J., Ruessink, B. G., & Roelvink, J. A. (2005). Nearshore subtidal bathymetry from time-exposure video images. *J. Geophys. Res*, **110**, 6011.
- Abreu, T., Sancho, F., & Silva, P. (2012). Influence of Non-Linear Waves and Undertow in Sandbar Development. *Coastal Engineering Proceedings*, 1–14.
- Alexander, P. S., & Holman, R. A. (2004). Quantification of nearshore morphology based on video imaging. *Marine Geology*, **208**(1), 101–111.
- Almar, R., Bonneton, P., Senechal, N., & Roelvink, D. (2009). Wave celerity from video imaging: a new method. In *Coastal Engineering 2008*, World Scientific Publishing Company, pp. 661–673.
- Archetti, R. (2009). Quantifying the Evolution of a Beach Protected by Low Crested Structures Using Video Monitoring. *Journal of Coastal Research*, **254**, 884–899.
- Armaroli, C., & Ciavola, P. (2011). Dynamics of a nearshore bar system in the northern Adriatic: A video-based morphological classification. *Geomorphology*, **126**(1–2), 201–216.
- Beck, M. W., Losada, I. J., Menéndez, P., Reguero, B. G., Díaz-Simal, P., & Fernández, F. (2018). The global flood protection savings provided by coral reefs. *Nature Communications*, **9**(1), 2186.
- Bell, P. S. (1999). Shallow water bathymetry derived from an analysis of X-band marine radar images of waves. *Coastal Engineering*, **37**(3–4), 513–527.

- Bergsma, E. W. J., & Almar, R. (2018). Video-based depth inversion techniques, a method comparison with synthetic cases. *Coastal Engineering*, **138**(August 2017), 199–209.
- Bergsma, E. W. J., Conley, D. C., Davidson, M. A., & O'hare, T. J. (2016). Video-based nearshore bathymetry estimation in macro-tidal environments. doi:10.1016/j.margeo.2016.02.001
- Brocchini, M., Calantoni, J., Reed, A. H., & Soldini, L. (2015). Summertime conditions of a muddy estuarine environment: The EsCoSed project contribution. *Water Science and Technology*, **71**(10), 1451–1457.
- Brocchini, M., Postacchini, M., Lorenzoni, C., & Smith, J. (2017). Comparison between the wintertime and summertime dynamics of the Misa River estuary. *Marine Geology*, **385**, 27–40.
- Brodie, K. L., Palmsten, M. L., Hesser, T. J., & Elgar, S. (2018). Evaluation of video-based linear depth inversion performance and applications using altimeters and hydrographic surveys in a wide range of environmental conditions. *Coastal Engineering*, **136**(December 2017), 147–160.
- Carter, D. J. T. (1982). Prediction of wave height and period for a constant wind velocity using the JONSWAP results. *Ocean Engineering*, **9**(1), 17–33.
- Catalán, P. A., & Haller, M. C. (2008). Remote sensing of breaking wave phase speeds with application to non-linear depth inversions. *Coastal Engineering*, **55**(1), 93–111.
- Certain, R., & Barusseau, J.-P. (2005). *Conceptual modelling of sand bars morphodynamics for a microtidal beach (Sète, France)*. *Bull. Soc. géol. Fr*, Vol. 176.
- Chapman, R. D. (1981). Visibility of rms slope variations on the sea surface. *Applied Optics*, **20**(11), 1959–66.
- Chapman, R. D., & Irani, G. B. (1981). Errors in estimating slope spectra from wave images. *Applied Optics*, **20**(20), 3645.
- Chickadel, C. (2007). Remote Measurements of Waves and Currents over Complex Bathymetry. *Oceanography*, **PhD**, 117.
- Coastal Engineering Manual (Engineer Manual 1110-2-1100) Chapter II-4: Surf Zone Hydrodynamics. Washington, DC: U.S. Army Corps of Engineers; 2003
- Davidson, M., Van Koningsveld, M., de Kruif, A., & Aarninkhof, S. (2007). The CoastView project: Developing video-derived Coastal State Indicators in support of coastal zone management. *Coastal Engineering*, **54**(6–7), 463–475.

- Dean, R. G. (1991). Equilibrium Beach Profiles: Characteristics and Applications. *Journal of Coastal Research*, Coastal Education & Research Foundation, Inc., pp. 53–84.
- Dugan, J. P., Piotrowski, C. C., & Williams, J. Z. (2001). Water depth and surface current retrievals from airborne optical measurements of surface gravity wave dispersion. *Journal of Geophysical Research: Oceans*, **106**(C8), 16903–16915.
- Gallagher, E. L., Elgar, S., & Guza, R. T. (1998). Observations of sand bar evolution on a natural beach. *Journal of Geophysical Research*, **103**, 3203–3215.
- Gao, J. (2009). Bathymetric mapping by means of remote sensing: methods, accuracy and limitations. *Progress in Physical Geography*, **33**(1), 103–116.
- Grilli, S. T. (1998). Depth inversion in shallow water based on nonlinear properties of shoaling periodic waves. *Coastal Engineering*, **35**(3), 185–209.
- Hamm, L., Capobianco, M., Dette, H. ., Lechuga, A., Spanhoff, R., & Stive, M. J. . (2002). A summary of European experience with shore nourishment. *Coastal Engineering*, **47**(2), 237–264.
- Hanson, H., & Kraus, N. C. (1989). *Genesis: Generalized model for simulating shoreline change, report 1, technical reference*, doi:10.5962/bhl.title.48202
- Harris, C. K., Sherwood, C. R., Signell, R. P., & Warner, J. C. (2008). Sediment dispersal in the northwestern Adriatic Sea. *J. Geophys. Res*, **113**, 11–14.
- Hartley, R., & Zisserman, A. (2003). *Multiple view geometry in computer vision*, Cambridge University Press.
- Hoefel, F., & Elgar, S. (2003). Wave-induced sediment transport and sandbar migration. *Science (New York, N.Y.)*, **299**(5614), 1885–7.
- Holland, K. T., & Holman, R. A. (1997). Video Estimation of Foreshore Topography Using Trinocular Stereo. *Journal of Coastal Research*, Coastal Education & Research Foundation, Inc., pp. 81–87.
- Holland, K. T., Holman, R. A., Lippmann, T. C., Stanley, J., & Plant, N. (1997). Practical use of video imagery in nearshore oceanographic field studies. *IEEE Journal of Oceanic Engineering*, **22**(1), 81–92.
- Holman, R. ., Lippmann, T. ., O’Neill, P. ., & Hathaway, K. (1991). Video estimation of subaerial beach profiles. *Marine Geology*, **97**(1–2), 225–231.
- Holman, R. A., Brodie, K. L., & Spore, N. J. (2017). Surf Zone Characterization Using a Small

- Quadcopter: Technical Issues and Procedures. *IEEE Transactions on Geoscience and Remote Sensing*, **55**(4), 2017–2027.
- Holman, R. A., Lalejini, D. M., Edwards, K., & Veeramony, J. (2014). A parametric model for barred equilibrium beach profiles. doi:10.1016/j.coastaleng.2014.03.005
- Holman, R. A., Lalejini, D. M., & Holland, T. (2016). A parametric model for barred equilibrium beach profiles: Two-dimensional implementation. *Coastal Engineering*, **117**, 166–175.
- Holman, R. A., & Sallenger, A. H. (1993). Sand bar generation: A discussion of the Duck experiment series. *Journal of Coastal Research*, (15), 76–92.
- Holman, R. A., Sallenger, A. H., Lippmann, T. C., & Haines, J. W. (1993). *The application of video image processing to study of nearshore processes*.
- Holman, R. A., & Stanley, J. (2007). The history and technical capabilities of Argus. *Coastal Engineering*, **54**(6–7), 477–491.
- Holman, R., Plant, N., & Holland, T. (2013). CBathy: A robust algorithm for estimating nearshore bathymetry. *Journal of Geophysical Research: Oceans*, **118**(5), 2595–2609.
- Holman, R., & Stanley, J. (2013). cBathy Bathymetry Estimation in the Mixed Wave-Current Domain of a Tidal Estuary. *Journal of Coastal Research*, **165**(65), 1391–1396.
- Hsu, T.-J., Elgar, S., & Guza, R. T. (2006). Wave-induced sediment transport and onshore sandbar migration. *Coastal Engineering*, **53**(10), 817–824.
- Irish, J. L., & Lillycrop, W. J. (1999). *Scanning laser mapping of the coastal zone: the SHOALS system*. *ISPRS Journal of Photogrammetry & Remote Sensing*, Vol. 54.
- Lee, G., Nicholls, R. J., & Birkemeier, W. A. (1998). Storm-driven variability of the beach-nearshore profile at Duck, North Carolina, USA, 1981–1991. *Marine Geology*, **148**(3–4), 163–177.
- Lippmann, T. C., & Holman, R. A. (1990). The spatial and temporal variability of sand bar morphology. *Journal of Geophysical Research*, **95**(C7), 11575.
- Longuet-Higgins, M. S. (1970). Longshore currents generated by obliquely incident sea waves: 1. *Journal of Geophysical Research*, **75**(33), 6778–6789.
- Masselink, G., & Short, A. D. (1993). The Effect of Tide Range on Beach Morphodynamics and Morphology: A Conceptual Beach Model. *Journal of Coastal Research*, Coastal Education & Research Foundation, Inc., pp. 785–800.
- Méndez, G. M. D., Haller, M. C., Raubenheimer, B., Elgar, S., & Honegger, D. A. (2015). Radar

- remote sensing estimates of waves and wave forcing at a Tidal inlet. *Journal of Atmospheric and Oceanic Technology*, **32**(4), 842–854.
- Misra, S. K., Kennedy, A. B., & Kirby, J. T. (2003). An approach to determining nearshore bathymetry using remotely sensed ocean surface dynamics. *Coastal Engineering*, **47**(3), 265–293.
- Nwogu, O., Mansard, E. P. D., Miles, M., & Isaacson, M. (1987). Estimation of directional wave spectra by the Maximum Entropy Method. In *Proc. IAHR Seminar on Wave Analysis and Generation in Laboratory Basins, XXII IAHR Congress, Lausanne, Switzerland*, pp. 363–376.
- Ojeda, E., & Guillén, J. (2006). Monitoring beach nourishment based on detailed observations with video measurements. *Journal of Coastal Research*, Coastal Education & Research Foundation, Inc., pp. 100–106.
- Parlagreco, L., Archetti, R., Simeoni, U., Devoti, S., Valentini, A., & Silenzi, S. (2011). Video-monitoring of a barred nourished beach (Latium, Central Italy). *Journal of Coastal Research*, (SPEC. ISSUE 64), 110–114.
- Percival, D. B. (1992). Simulating Gaussian Random Processes with Specified Spectra. *COMPUTING SCIENCE AND STATISTICS*, **24**, 534–538.
- Piotrowski, C. C., & Dugan, J. P. (2002). Accuracy of bathymetry and current retrievals from airborne optical time-series imaging of shoaling waves. *IEEE Transactions on Geoscience and Remote Sensing*, **40**(12), 2606–2618.
- Plant, N. G., Freilich, M. H., & Holman, R. A. (2001). Role of morphologic feedback in surf zone sandbar response. *Journal of Geophysical Research: Oceans*, **106**(C1), 973–989.
- Plant, N. G., Holland, K. T., & Haller, M. C. (2008). Ocean Wavenumber Estimation From Wave-Resolving Time Series Imagery. *IEEE Transactions on Geoscience and Remote Sensing*, **46**(9), 2644–2658.
- Plant, N. G., & Holman, R. A. (1997). Intertidal beach profile estimation using video images. *Marine Geology*, **140**(1–2), 1–24.
- Postacchini, M., Soldini, L., Lorenzoni, C., & Mancinelli, A. (2017). Medium-Term dynamics of a middle Adriatic barred beach. *Ocean Science*, **13**(5), 719–734.
- Price, T. D., & Ruessink, B. G. (2011). State dynamics of a double sandbar system. *Continental Shelf Research*, **31**(6), 659–674.
- Radermacher, M., Wengrove, M., van Thiel de Vries, J., & Holman, R. (2014). Applicability of

- video-derived bathymetry estimates to nearshore current model predictions. *Journal of Coastal Research*, **70**, 290–295.
- Rattanapitikon, W., & Shibayama, T. (2000). Simple Model For Undertow Profile, *Coastal Engineering Journal*, **42**(1), 1–30.
- Ribas, F., Ojeda, E., Price, T. D., Guillén, J., Ojeda, E., & Guillén, J. (2010). Assessing the Suitability of Video Imaging for Studying the Dynamics of Nearshore Sandbars in Tideless Beaches. *IEEE TRANSACTIONS ON GEOSCIENCE AND REMOTE SENSING*, **48**(6). doi:10.1109/TGRS.2009.2039576
- Roelvink, J. A., & Stive, M. J. F. (1989). Bar-generating cross-shore flow mechanisms on a beach. *J Geophys Res C Oceans* **94**(4), 4785-4800. (1989).
- Rutten, J., de Jong, S. M., & Ruessink, G. (2017). Accuracy of Nearshore Bathymetry Inverted From $\{X\}$ -Band Radar and Optical Video Data. *IEEE Transactions on Geoscience and Remote Sensing*, **55**(2), 1106–1116.
- Scarsi, G. (2009). *Elementi di idraulica marittima e costiera (In italian)*, ARACNE, Roma.
- Sembiring, L., van Dongeren, A., Winter, G., van Ormondt, M., Briere, C., & Roelvink, D. (2014). Nearshore bathymetry from video and the application to rip current predictions for the Dutch Coast. *Journal of Coastal Research*, **70**, 354–359.
- Sherwood, C., Book, J., Carniel, S., & Warner, J. (2004). Sediment Dynamics in the Adriatic Sea Investigated with Coupled Models. *Oceanography*, **17**(4), 58–69.
- Shore protection Manual Volume I, Washington, DC: U.S. Army Corps of Engineers; 1984
- Short, A. D., & Aagaard, T. (1993). Single and Multi-Bar Beach Change Models. *Journal of Coastal Research*, Coastal Education & Research Foundation, Inc., pp. 141–157.
- Silva, P. A., Abreu, T., A, D. A. Van Der, & Sancho, F. (2011). Sediment transport in nonlinear skewed oscillatory flows : Transkew experiments, **49**(sup1), 72-80. doi:10.1080/00221686.2011.592681
- Soldini, L., Postacchini, M., Lorenzoni, C., & Mancinelli A. (2014). L'evoluzione della costa nel breve e lungo periodo : il caso di Senigallia (AN), Proc of 5th Int. Symp. Monitoring of Mediterranean Coastal Areas: problems and measurements techniques, Livorno, Italy, 759-768, (in Italian).
- Stilwell, D. (1969). Directional energy spectra of the sea from photographs. *Journal of Geophysical Research*, **74**(8), 1974–1986.

- Stockdon, H. F., & Holman, R. A. (2000). Estimation of wave phase speed and nearshore bathymetry from video imagery. *Journal of Geophysical Research: Oceans*, **105**(C9), 22015–22033.
- Svendsen, I. A. (2006). *Introduction to nearshore hydrodynamics*, World Scientific.
- van Enckevort, I. M. ., & Ruessink, B. . (2003). Video observations of nearshore bar behaviour. Part 1: alongshore uniform variability. *Continental Shelf Research*, **23**(5), 501–512.
- Van Enckevort, I. M. J., & Ruessink, B. G. (2001). Effect of hydrodynamics and bathymetry on video estimates of nearshore sandbar position. *Journal Of Geophysical Research*, Vol. 106.
- van Rijn, L. C., Wasltra, D. J. R., Grasmeyer, B., Sutherland, J., Pan, S., & Sierra, J. P. (2003). The predictability of cross-shore bed evolution of sandy beaches at the time scale of storms and seasons using process-based profile models. *Coastal Engineering*, **47**(3), 295–327.
- Walker, R. E. (1994). *Marine light field statistics*, New York: Wiley.
- Walstra, D. J. R., Reniers, A. J. H. M., Ranasinghe, R., Roelvink, J. A., & Ruessink, B. G. (2012). On bar growth and decay during interannual net offshore migration. *Coastal Engineering*, **60**, 190–200.
- Wang, Y. (2016). Predicting net cross-shore total load transport: A phase-averaging, quasi-steady approach incorporating undertow contribution. *China Ocean Engineering*, **30**(5), 703–717.
- Wright, L. ., & Short, A. . (1984). Morphodynamic variability of surf zones and beaches: A synthesis. *Marine Geology*, **56**(1–4), 93–118.
- Yoo, J., Fritz, H. M., Haas, K. A., Work, P. A., & Barnes, C. F. (2011). Depth Inversion in the Surf Zone with Inclusion of Wave Nonlinearity Using Video-Derived Celerity. *Journal of Waterway, Port, Coastal, and Ocean Engineering*, **137**(2), 95–106.
- Zanke, U., Berechnung der Sinkgeschwindigkeiten von Sedimenten, Mitt. des Franzius-Instituts fiir Wasserbau, Heft 46, Seite 243, Technical University, Hannover, West Deutschland, 1977 (in German)
- Zuckerman, S., & Anderson, S. (2018). Bathymetry and Water-Level Estimation Using X-Band Radar at a Tidal Inlet. *Journal of Coastal Research*. doi:10.2112/JCOASTRES-D-17-00182.1